UNIVERSIDAD NACIONAL AUTÓNOMA DE MÉXICO

POSGRADO EN CIENCIAS FÍSICAS

On the relaxation and rigidity properties in glass forming systems

TESIS
PARA OPTAR POR EL GRADO DE:
DOCTOR EN CIENCIAS (FÍSICA)

Presenta:

Javier Quetzalcóatl Toledo Marín

Dr. Gerardo García Naumis
Instituto de Física, UNAM
Dra. Rosario Paredes Gutiérrez
Instituto de Física, UNAM
Dr. Rubén Santamaría Ortiz
Instituto de Física, UNAM

México, CDMX, Diciembre 2019

On the relaxation and rigidity properties in glass forming systems.

J. Quetzalcóatl Toledo-Marín

Agradecimientos

Agradezco a Olivia y a mis padres.

Seguidamente, agradezco al Instituto de Física y a los investigadores que de algún modo u otro contribuyeron con esta tesis. En particular, agradezco a Le Yan, Adrián Huerta, Leonardo Dagdug, J. Rubén Gómez y Hugo Flores.

Agradezco el apoyo de CONACYT y al proyecto DGAPA-UNAM IN102717.

También agradezco a Ariel y Joanka.

Finalmente, agradezco a Naumis por ser mi supervisor, por tenerme paciencia, por siempre ser tan entusiasta y por compartir su conocimiento de la física, en particular, y de lo no tan particular. Se requiere de mucho no sé qué para saber guiar el trabajo de investigación sin imponerlo, y se requiere de otro tanto más de no sé qué para lograrlo publicar.

List of publications

- J.Q. Toledo-Marín, C. Rodríguez, Y Plasencia Montesino, G.G. Naumis. *Phase Diagram for a model of Spin Crossover in Molecular Crystals. arXiv:1907:03896.* **under review** (2019).

- A. Huerta, J.Q. Toledo-Marín, G.G. Naumis. *How the overlap of excluded volume determines the configurational energy landscape and" thermodynamics" in the" one to five hard disks in a box" system. arXiv preprint arXiv:1903.09100.* **accepted in *Physica A*** (2019).

- J.Q. Toledo-Marin and Le Yan. "Competition between entropy and energy in network glass: the hidden connection between intermediate phase and liquid-liquid transition." Frontiers in Materials 6 : 196 (2019).

- J.Q. Toledo-Marín and Gerardo G. Naumis. "Testing rigidity transitions in glass and crystal forming dense liquids: viscoelasticity and dynamical gaps." Frontiers in Materials 6 : 164 (2019).

- J.Q. Toledo-Marín and Gerardo G. Naumis. "Viscoelasticity and dynamical gaps: rigidity in crystallization and glass-forming liquids." Journal of Non-Crystalline Solids: X : 100030 (2019).

- M.A. Moret, G. Zebende, J.C. Phillips, J.Q. Toledo-Marín, G.G Naumis. *Más Allá de La Filogenética: Evolución Darwiniana de La Actina.* Revista Mexicana de Ingeniería Biomédica, 40(1), 1-11 (2018).

- J.Q. Toledo-Marín, G.G. Naumis. *Escape time, relaxation, and sticky states of a softened Henon-Heiles model: Low-frequency vibrational mode effects and glass relaxation.* Physical Review E, 97(4), 042106 (2018).

- J.Q. Toledo-Marín, G.G. Naumis. *Short time dynamics determine glass forming ability in a glass transition two-level model: A stochastic approach using Kramers escape formula.* The Journal of Chemical Physics, 146(9), 094506 (2017).

- J.Q. Toledo-Marín, R. Diaz-Mendez, M.D.C. Mussot. *Is a good offensive always the best defense?*. International Game Theory Review, 19(01), 1750004 (2017)

- J.Q. Toledo-Marín, I.P. Castillo, G.G. Naumis. *Minimal cooling speed for glass transition in a simple solvable energy landscape model.* Physica A: Statistical Mechanics and its Applications, 451, 227-236 (2016).

Disclosure

The present text is based on four publications, namely,

- J.Q. Toledo-Marín and Gerardo G. Naumis. "Testing rigidity transitions in glass and crystal forming dense liquids: viscoelasticity and dynamical gaps." Frontiers in Materials 6 : 164 (2019).

- J.Q. Toledo-Marin and Le Yan. "Competition between entropy and energy in network glass: the hidden connection between intermediate phase and liquid-liquid transition." Frontiers in Materials 6 : 196 (2019).

- J.Q. Toledo-Marín and Gerardo G. Naumis. *Escape time, relaxation, and sticky states of a softened Henon-Heiles model: Low-frequency vibrational mode effects and glass relaxation.* Physical Review E, 97(4), 042106 (2018).

- J.Q. Toledo-Marín and Gerardo G. Naumis. *Short time dynamics determine glass forming ability in a glass transition two-level model: A stochastic approach using Kramers escape formula.* The Journal of Chemical Physics, 146(9), 094506 (2017).

as well as complementary material.

Contents

Abstract

Rigidity theory has shown experimentally a link between rigidity and relaxation. Specifically, how by varying the coordination number of a glass forming material the necessary cooling speed for a strong glass forming tendency varies as well. Yet, a proper understanding on how these two features are related is still lacking. The main objective in this work is to provide a better understanding of relaxation and rigidity in glass forming systems as well as establishing the missing links between these two. To this end, we first develop a simple solvable glass model from the energy landscape point of view. This model has a first order phase transition to a crystal as well as a dynamic transition to a glass. In this model we are able to find analytical expressions for the relaxation times as a function of the short time dynamics as well as the minimum cooling speed for a strong glass forming tendency. We show how the vibrational modes, together with the energy barriers, determine the relaxation. Our strategy consists on using Kramers' transition state theory. Then, we present a non-linear, non-deterministic, zero temperature model where we study the floppy modes relation with energy barriers and the latter with the relaxation time. We find a broad range of relaxation times scales that arise from dynamical heterogeneity. We further pinpoint the plethora of initial configurations to understand how these power-law relaxation time appear. This, we discuss, is useful in glass dynamics such as molecular rearrangements usually related with the β-relaxation. Then we present the conclusions of the chapter while setting the tone for the next chapter.Then we turn to the rigidity aspects, namely, we first study the relationship between rigidity and floppy modes by means of simulation of hard-disks. We present the concept of dynamical-gap and show its usefulness in characterizing the rigidity, counting floppy modes and using it as a order parameter. Then, we present a model which shows how floppy modes emerge through maximization of vibrational entropy. We then relate this with the heterogeneous-homogeneous phase transition.

Productive stupidity means being ignorant by choice. Focusing on important questions puts us in the awkward position of being ignorant. One of the beautiful things about science is that it allows us to bumble along, getting it wrong time after time, and feel perfectly fine as long as we learn something each time. No doubt, this can be difficult for students who are accustomed to getting the answers right. No doubt, reasonable levels of confidence and emotional resilience help, but I think scientific education might do more to ease what is a very big transition: from learning what other people once discovered to making your own discoveries. The more comfortable we become with being stupid, the deeper we will wade into the unknown and the more likely we are to make big discoveries.

Martin A. Schwartz

The importance of stupidity in scientific research

Journal of Cell Science 2008 121: 1771 doi: 10.1242/jcs.033340

Chapter 1

Introduction

1.1 Conventional Wisdom

Glasses have an overwhelming presence in our societies, they are part of our daily lives. Examples of the above are window glasses, jars and containers of products for our consumption, smart phone screens, optic fiber and data storage devices. Corning Industries claim that when historians write about this age, it should be called *Glass Age*. Although the scientific literature concerning this subject is extensive, it is still an open and complex problem, and our understanding of the subject is, to a large extent, phenomenological (1–13). The reason for this is due to the fact that the formation of glass occurs outside the thermodynamic equilibrium and there is no long-range order. That is why studying glasses with techniques of the solid state or conventional statistical physics does not respond to the unknowns of the glass forming process (14).

From a fundamental and technological point of view, the most important variable for glass formation is the cooling rate (10; 15). However, in recent times a variety of phenomena have been found to show glassy behavior. In this sense, it is said that a material is *glassy* when its relaxation time becomes of the order of or greater than the duration of the experiment or the numerical simulation. Under this generic definition, a large number of systems are grouped altogether, that is, supercooled liquid, type II superconductors with disorder, spin glasses, colloidal systems, emulsions, granular media, proteins and complex fluids (16).

In general, if one takes a material in its liquid phase and it is cooled in a quasi-static manner, the given material will have a temperature such that when it is crossed, the material crystallizes. That temperature is defined as the crystallizing temperature of the material, T_c. If we repeat the process

but now the cooling is carried out (sufficiently) fast, the material will not crystallize. What happens is that the liquid enters a supercooled metastable state where a number of thermodynamical properties seemingly behave as in the liquid while a number of dynamical properties do not. For instance, the viscosity varies by more than ten orders of magnitude as the temperature varies by a factor of three and at some point the system becomes so viscous that for the purpose of the experiment, the system becomes a solid. This state of matter is called glass or glass state. Thus glass is a solid as is the crystalline phase, but unlike the latter, the glass is isotropic and has no long-range order, as in the liquid phase. There are those who state that glass is a system outside of equilibrium, which physical properties evolve into a state in equilibrium (17). Therefore, in principle, glass properties change over time, and the glass state is not unique. The latter is supported by the fact that the glass, in principle, does not comply with the third law of thermodynamics. This relaxation of the glass is easily observed as the cooling increases or when the glass is at a temperature close to the glass transition temperature (13).

There are several techniques to characterize a glass, among them there's neutron, light and X-rays diffraction which measures the dielectric constant, specific heat, compressibility and viscosity, that is, the susceptibilities or responses to a change in an external parameter. The point at which the glass state is obtained is called the glass transition and the temperature at which it occurs is called the glass transition temperature. Additionally, it is possible to obtain a glass at high pressure, so one would define a glass transition pressure. One property of the transition is the continuity of the entropy and the volume although its derivatives are discontinuous, in this sense the transition is similar to a second order phase transition in the Ehrenfest formalism.

On the other hand, Phillips (see (18)) observed that for several chalcogenides supercooled liquids, the minimum cooling rate for a strong tendency to form the glass is a function of the system rigidity. This gave rise to his well-known rigidity theory which we can summarize as follows. When the number of constraints between atoms is equal to the number of degrees of freedom, the tendency of glass formation is optimized, that is, to obtain glass it is enough to cool it with a minimal speed. In this situation, the average number of coordination is equal to the critical coordination number of percolation, so that domains of floppy modes (modes of zero frequency) coexist with rigid modes. As the average number of coordination decreases, which is achieved by varying the chemical composition of the system, floppy modes increase. Increasing floppy modes by number makes glass formation difficult. The same happens in the case where there are only non-floppy modes.

Relaxation times are proportional to the viscosity coefficient. To see this, recall that the viscosity

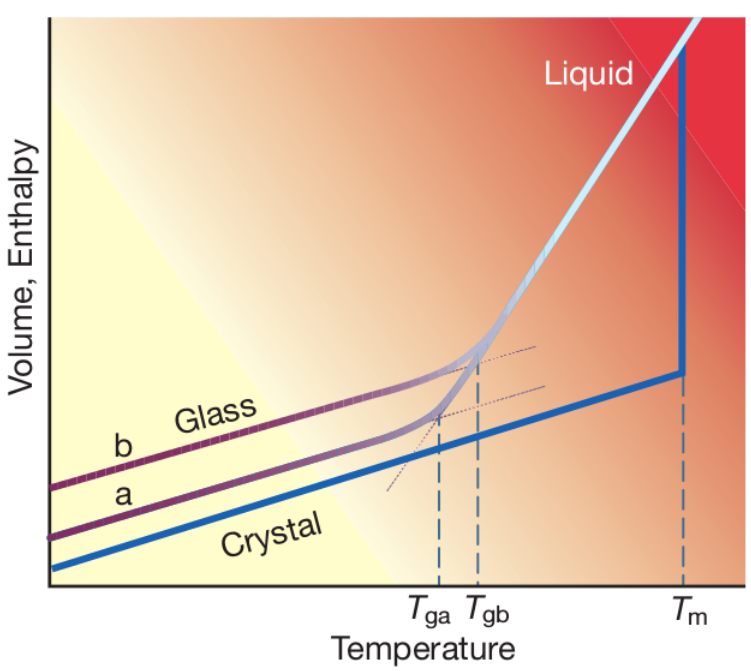

Figure 1.1: Specific volume (or enthalpy, as well) dependence with temperature at constant pressure. The temperature T_m denotes the melting temperature, while T_{ga} and T_{gb} denote the glass transition temperature for different cooling speeds, where the former corresponds to a smaller cooling speed than the latter. As the liquid is cooled in equilibrium at constant pressure, a first order phase transition occurs at T_m and the liquid becomes a crystal following the dark blue line. When the liquid is cooled sufficiently fast, it enters a metastable supercooled regime, while the thermodynamical quantities, such as specific volume and enthalpy, follow the same trend as the equilibrium liquid. Eventually, as temperature decreases, response functions, such as the compressibility coefficient, behave as if the liquid had crystallized. Taken from (7)

η is defined as follows: when a liquid is placed between two parallel solid plates of area A moving with relative velocity v between each other, the force F needed to maintain this velocity is $F = \eta v A/d$, where d is the distance between the plates. The viscosity of water under normal conditions is 10^{-3} Pa s, while a material, cooled with a speed of the order of Kelvin per minute, above the glass transition temperature has a viscosity of the order of 10^{12} Pa s. When this happens, the material is effectively frozen for lab time scales. Therefore, the glass transition occurs at a temperature, T_g, where the viscosity equals 10^{12}. It is also possible to obtain a glass at high pressures, however, we will not consider that scenario throughout this thesis unless otherwise specified.

In 1867, Maxwell suggested that in a short enough time scale, any liquid has an elastic response and behaves like a solid (13). If x is the relative displacement of the plates, the shear displacement γ is defined as $\gamma = x/d$; for a solid the elastic shear modulus G is defined through $\sigma = G\gamma$, where $\sigma = F/A$ is the shear stress. In terms of σ and $\dot{\gamma}$ the definition of viscosity, η, is $\sigma = \eta\dot{\gamma}$. Maxwell proposed to make an extrapolation between the solid and liquid behavior by assuming,

$$\dot{\gamma} = \frac{\sigma}{\eta} + \frac{\dot{\sigma}}{G}\,. \tag{1.1}$$

Notice from Eq. (1.1) that a liquid with steady flow corresponds to $\dot{\sigma} = 0$, while when you have a solid then $\eta = \infty$.

Furthermore, let us suppose an initial condition $\dot{\gamma}(t) = \gamma_0\delta(t)$, which corresponds to an initial displacement. By solving Eq. (1.1) with this initial condition, one finds,

$$\sigma(t) \sim G\gamma_0\Theta(t)e^{-Gt/\eta}\,, \tag{1.2}$$

where $\Theta(t)$ is the *Heaviside* function, and Maxwell's relaxation time is,

$$\tau = \frac{\eta}{G}\,. \tag{1.3}$$

Thus, in general, a liquid behaves like a solid for time scales much less than τ, while for time scales much greater than τ it behaves like a liquid. Generally, the values of G are in the range of $10^9 - 10^{10}$ Pa, therefore, given that $\eta \approx 10^{12}$ Pa s at the glass transition, then τ is in the range of $10^2 - 10^3$ s. With this argument we can say that the transition takes place when Maxwell's relaxation time is of the order of the cooling rate.

The previous derivation is rather coarse-grained, to say the least, yet it gives a picture and pinpoints the important variables to understand the dynamics. The problem in its full dimensions is actually quite complex in the sense that, for instance, the Maxwell's relaxation time depends on the

microscopic processes, such as the molecular characteristic translation and reorientation time. Perhaps an illustrative example of the existance of different relaxation times is the well-known Prince Rupert's drops (PRDs), which made of SiO_2. The story behind the name is beyond the scope of this thesis. However, a PRD looks like window glass in the form of a drop and a long tail as shown in Fig. 1.2. What is interesting in PRDs is that they have exceptional strength properties, all the while if the tail is cut off the whole drop shreds to pieces! The science behind this phenomenon was rather well understood, but it was only until quite recently that it was proved that the drop is under large surface compressive stresses (19). As mentioned previously, as the temperature of the supercooled liquid decreases, its viscosity increases abruptly. In fact, as the temperature changes around three units, the viscosity has a variation over 16 orders of magnitude! Moreover, nothing particularly spectacular happens to the structure during such huge viscosity increase. Now, as mentioned, the necessary cooling speed to form a glass is material-dependent. In order to form a glass window, SiO_2-based melts must be heated to the order of thousands of degree Celsius and then, to cool the liquid and form the glass, it is generally sufficient to put it in contact with air at room temperature (see for instance Ref. (20)). In the case of PRDs, it must be cooled with water at room temperature as shown in Ref. (21). By simply dropping a drop of supercooled liquid in a water bucket. What happens next is quite fascinating. The drop will have different relaxation times. Thus, we may think of a characteristic time function that is space-dependent. Furthermore, notice that since the drop cools from the outside towards the inside, this characteristic relaxation time function is strongly radial-dependent. This dynamical heterogeneity has a huge impact on the glass properties. As the outside layer has solidified, the inner layers are still in the supercooled regime and the specific volume is decreasing (see Fig. 1.1), thus inner layers pull on the outer solidified layers, generating large surface compressive stresses. The underlying idea is that in a supercooled liquid there are different characteristic time scales which are space-dependent. These characteristic time scales have an effect on the internal structure and stress in the glass. Thus, one question we may ask is: *How are characteristic times related to the internal structure of the supercooled liquid?*

Whilst the previous question is valid and interesting from a theoretical point of view, from a technological point of view it is essential. The internal structure of a liquid may be tuned by changing the composition of the given liquid. Hence, a proper understanding regarding the aforementioned question would enable us to tune the characteristic relaxation times at will. Foremost important, we then should be able to elucidate why the viscosity in a supercooled liquid increases exponentially with

Figure 1.2: **left**) Prince Rupert's drop. The color fringes is indicative of residual stresses. **right**) Prince Rupert's drop right after the tail of the drop is cut off. The drop shatters to pieces given the internal stresses this glass has, given the preparation protocol. This also gives PRDs exceptional strength properties (see main text for further details). Taken from the web.

decreasing temperature.

As mentioned, there is a proportionality between the viscosity and Maxwell's relaxation time. One of the best methods for measuring characteristic time scales in liquids and supercooled liquids as well as glasses and crystal is dielectric spectroscopy. This method, however, is only applicable when certain conditions are met by the given material. Since the increase of the characteristic time scales, as temperature decreases, is associated with the slowing down of the molecular dynamics of the given system, then dielectric spectroscopy will only be able to capture this if the entities responsible for the slowing of the molecular dynamics respond to the external electric field. This is true if the entities are charged or exhibit a dipolar moment so that one may see the slowing down molecular dynamics through dielectric spectroscopy (22). On the plus side, dielectric spectroscopy has a broad accessible frequency range and the essence of this method is to measure the dielectric response function of a given material when an external AC electric field is applied to it. The poles in the imaginary part of the dielectric permittivity, also termed *dielectric loss*, yield the resonant frequencies. The inverse of these frequencies are defined as the characteristic relaxation time. In Fig. 1.3 we show the typical behavior of the dielectric loss for *a)* a liquid, *b)* a supercooled liquid, and *c)* a glass. There are several remarks to be made here, the first one being that the Boson peak is related with the transverse normal modes (23), in this sense, crystal do show a Boson peak as well. Nevertheless, the Boson peak is beyond the scope of this thesis. Notice, from Fig. 1.3, that the dielectric loss function in the liquid has a

peak, called the α-peak and as temperature is lowered and the liquid enters the supercooled regime, this peak shifts to lower frequencies while another peak, called the β-peak appears at higher frequencies. The inverse of the frequencies at the α and β peaks are known as the characteristic α- and β-relaxation times, τ_α and τ_β , respectively. Although it is not entirely clear to what kind of miscroscopic process these characteristic times are related to, it is argued that τ_α corresponds to translation movements of the entities (such as atoms, molecules, etc.) and τ_β corresponds to rotational characteristic relaxation times of these entities. Perhaps in the liquid regime the α-peak corresponds to a wide variety of processes, each having relaxation times of the same order, however, as previously mentioned, when the temperature is lowered and the system enters the supercooled regime, the viscosity increases abruptly, which implies that translational movement begins to slow down. Hence, the α-peak in the supercooled regime is associated with translational dynamics. Now, if this is true, in the supercooled regime, $\tau_\alpha \gg \tau_\beta$, thus, for time scales of the order of τ_β, translational movements are effectively halted, which would imply that the entities are caged and only then rotational relaxation becomes relevant (24; 22).

Let us suppose that as we lower the temperature, we compute τ_α. Then, we would obtain something similar to Fig. 1.4 if we plot $\log\tau_\alpha$ on the y-axis instead of the viscosity and $1/T$ on the x-axis. This kind of plot is known as the Angell plot (25). Moreover, this provides a way to characterize glass formers as strong or fragile.

As was mentioned before, the glass transition temperature, T_g, is defined as the one for which the viscosity of the material is of the order of $\approx 10^{12}$ Pa s. Then, fragility index m is defined as the slope of the curves shown in Fig. 1.4 when $T = T_g$, namely,

$$m = \left.\frac{\partial \log(\eta)}{\partial\left(T_g/T\right)}\right|_{T=T_g}. \tag{1.4}$$

This provides a "quantitative" measure of the strong-fragile behavior of the glass former. For small fragile index values, the glass former is said to be a strong glass former, whereas for large fragile index values the glass former is said to be a fragile one. Strong glass formers require a cooling speed smaller than the ones needed for fragile glass formers (7). Loosely speaking, any given physical configuration of a given system will have some internal energy, some degree of degeneracy and some entropy. Thus, from a statistical mechanics stand point, we may map any given physical configuration to a point in a hypersurface corresponding to the energy. This hypersurface will have valleys and barriers as sketched in Fig. 1.5. Given a temperature, the system will be able to visit any point in the hypersur-

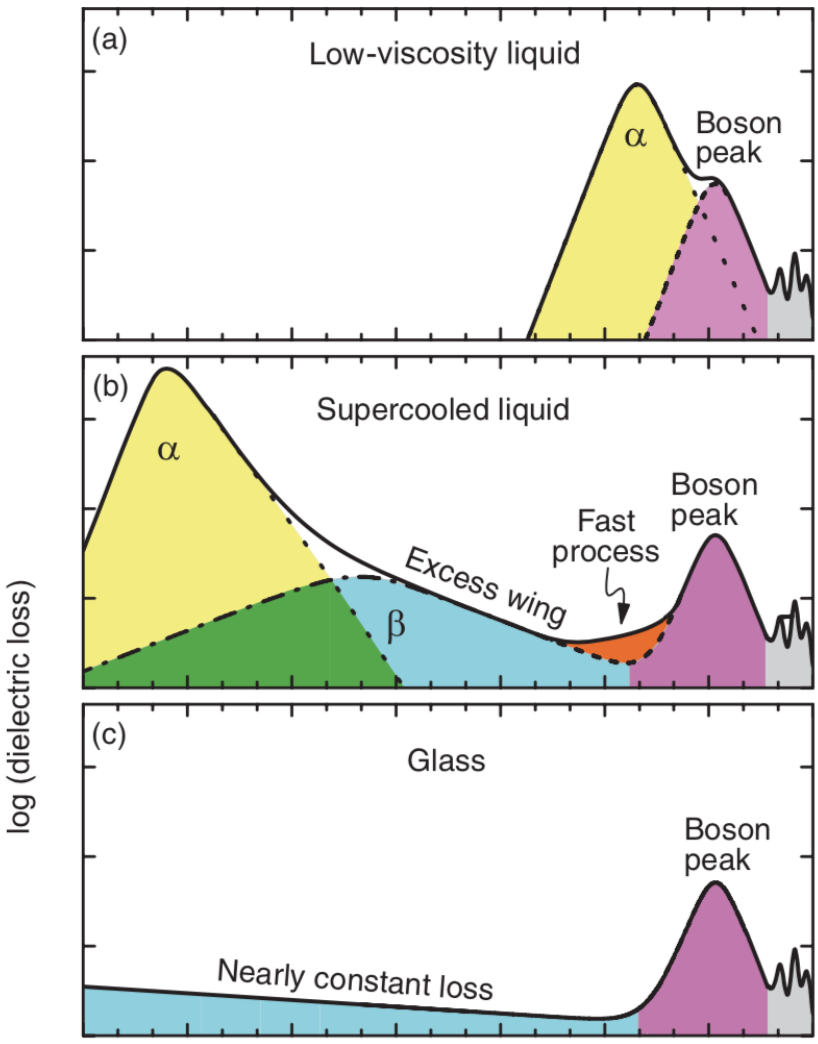

Figure 1.3: Sketch of the logarithm of the dielectric response for a liquid, a supercooled liquid and a glass. The inverse of the frequency where the α and β peaks occur correspond to the τ_α and τ_β relaxation times, respectively. Notice that $\tau_\alpha > \tau_\beta$. In addition, τ_α increases exponentially with the decrease in temperature. Adapted from Ref. (22)

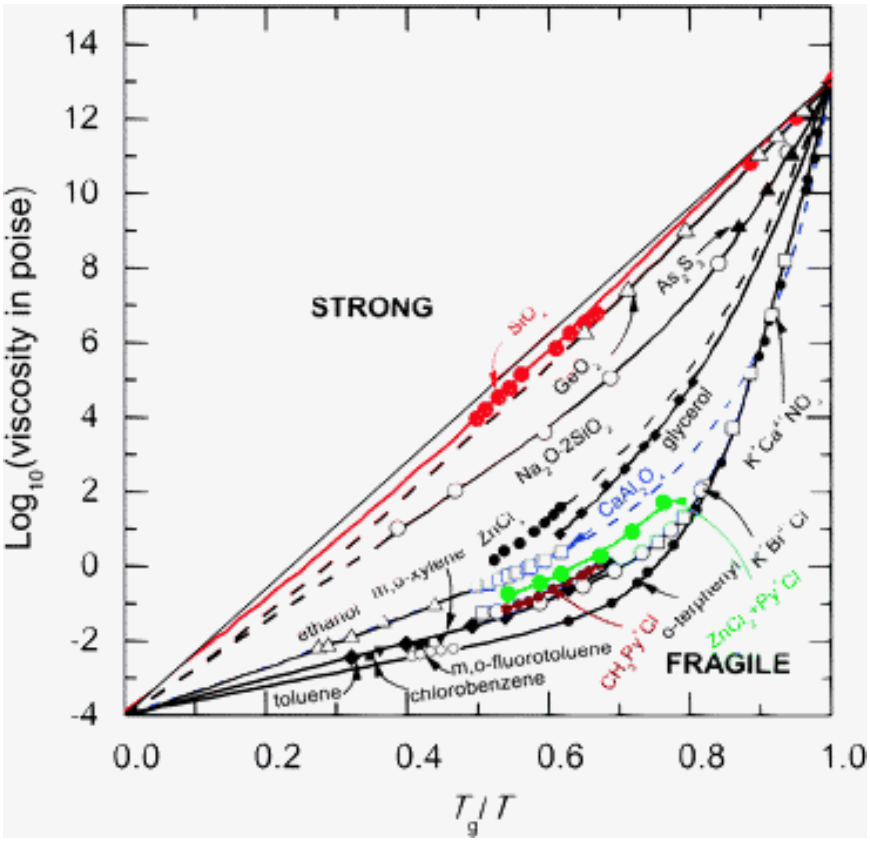

Figure 1.4: Angell's glass classification through viscosity *vs* $\sim 1/T$. The viscosity of strong glasses are usually modeled through Arrhenius Law, while for fragile glasses a spectrum of non-Arrhenius formulas are used. Furthermore, the Volger-Tammann-Fulcher formula is widely used. Taken from Ref. (26)

face that has an energy lower than the temperature times Boltzmann's constant. Under this picture it is easy to see that as the temperature is lowered, the configurational space is reduced and, eventually, if the temperature is low enough, the configurational space available to the system will consist of one single point corresponding to the global minimum of the energy hypersurface, which would correspond to the crystal phase. However, if the temperature is lowered fast enough, the system might become arrested in a local minimum. This local minimum corresponds to the glass state. Then, one could ask the question "*How fast should the temperature be lowered to arrest the system in a local minimum?*". In general, this would depend on the specific topology of the hypersurface. However, one should expect that to answer the former question, only general features of the hypersurface would be necessary [1], but that does not seem to be the case. Having reached this point, we should state that this energy landscape picture is not enough to fully understand the glass transition, but it is useful enough for the purposes of this thesis. Another thing to stress is that the number of metastable states (local minima) grow exponentially with the number of entities (22). In this sense, it is said that the glass state is a very degenerate state.

The literature regarding the nature of strong and fragile glasses is vast, but one must dive into it with much care as the rabbit hole goes far down. Nevertheless, several ideas are worth emphasizing, namely,

- Perhaps not the most useful way, yet the most common way in classifying glasses is under the strong-fragile prism.

- The viscosity for strong glasses follows the Arrhenius law, while the viscosity for fragile glasses are usually modeled using the the Volger-Tammann-Fulcher formula (13; 16).

- The dynamics of strong glasses are, ultimately, driven by activation energies. For fragile glasses, entropy seems to play a crucial role.

There are many models that try to explain the glass transition from a dynamical approach. At some point, the holy grail was to make dynamics and thermodynamics meet. This was one of the strong points in the Adams-Gibbs model. This is beyond the scope of this thesis, but for a very nice review, see Ref. (13).

[1] Similar to solid state physics and many other fields where the central limit theorem and its corollaries play a crucial role in averaging and simplifying things.

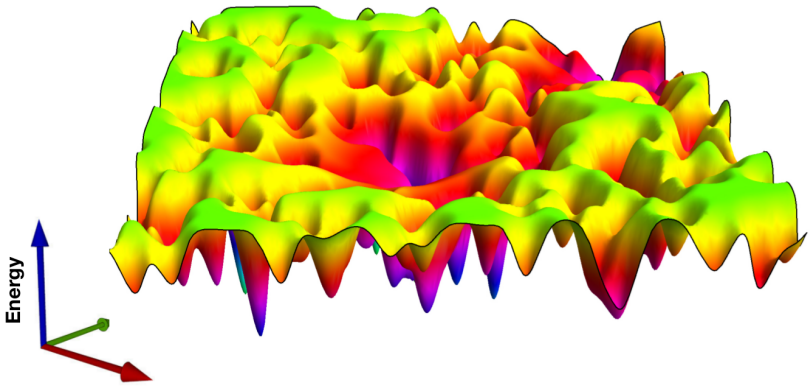

Figure 1.5: Free energy landscape sketch. In this sketch, the system as a whole moves over the XY plane, while the Z corresponds to the energy. Each point in the energy landscape corresponds to a system configuration. Notice that different configurations may have the same energy (same value in the Z-axis). Additionally, to go from one minimum to another, the system has to cross an energy barrier as well as to take into account the curvature of the minimum. Take from Ref. (27)

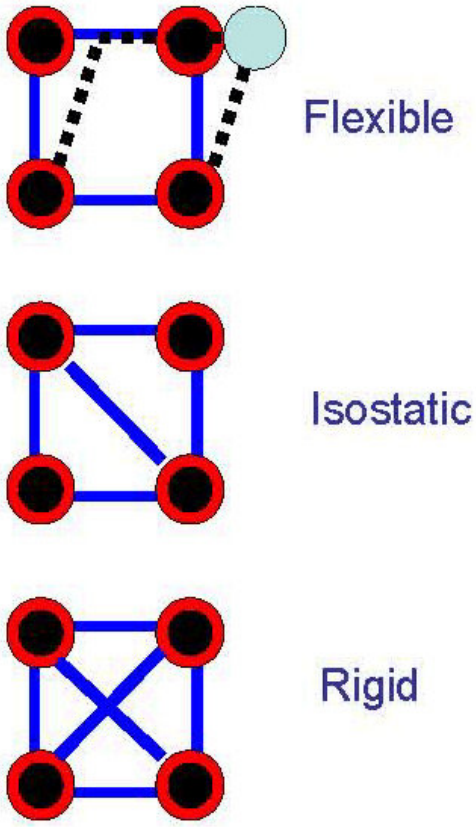

Figure 1.6: Sketch of a underconstrained (upper panel), isostatic (central panel) and overconstrained system (lower panel). When a system is underconstrained, there are floppy modes, i.e., vibrational modes such that the eigenvectors associated to these floppy modes point in directions where the system may flow without losing energy. From the rigidity theory standpoint, the isostatic system corresponds to a finite coordination number value where the number of constraints equal the number of freedom degrees. By increasing the coordination number, the number of constraints surpasses the number a degrees of freedom and the system becomes overconstrained. Rigidity theory relies completely on the coordination number in order to determine rigidity. Take from Ref. (28)

As already mentioned , one of the foundations in current glass research is the constraint rigidity theory of Phillips and Thorpe (29; 30). This helped to understand the supercooled behavior of chalcogenides. The underlying idea is that by changing the coordination number the necessary cooling rate for glass forming tendency varied. To modify the coordination number, the chemical composition is varied and used as a proxy. A first result was realizing that there is a critical coordination number at which the necessary cooling rate is minimum. This critical coordination number is equal to 2.4. They further realized that this result is obtained when the number of constraints equals the number of degrees of freedom. Phillips compared this theory with actual experiments (see Fig. 1.7 (a)) of the time and obtained a fairly nice agreement between theory and experiment. Then, Thorpe introduced the notion of rigidity threshold and, through a mean field approach, realized that the critical coordination number corresponded to the rigidity threshold. But the story does not end there. A simple way to grasp these ideas is shown in Fig. 1.6 where we show a network of four nodes with (upper panel) four edges in which case the network has a direction where it may be deformed without doing work. As we increase in one the number of edges (center panel) the network becomes isostatic (i.e., the network may not be deformed without doing work). In this case, the number of constraints equals the number of degrees of freedom. We may add another edge (lower panel) in which case this lead to the overconstrained configuration. In real systems, such as chalcogenides, the number of edges is tuned by changing the concentration of the substances in question.

A little over twenty years after Phillips' paper came out, Boolchand (31; 32) experimentally found that rather than a critical value, there is in fact a window over which the glass melt properties change dramatically, as shown in Fig. 1.7 (b). This was further supported by simulations (33). This window was coined as the *intermediate phase* (see Fig. 1.7 (c)). Since then much controversy has surrounded this intermediate phase and, to be fair, it is still a subject of heated debate. Nevertheless, there is supporting evidence that properties such as the viscosity, the molar volume and the enthalpy experience a dramatic change when entering this window (34). Additionally, it has been shown that glass formers in this intermediate phase are reversible in terms of heat absorption and release at the glass transition, and also become strong in terms of dynamical fragility. These features are singular with respect to those of the glass formers out of the phase. On the other hand, calorimetry experiments imply a first-order phase transition in some strong glass-forming liquids above the glass transition temperature. There, we assume the existence of this phase transition.

Still, no one has been able to produce a coherent theory to account for the empirically found

relationship between relaxation and rigidity. In fact, it is worthwhile mentioning that there are several thesis that deal with rigidity in disordered systems as well as relaxation in glass melts, yet there hasn't been a thesis that deals and relates both properties. Here we relate them and provide such a theory.

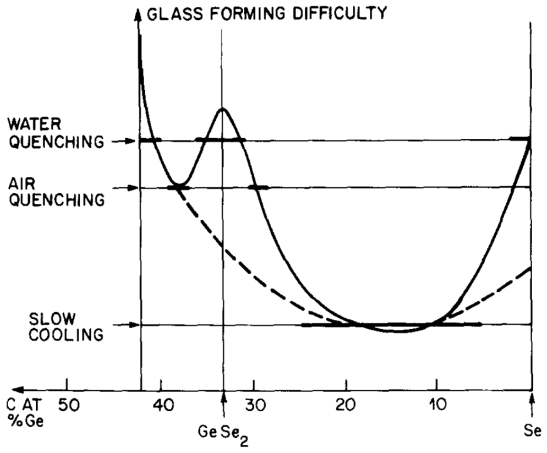

(a)

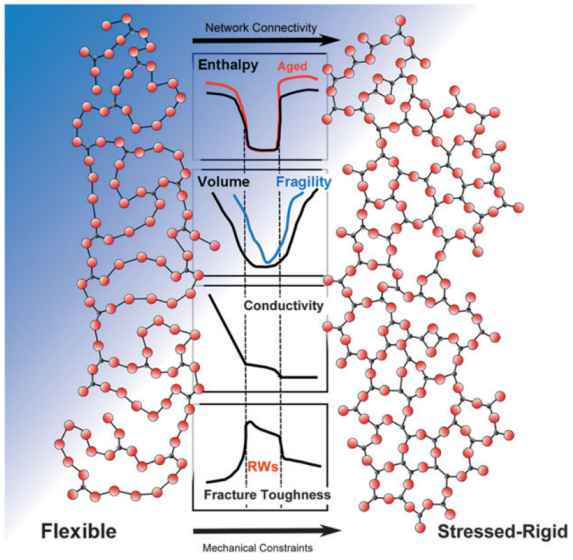

(b)

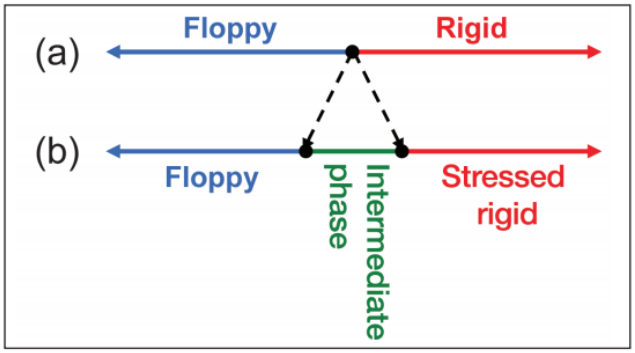

(c)

Figure 1.7: **a)** Glass forming difficulty. As the concentration is varied, the mean coordination number changes. This affects the glass forming tendency. Taken from Ref. (29). **b)** Thermodynamical and dynamical features variation with composition. Taken from Ref. (34). **c)** Schematic view of the intermediate phase. Taken from Ref. (35).

1.2 Outline of the thesis

The second chapter deals with the relaxation dynamics in glass forming models. First, we study a simple solvable glass model from the energy landscape point of view. This model has a first order phase transition to a crystal as well as a dynamic transition to a glass. In this model we are able to relate the relaxation time and the short time dynamics as well as the minimum cooling speed for a strong glass forming tendency. We show how the vibrational modes, together with the energy barriers, determine the relaxation. Our strategy consists on using Kramers' transition state theory. Then, we present a non-linear, non-deterministic, zero temperature model where we study the floppy modes relation with energy barriers and the latter with the relaxation time. We find a broad range of relaxation times scales that arise from dynamical heterogeneity. We further pinpoint the plethora of initial configurations to understand how this exponential relaxation times appear. This, we discuss, is useful in glass dynamics such as molecular rearrangements usually related with the β-relaxation. Then we present the conclusions of the chapter while setting the tone for the next chapter.

The third chapter is concerned with the rigidity aspects. We first study the relationship between rigidity and floppy modes by means of simulation of hard-disks. We present the concept of dynamical-gap and show its usefulness in characterizing rigidity, counting floppy modes and using it as a order parameter. Then, we present a model which shows how floppy modes emerge through maximization of vibrational entropy. We then relate this with the heterogeneous-homogeneous phase transition.

The fourth chapter presents the conclusions. Additionally, there are six appendices which complement the ideas and derivations throughout the main text. The whole text has been written to be self-contained.

Chapter 2

On the relaxation properties of glass forming systems

2.1 Introduction

Relaxation processes are ubiquitous in the Universe. In fact, if one were to take a snapshot of the Universe, one would see that only a few number of physical systems are in equilibrium, while the rest are either in steady states or relaxing towards equilibrium. All the same, it is not clear how relaxation processes depend upon the energy landscape (12; 36; 16; 22; 37; 38). It is of common knowledge that this is due to mainly two contributions, one being the energy landscape complexity itself, and the other being the interaction with the sourrounding of the system. However, even if we only consider the complexity of the energy landscape, one would find that the system has an intermittent chaotic behavior. In this way, the deterministic feature is meaningless, similar to what happens in stochastic processes (39). Furthermore, what we call stochastic behavior and chaotic behavior seems to be two faces of the same coin (40). In this sense, Alvaro *et al.* in (41) are able to establish this sort of correspondence for two particular well-known stochastic models.

In order to guarantee that the system under study will tend to an equilibrium state, one usually imposes detailed balance or assumes that the conditions are fulfilled for the fluctuation-dissipation theorem or the equipartition theorem. However, this is not obvious when going from a classical mechanical to a statistical mechanical approach. As it is well known, this is what Fermi, Pasta and Ulam investigated back in 1954, by considering a chain of nonlinear oscillators. What they found is quite long to sumarize here (see (42)). However, as one would expect, this relaxation depends strongly on

the mode-coupling, i.e., the non-linear terms. In fact, Ponno in Ref. (43) presents some estimates on how the energy is transfered from one mode to another, as well as the characteristic relaxation time which is proportional to the number of oscillators. What is even more interesting is that this energy sharing starts in the low vibrational modes due to resonances, which was first pointed out in Ref. (44). This is because the dispersion relation for the low vibrational modes is linear and the frequencies are linearly dependent. Then each mode will resonate with their mode-coupling term. Here is a hint on the importance of the low vibrational modes in the relaxation properties.

Nonetheless, the relaxation mechanism, in particular, in supercooled liquids, has proven to be very complex. In fact, the general features of supercooled liquids still lack a scientific explanation, because of their complex nature. On the one hand, the problem is difficult because the harmonic approximation breaks down for the Hamiltonian at long-time scales, which are relevant to describe the relaxation and viscosity properties of glassy melts (12). On the other hand, the glass transition is a non-equilibrium transition problem where the system does not have long range order. These arguments are just the tip of the iceberg that give foundation to why this problem is a very complex one. Despite the amount of research focused on it (see (45–50; 4; 15) and in particular (13) and references therein), there is not too much of a consensus and rather different points of view. To spice things up a little, experiments and simulations have not yet met in the sense that it takes too much computational time to drive the system towards a region near the glass transition temperature. Yet attention should be payed on recent simulations (51).

One of the questions that arise about this phenomenon is how the glass transition temperature, T_g, is related to the composition of the glass former (1; 3). Rigidity theory (18; 52–55) gives some insight on this aspect in a qualitative manner, and works quite well in the case of chalcogenide glasses. Another rather interesting feature of supercooled liquids is the viscosity behavior during a quench. As is well known, viscosity is a property that depends upon relaxation, i.e., the time that the system takes in order to leave a basin of the energy landscape and produce a structural relaxation. Depending on this behavior, the supercooled liquid is classified as strong if it follows the Arrhenius equation and as fragile if it follows the Vogel-Fulcher-Tamman equation (13; 16). The fragility or non-fragility of a supercooled liquid is related with the glass forming tendency in the sense that strong supercooled liquids have a strong glass forming tendency such that do not require large quenches in comparison with fragile ones which are poor glass formers. Thus, the glass forming tendency is clearly related with the relaxation times of the system.

It is well known that there is a correlation between the glass transition temperature, T_g, and the cooling rate. Quite recently, Lerner *et al.* in Refs. (56; 57) have shown that the statistics and localization of low-frequency vibrational modes depend upon the cooling rate. Thus, there lies a trichotomy, namely, glass transition, relaxation and low-frequency vibrational. This has been, further, discussed in Refs. (58–60; 23; 61; 62). In fact, rigidity theory has allowed to rationalize how they are interrelated(14). As already mentioned, in their rigidity theory, Phillips and later Thorpe, consider covalent bonding as a mechanical constraint(18; 52). In this sense, one may summarize the main feature of this theory as follows. When the number of bond constraints equals the number of degrees of freedom, the glass forming ability is optimized, i.e., producing glass requires the slowest cooling rate. In this situation, the mean coordination number equals the critical percolation coordination number, i.e., domains of floppy modes (zero frequency modes) and rigid modes coexist. As the mean coordination number decreases, which may be tuned by varying the chemical composition, floppy mode domains grow while rigid mode domains disappear. As floppy modes increase in number, the glass formation is more difficult. We stress the previous through the thesis (as the reader may have noticed) because of its importance. This sets the baseline for this thesis.

In this chapter we first present a simple solvable two-level glass forming model which has a first order phase transition to a crystal, while also having a dynamical transition to a glass when cooled fast enough. In this model we are able to analytically relate short time dynamics with long time relaxation properties. We do this by modeling the system from an energy landscape approach. One caveat under this approach is that the topology of the energy landscape is subject to changes as temperature varies, hence the difficulty to mathematically model it, in addition to the topological complexity as can be seen in Fig. 2.1 which is what an energy landscape actually looks like. What lacks in the two-level model is the correlation between vibrational modes and energy barriers. To address this issue, we present our findings on the relaxation behavior when we decrease the energy barriers which are coupled with the frequency of the normal modes. When the energy barriers decrease so does the vibrational modes which then yield floppy modes. Our approach is base on a chain formed by three non-linear oscillators, which yields the Hénon-Heiles potential when expressed in the coordinates that diagonalize the linear part. This potential is a particular case of the Fermi-Pasta-Ulam (FPU) model, in which it is known that low-frequency modes are responsible for relaxation (63–66). This has been made by adding second-neighbours, disorder and quasiperiodicity (64; 65; 67; 68). The advantage of the Hénon-Heiles model (69–74) is that it contains the minimal ingredients to understand the

effects of non-linearity.

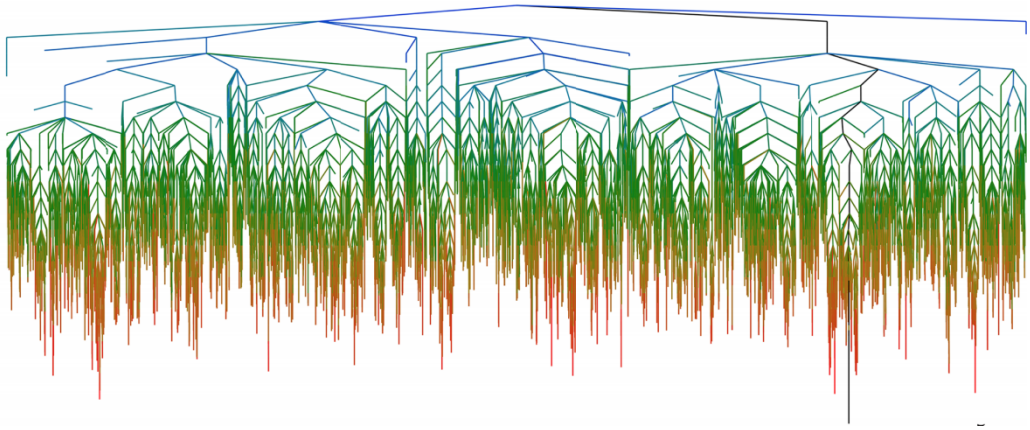

Figure 2.1: Energy landscape of a supercooled liquid *in silico*. Each end node corresponds to a system configuration, while the edges resemble the connected configurations. Obtained from Ref. (75)

It is worthwhile mentioning the results from Zwanzig (see Ref. (36)) where he shows that if we take a particle coupled to N harmonic oscillators, by appropriately choosing the memory function, it is possible to obtain the Langevin Equation. This is conceptually important in order to understand the connection between the two models discussed in this chapter. Concerning the escape dynamics, it has been observed the fact that the phase space escape flow follows an exponential law connected to chaotic dynamics, whereas in non-chaotic dynamics the phase space escape follows a power law. Using simple arguments, Zhao *et al.* (74) obtained the exponential law, which they then compared succesfully with their simulations in the case of chaotic dynamics, with a small threshold energy. Bauer and Bertsch (76) also obtained the exponential law before Zhao *et al.* Furthermore, from a heuristic and retrospective approach they obtained the power law. Here we show that there is the crossover between exponentially decaying law and power law which is not seen in (74) because they consider smaller threshold energies and short times.

The next section treats the simple solvable two-level glass forming model under a quench. In section 2.3 we present the soften-Hénon-Heiles model, its features and results. Finally, in section 2.4 we summarize and conclude this chapter.

2.2 Simple solvable two-level model

2.2.1 Glass transition two-level model

Let us, in a brief manner, define the model to be used for the glass transition (for a detailed description see (59)). As seen in Fig. 2.2, the energy landscape is composed of g_1 wells with energy $E_1 = N\epsilon > 0$ which we denote as the meta-stable states for N atoms in total, and $g_0 (\ll g_1)$ wells with energy $E_0 = 0$ which we denote as ground states. All wells are interconnected, and any two wells have an in-between wall of height V.

Now, given this simple topology, we assume that transition probabilities between the wells in the metastable state are all the same, in like manner transition probabilities between the wells in the ground state are all the same. The transition probability from each well in the metastable state to any of the wells in the ground state are all the same as well as the transition probability from each well in the ground state to any of the wells in the metastable state. The probability $p(t)$ of finding the system in the metastable state satisfies the following master equation(59):

$$\dot{p}(t) = -\Gamma_{10} g_0 p(t) + \Gamma_{01} g_1 \left(1 - p(t)\right) , \tag{2.1}$$

where Γ_{10} corresponds to the transition probability per time for going from the state with energy E_1 to the ground state, i.e., state with energy 0, and Γ_{01} for the reverse transition. Now, let us use Kramers' theory to take into account in a proper way contribution from the curvature of the basin. To do this, we consider that the square well model must be replaced by a smooth potential. Since the square well model can be reduced to a model of two levels with degeneracy, then the model with the smooth potential can be translated into a landscape with the shape shown in Fig. 2.3 with the same degeneracy as in the original square model.

According to Kramers' first passage time formulation in the overdamped scenario (36; 77; 78) (see Appendix A for details in the derivation), one finds that

$$\begin{cases} \Gamma_{10}(T) = \frac{\omega_1 \omega_c}{2\pi\gamma} e^{-V/T} , \\ \Gamma_{01}(T) = \frac{\omega_0 \omega_c}{2\pi\gamma} e^{-(V+E_1)/T} , \end{cases} \tag{2.2}$$

where $\omega_1^2 \equiv V''(x_1)/M$ is the squared angular frequency inside the metastable minimum at position $x = x_1$ and M is the mass of the system. $V''(x)$ denotes the second derivative of the potential at x. $\omega_0^2 \equiv V''(x_0)/M$ is the squared angular frequency inside the global minimum at position $x = x_0$ and

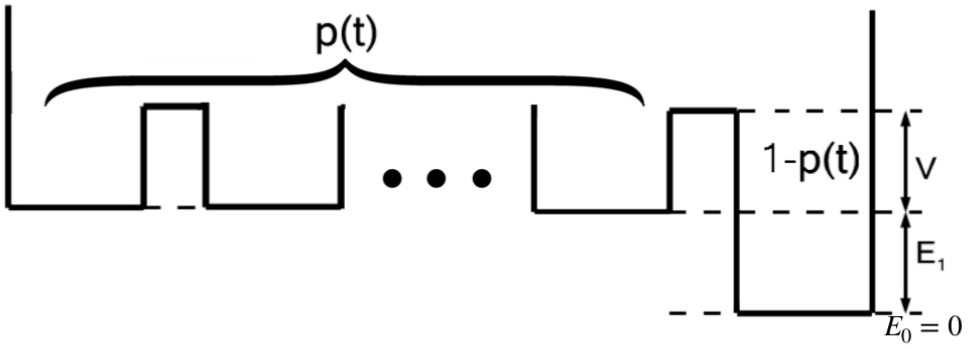

(a)

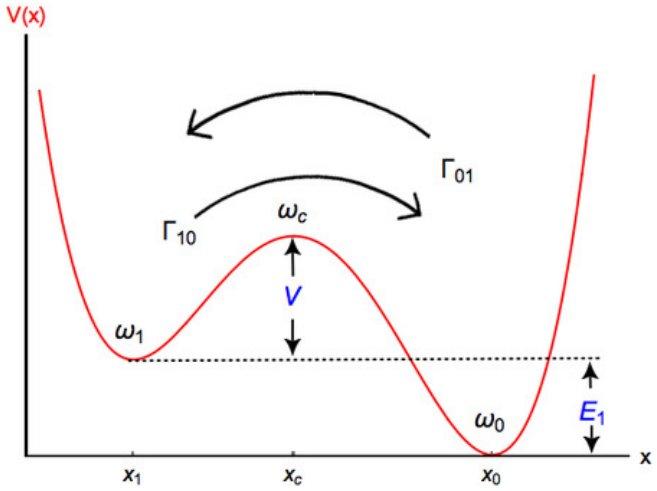

(b)

Figure 2.2: (**upper panel**) The two level system energy landscape, showing the barrier height V and the asymmetry E_1 between the two levels and the low energy $E_0 = 0$. There are g_1 wells with energy E_1, associated with metastable states, and g_0 ground states with energy $E_0 = 0$. The population of the upper well is $p(t)$ (59). (**lower panel**) The double well embedded with the specified parameters in the model.

$\omega_c^2 \equiv |V''(x_c)|/M$ is the squared angular frequency at the transitional state at position $x = x_c$ (see Fig. 2.2 (b)). Also, the energy potential barrier height that appears in Eq. (2.2) is given by V, which is

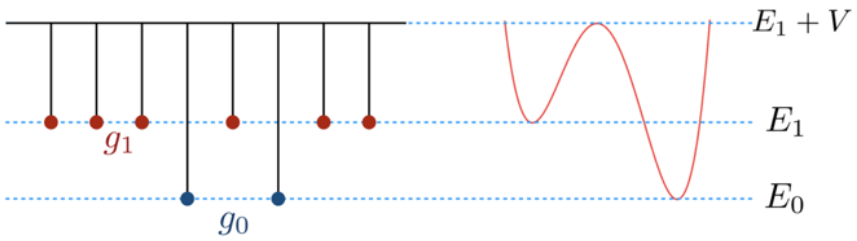

Figure 2.3: Sketch of a double well potential with a barrier of height V, showing the frequencies associated with each well and transition barriers. The transition rates between wells are also shown with arrows.

defined as $V = V(x_c) - E_1$. Here we denote the dissipation coefficient as γ and is fixed at $\gamma = 1$.

For real glasses, ω_1 and ω_0 depend upon the normal modes frequencies at the energy minima (55; 23; 60). Here is important to remark that in general, the potential barrier height V can be correlated with the surrounding energy minima. In this sense, the normal modes frequencies and the energy minima of the energy landscape is known for a variety of interaction potentials (79; 80). Also, the energy barriers distribution (81) and the Hessian index (82) as function of temperature has been obtained for Lennard-Jones supercooled liquids. As was mentioned, the topology of the energy landscape changes with temperature, in addition to its topological complexity. In this sense, perhaps the use of tools such as the ones provided by catastrophe theory might be useful, as pointed out by Wales in (83). Nonetheless, the relation between the transition barrier heights and the frequencies is still an open issue, but certainly they can be correlated (84). Throughout this section, V is treated as an independent parameter that may or may not be correlated with the frequency ω at the bottom of the adjacent wells. Here we only need the maximum value of $V(x)$, identified with V, and a finite $V''(x)$ at such point. In that sense, our model describes a general situation of an energy barrier and two adjacent minima. In reality, one needs to include many energy minima and barriers between them as well as correlations between energy minima, barrier height and curvature, and the fact that in real glasses, there is a *distribution of energy barriers, energy minima and curvatures* that are needed to be overimposed on our minimal picture of the landscape.

It is worthwhile mentioning that the transition rates shown in Eq. (2.2) satisfy the detailed balance condition,

$$\frac{\Gamma_{01}}{\Gamma_{10}} = \frac{\omega_0}{\omega_1} e^{-E_1/T}, \tag{2.3}$$

Also, it is important to observe that the stationary solution to our master Eq. (2.1) is:

$$p_0(T) = \frac{\frac{g_1\omega_0}{g_0\omega_1}e^{-E_1/T}}{1+\frac{g_1\omega_0}{g_0\omega_1}e^{-E_1/T}}\,. \tag{2.4}$$

In general, the degeneracies g_0 and g_1 depend upon the landscape complexity, which increases as $\sim N!\exp(N)$ (49; 85; 86). Here we assume $g_0 = \exp\left(N\log(\Omega_0)\right)$ and $g_1 = \exp\left(N\log(\Omega_1)\right)$ where $\Omega_1 > \Omega_0 = 1$. Therefore, in the thermodynamic limit, when $T < T_c$ then $p_0(T) = 0$, while when $T > T_c$ then $p_0(T) = 1$, where T_c is the first order transition temperature and is defined by the equality [1]

$$T_c = \frac{\epsilon}{\log\left(\Omega_1/\Omega_0\right)}\,. \tag{2.5}$$

In equilibrium, the system at $T < T_c$ is in the crystalline state while when $T > T_c$ it represents the liquid. When the system experiences a quench, the system may be arrested in metastable states. This will be presented in the following.

2.2.2 Cooling speed and residual population

Let us study our model under cooling. In that case, a cooling protocol, i.e. the temperature as a function of time, $T(t)$, needs to be specified. Experimentally, a linear cooling is usually used. For obtaining analytical results, an hyperbolic quench is more appropriate. Both cooling protocols produce similar results, except for the size of the glass transition region, associated with the boundary layer of the differential equation (87; 59). This boundary layer decrease as N increases. For the hyperbolic quench, $T(t) = T_0/(1+Rt)$ where T_0 is the initial temperature at which the system is in thermal equilibrium and R is the cooling rate. In particular, we are interested in the system's dependence with ω_1 when a rapid quench is applied.

Notice that care must be taken with our notation. Here $T = T(t)$, and as a result, the population described by Eq. (2.1) will be denoted at times by $p(T)$, which should not be confused with the equilibrium probability $p_0(T)$. Having said this, let us write Eq. (2.1) as follows:

$$\dot{p}(t) = -\frac{\omega_c}{2\pi\gamma}\left(\omega_1 g_0 e^{-\frac{V}{T(t)}} + \omega_0 g_1 e^{-\frac{(V+E_1)}{T(t)}}\right)p(t) + \frac{\omega_0\omega_c}{2\pi\gamma}g_1 e^{-\frac{V+E_1}{T(t)}}\,. \tag{2.6}$$

The solution to this first order non-homogeneous ordinary differential equation is obtained in a

[1] Here and on, when taken the thermodynamic limit we will assume $\Omega_1/\Omega_0 > 1$.

straightforward manner yielding the following:

$$p(t) = \exp\left[\frac{\omega_c T_0 e^{-\frac{V}{T(t)}}}{2\pi\gamma R}\left(\frac{\omega_1 g_0}{V} + \frac{\omega_0 g_1 e^{-\frac{E_1}{T(t)}}}{V+E_1}\right)\right] \times \left[p(\infty) - \int_t^\infty dt' \frac{\omega_0\omega_c}{2\pi\gamma} g_1 e^{-(V+E_1)/T(t')} \exp\left(-\frac{\omega_c T_0 e^{-\frac{V}{T(t)}}}{2\pi\gamma R}\left(\frac{\omega_1 g_0}{V} + \frac{\omega_0 g_1 e^{-\frac{E_1}{T(t)}}}{V+E_1}\right)\right)\right]. \quad (2.7)$$

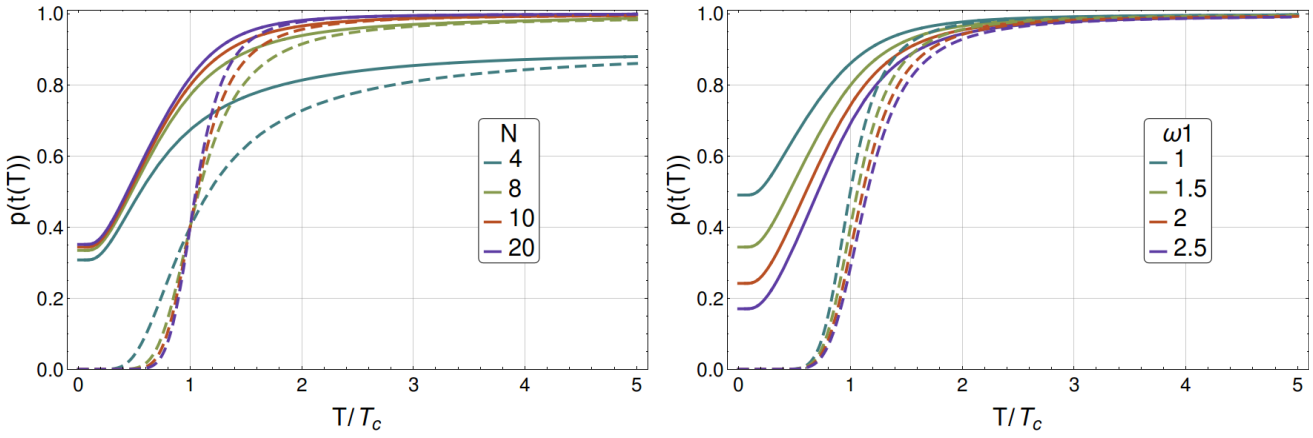

(a) (b)

Figure 2.4: Temperature dependent distribution in equilibrium (dashed lines) and under fast cooling (continuous lines). We parametrize the time dependent probability with temperature, i.e., $p(t(T))$. Given the cooling protocol, the system may be arrested in a metastable state. In (a), the size of the system is changed for a given cooling ratio. The parameters were fixed at **(a)** $V=1$, $\gamma=1$, $R=1$, $\omega_c=1$, $\omega_0=1$, $\omega_1=1$, $\epsilon=1$,$\Omega_0=1$, $\Omega_1=2$, since we are solely interested in the dependence with N and the change in behavior when a cooling speed is taken into account. In panel **(b)**, the size and cooling rate is fixed, while the oscillation frequency of the metastable energy basin is modified. Observe that the glass forming ability increases as the oscillation frequency ω_1 of the metastable states goes to zero. The reason is that the system probes the energy barrier less frequently. The parameters are $V=1$, $\gamma=1$, $R=1$, $\omega_c=1$, $\omega_0=1$, $N=8$, $\epsilon=1$,$\Omega_0=1$, $\Omega_1=2.$, since we are only interested in the effect of the frequency ω_1 has in the glass forming tendency.

Now, in order to find the residual population $p(\infty)$ corresponding to $t\to\infty$ which gives the probability of arresting the system in the metastable states as $T\to 0$, we first assume that the system is initially in thermal equilibrium at a temperature T_0 such that $T_0 > T_c$. Hence we write:

$$p(\infty) = p_0(T_0)\exp\left(-\frac{\omega_c T_0 e^{-\frac{V}{T_0}}}{2\pi\gamma R}\left(\frac{\omega_1 g_0}{V} + \frac{\omega_0 g_1 e^{-\frac{E_1}{T_0}}}{V+E_1}\right)\right) + \int_0^\infty dt' \frac{\omega_0\omega_c}{2\pi\gamma} g_1 e^{-(V+E_1)/T(t')} \exp\left(-\frac{\omega_c T_0 e^{-\frac{V}{T(t)}}}{2\pi\gamma R}\left(\frac{\omega_1 g_0}{V} + \frac{\omega_0 g_1 e^{-\frac{E_1}{T(t)}}}{V+E_1}\right)\right). \quad (2.8)$$

In Fig. 2.4 we have plotted p given by Eqs. (2.4) and (2.7) as function of T, while in Fig. 2.5 we have plotted $p(\infty)$ given by Eq. (2.8). Notice, from the lower panels in both figures, how the residual population increases as ω_1 decreases, i.e., as the metastable wells become broader. This agrees with the first passage time of a non-drifting Brownian particle (see Ref. (88) for instance). Notice that as ω_1 tends to zero, the well becomes flat. Hence, the system can be thought of as a one-dimensional free Brownian particle. In this scenario, at long times, the first passage time distribution goes as $\sim t^{-3/2}$. Thus, the mean first passage time diverges, which means the particle takes an infinite time in going from the metastable state to the ground state. This is what the lower panels in Figs. 2.4 and 2.5 are suggesting.

As previously mentioned, prior to the glass transition, the characteristic relaxation time increases. When this time is of the order of the observation time, then the supercooled liquid is not able to remain in equilibrium and the glass is formed. This characteristic relaxation time is obtained in the following.

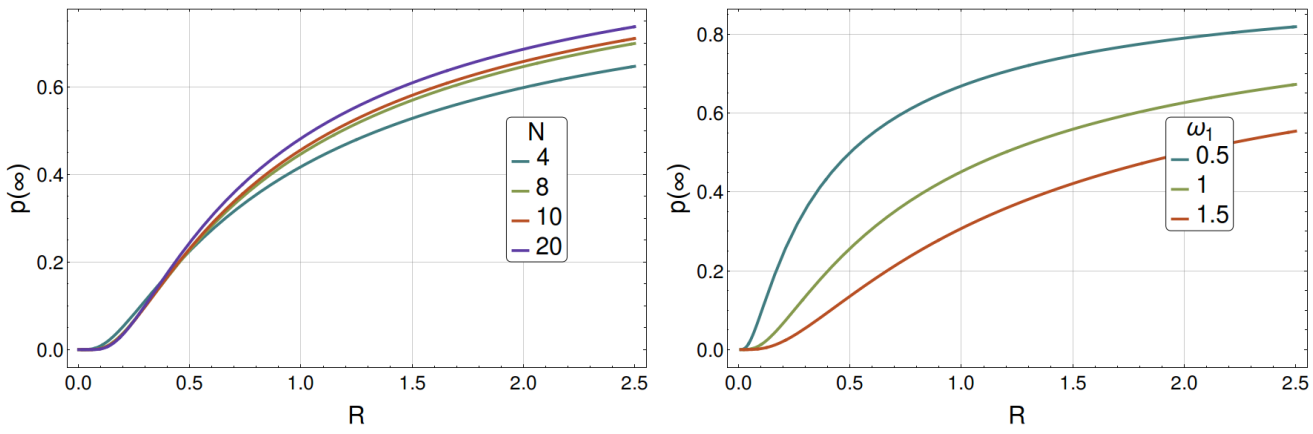

(a) (b)

Figure 2.5: Final state quenched distribution as a function of the cooling rate as obtained from Eq. (2.8). In panel (a), the size of the system is changed. The parameters were fixed at **(a)** $V = 1$, $\gamma = 1$, $T_0 = T_c$, $\omega_c = 1$, $\omega_0 = 1$, $\omega_1 = 1.1$, $\epsilon = 1, \Omega_0 = 1$, $\Omega_1 = 2$, since we are solely interested in the dependence with N. In panel **(b)**, the oscillation frequency of the metastable energy basin is modified. Observe how as the frequency $\omega_1 \to 0$, the glass forming ability increases for a given cooling rate R. Again, the reason is the decreasing probing of the energy barrier. The parameters are $V = 1$, $\gamma = 1$, $T_0 = T_c$, $\omega_c = 1$, $\omega_0 = 1$, $N = 4$, $\epsilon = 1$, $\Omega_0 = 1$, $\Omega_1 = 2$, since we are solely interested in the dependence with the frequency ω_1.

2.2.3 Characteristic relaxation time

Glass formation happens as a dynamical transition, i.e., glasses appear because the system is not able to relax into the energy minimum. In this simple model we can test this idea in a simple way. To determine the characteristic relaxation time, let us assume that at any fixed given temperature T, the initial condition is $p(t=0)=\rho$, where $0\leq\rho\leq 1$. Now, because of detailed balance, we know that for a *fixed temperature* $p(t\to\infty)=p_0(T)$. Hence, we formally write:

$$\begin{cases} \dot{p}(t) = -\Gamma_{10}(T)g_0 p(t) + \Gamma_{01}g_1\left(1-p(t)\right) \\ p(t=0)=\rho \\ p(t\to\infty)=p_0(T) \end{cases} . \tag{2.9}$$

By simple inspection, one is able to write the solution,

$$p(t) = p_0(T) + \left(\rho - p_0(T)\right)e^{-t/\tau} . \tag{2.10}$$

where the characteristic relaxation time τ is:

$$\tau = \frac{1}{\Gamma_{10}g_0+\Gamma_{01}g_1} = \frac{2\pi\gamma}{\omega_c\omega_1}\frac{1}{e^{-(V/T+F/T)}} , \tag{2.11}$$

where F is the free energy, i.e.,

$$F = -T\log\left(g_0 + g_1\omega_0\exp\left(-E_1/T\right)/\omega_1\right). \tag{2.12}$$

Notice that in Eq. (2.11), in the thermodynamical limite τ is proportional to the oscillation period multiplied by the inverse conditional probability $\mathscr{P}(V+E_1|E_1)$. Before continuing, let us stress the following. When $\gamma\gg 1$ the system is strongly coupled with the heat bath, thus it dissipates energy at a very high rate. On the contrary, when $\gamma\to 0$ the system is weakly coupled with the heat bath, which are responsible for the fluctuations in the system which in turn are responsible for the barrier crossing. However, Eq. (2.11) does not apply for the latter case. Instead, one may use Kramers' transition state theory in the underdamped regime (see for instance (78; 36; 89))

In the thermodynamical limit, the characteristic relaxation time below the critical temperature goes as $2\pi\gamma/\left(\omega_c\omega_1\Omega_0^N\right)\exp\left(V/T\right)$. Despite stating the obvious, notice that as ω_1 decreases, the characteristic relaxation time increases. As stated earlier, when ω_1 tends to zero, the energy landscape changes in such a way that the available phase space increases. Hence, it takes longer for the particle to visit the "summit" or probe the energy barrier . Therefore, the characteristic relaxation time increases as ω_1 tends to zero. In this limit, such a degree of freedom becomes a floppy mode. As we discuss in the following, this affects the critical cooling rate for glass formation.

2.2.4 Thermodynamic limits and critical cooling rate

Let us first consider the thermodynamical limit $N \to \infty$ for expressions $p(\infty)$ and $p(t)$. In this scenario, from Eq. (2.8) we obtain for $p(\infty)$ the following expression:

$$p(\infty) = \exp\left(-\frac{\Gamma_{10}(T_c)T_0}{RV}\right). \tag{2.13}$$

Arguing the same way, one obtains from Eq. (2.7) for $p(t)$ the following result:

$$p\left(T(t)\right) = \begin{cases} 1, & T(t) \geq T_c \\ \exp\left(\frac{\Gamma(T(t))T_0}{RV}\left(1 - e^{V\frac{T_c - T(t)}{T_c T(t)}}\right)\right), & T(t) \leq T_c, \end{cases}$$

We define the critical cooling rate as the cooling rate for which the residual population has an inflection point, to obtain the following relation:

$$R_{\text{crit}} = \frac{\omega_1 \omega_c T_0}{4\pi\gamma V} e^{-V/T_c}. \tag{2.14}$$

This equation relates the cooling rate with the short-time dynamics in the model which is one the main result of this work. In the following section, we will discuss its properties and validity.

Notice that Eqs. (2.11) and (2.14) provide a link between long and short-time dynamics for a simple landscape. Let us know discuss some important points concerning its application in real systems.

The first is to observe that in Eq. (2.14), R_{crit} is linear on ω_1. As $\omega_1 \to 0$, the relaxation time grows. The reason is simple to understand. As the energy well flattens, the time spent by the system close to the dividing energy barrier goes to zero and the probability of escape decreases. In other words, the frequency of oscillation is roughly the inverse of the time between collisions with the energy barrier. Up to our knowledge this observation has not been taken into account for the dynamical analysis of glasses.

We believe this issue has been overlooked due to other effects that also modify the relaxation. All of them play a role. Here we isolated one of the ingredients, the basin oscillation frequency. Other ingredients are the correlation between the barrier heights and basin oscillation frequency, as well as the existence of a distribution of basins (79; 81; 82; 80) .

Such effects have also been found from empirical arguments in rigidity theory of glasses (14). A simple and intuitive way to understand this is as follows. According to Dyre (13), the energy barriers are related with the molecules' mean-square displacement, $\langle u^2 \rangle$, by,

$$\Delta E = \lambda_1 k_B T \frac{a^2}{\langle u^2 \rangle}, \tag{2.15}$$

with a being the lattice parameter and λ_1 a factor of order unity. But the mean-square displacement in a basin can be written as (14; 60),

$$\langle u^2 \rangle = \frac{3T}{\langle M \rangle} \int_0^\infty \frac{\rho(\omega)}{\omega^2} d\omega \,, \tag{2.16}$$

where $\rho(\omega)$ is the density of vibrational states. Observe that the previous equation holds for the supercooled liquid close to the glass transition as long as one performs its computation in a distribution of basins and by using a cut-off for small frequencies (55). Combining the previous equations we obtain an estimate of the energy barriers,

$$\Delta E = \lambda_1 \frac{a^2 \langle M \rangle}{3 \int_0^\infty \frac{\rho(\omega)}{\omega^2} d\omega} \,. \tag{2.17}$$

Assuming the model presented in Ref. (14) for the density of states (DOS) of floppy systems, i.e.,

$$g(\omega) = (1-f) g_R(\omega) + f \delta(\omega - \omega_f) \,, \tag{2.18}$$

where, f denotes the fraction of floppy modes, while $g_R(\omega)$ denotes Debye's DOS, we obtain the following:

$$\begin{aligned} \Delta E &= \frac{\lambda_1 a^2 \langle M \rangle}{3} \left[\left(1-f\right) \frac{V \omega_D}{2\pi^2 c^3 3N} + \frac{f}{\omega_f^2} \right]^{-1} \\ &\approx \frac{\lambda_1 a^2 \langle M \rangle \omega_f^2}{3f} \left(1 - \frac{V \omega_D \omega_f^2}{2\pi^2 c^3 3N} \frac{\left(1-f\right)}{f} \right) . \end{aligned} \tag{2.19}$$

Thus, energy barriers decrease when the oscillation frequency goes to zero. Interestingly, this suggest a feedback mechanism on energy barriers and floppy modes, as has been made in the temperature-dependent constraint theory (90).

From the previous considerations, in our model we may assume a more general form of Eq. (2.14), by explicitly taking into account the correlation between V and ω_1,

$$R_{\text{crit}} = \frac{\omega_1 \omega_c T_0}{4\pi\gamma V(\omega_1)} e^{-V(\omega_1)/T_c} \,. \tag{2.20}$$

Here $V(\omega_1)$ denotes such possible correlation. Obviously, its actual form depends upon the particular potential form. However, in its more crude approximation one can extend the harmonic approximation around the closer metastable minima to estimate the height of the barrier. For this harmonic approximation, the transition barrier, which goes as $\sim \omega_1^2$, is an overestimation proportional to the separation between the barrier and the minimum, as discussed by Dyre (13). In the case of a quartic double well, the transition barrier also goes as $\sim \omega_1^2$. For the sake of the argument, let us assume in

general that the energy landscape can be written in such a way that $V(\omega_1) \sim \omega_1^{1+q}$ where $q > 0$. Then the critical cooling rate is now,

$$R_{\text{crit}} \sim \frac{1}{\omega_1^q} \exp(-\omega_1^{1+q}/T_c)\,. \tag{2.21}$$

Notice that this last expression diverges as ω_1 tends to zero. Also, in Fig. 2.6, we have plotted the characteristic relaxation time taking into account this dependence between V and ω_1 for different values of q. Notice how there always exists a temperature in which the characteristic relaxation time for broader wells is always smaller than that for narrower wells, although this can happen at a temperature much lower than T_c. In any case, from Eq. (2.21) is clear that *the long-time relaxation depends on the short-time relaxation factor* ω_1. However, its actual functional form depends upon the correlation between energy barrier and short-time oscillation frequency.

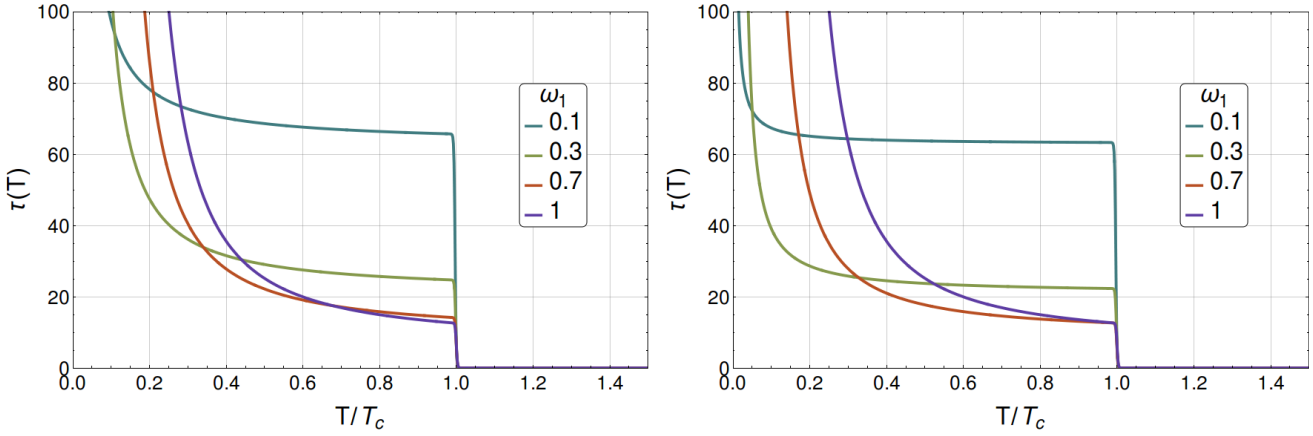

(a) (b)

Figure 2.6: Characteristic relaxation times as a function of the temperature using different oscillation frequencies of the metastable state, as obtained from Eq. (2.11) considering $V(\omega_1) \sim \omega_1^{1+q}$. In panel **(a)**, the energy barrier has $q = 0.2$ while in panel **(b)** $q = 1$. The parameters were fixed at: $N = 1000$, $\gamma = 1$, $\omega_0 = 1$, $\omega_c = 1$, $\epsilon = 1, \Omega_0 = 1$, $\Omega_1 = 2$, since we are only interested in the low frequency effect of the relaxation.

Finally, it is worthwhile mentioning that the model reproduces the experimentally observed logarithm change with the cooling rate of the glass transition temperature T_g. First we observe that T_g is the temperature for which the specific heat has a peak as a function of T. From this, one can adapt the approach used by Trachenko *et al.* (50), to put the relaxation time Eq. (2.11) at T_g into the cooling protocol $T = T(t)$, to obtain that,

$$T_g = \frac{V}{\log\left(\frac{\overline{\Delta T}}{T_0}\right) - \log\left(\frac{2\pi\gamma R}{\omega_c \omega_1}\right)}\,. \tag{2.22}$$

Here $\overline{\Delta T} = T_0^2\,(T_1 - T_2)\,/\,T_1\,T_2$ is defined as a reduced temperature range between the two temperatures

T_1 and $T_2 (< T_1)$ related by the glass transition relaxation time when the hyperbolic quench is applied. Notice, from Eq. (2.22), that $2\pi\gamma/\omega_c\omega_1$ is the Debye vibrational period, which is of the order of flow time events (50).

As mentioned already, one of the features this model lacks of is the correlation between energy barriers and vibrational modes. While in this model we have assumed no correlation and we tune the parameters independently at will, it is important to realize that this is not the case in real systems. Nevertheless, it is precisely because of the independence between vibrational modes and energy barrier in our model that we are able to understand and pinpoint the role of vibrational modes when it comes to relaxation properties. Now, let us turn to a non-linear, zero temperature model to study the relaxation properties.

2.3 Soften Hénon-Heiles Model

2.3.1 Soften Hénon-Heiles model

In the previous section we considered a simple solvable model where each of the ingredients necessary for the glass transition are uncoupled. Yet, in real glasses this is not the case and, as has been already pointed out, non-linear effects play a crucial role. Perhaps an obvious next step for the two-level model would be to consider more vibrational modes following the work of Landauer for the generalization of Kramers' transition state theory (see Ref. (91)). However, we went in a different direction by considering a non-linear model. Given the caveats when dealing with non-linear models, we decided to neglect the thermal bath. In the end, it is possible, in principle, to regard the energy landscape topology as a memory kernel function in a Langevin Equation (see Refs. (92; 36)).

Let us consider a chain consisting of 3 masses joined by non-linear springs and periodic conditions as shown in Fig. 2.7. Thus, the Hamiltonian is

$$H = \sum_{i=1}^{3} \frac{1}{2m}\vec{P}_i^2 + \frac{1}{2}k_{i+1,i}\left(\Delta Q_{i+1,i}\right)^2 + \frac{\chi}{3}\left(\Delta Q_{i+1,i}\right)^3 , \tag{2.23}$$

where $\Delta Q_{i+1,i} = Q_{i+1} - Q_i$ denotes the distance between mass i and mass $i+1$ and $k_{i+1,i}$ is the spring stiffness between masses i and $i+1$. We use χ to denote the coefficient of the non-linear force between the masses. Furthermore, let us introduce the control parameters α and β in the stiffness such that $k_{21} = k$, $k_{21}\beta = k_{13}$, and $k_{32} = \alpha k_{21}$.

As we show in detail in the Appendix B, one of the eigenvalues of dynamic matrix **D** is always zero

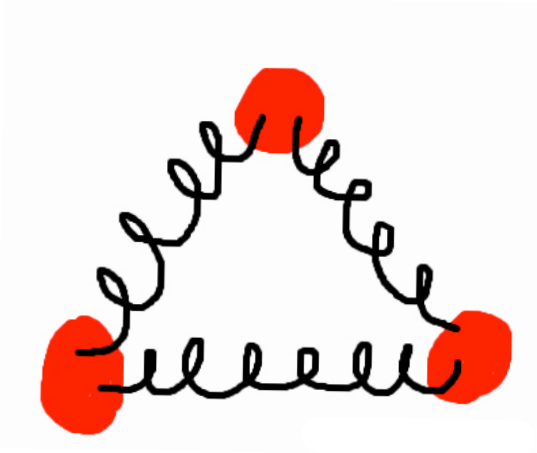

Figure 2.7: Sketch of the three masses joined by three springs.

and corresponds to the center of mass motion, while the other two depend upon δ and β. However, as was stated in the introduction, we are interested in studying the low vibrational dynamics relaxation process. In this sense, it happens that one of the eigenvalues, which we denote as ω_x^2, becomes zero only when $\delta = \beta = 0$ while the other one, denoted as ω_y^2 becomes 2. There is an additional eigenvalue we denote as ω_z^2 which is always zero and corresponds to the motion of the center of mass. Thus, here on we consider $\delta = \beta$ and without loss in generality we assume $k = 1$. Therefore, the eigenvalues become

$$\omega_x^2 = 3\beta\,, \quad \omega_y^2 = 2+\beta\,. \tag{2.24}$$

Finally, by expressing the non-linear term in terms of the normal coordinates and momenta we obtain

$$H = \frac{1}{2}\left(p_x^2 + p_y^2\right) + \frac{1}{2}\left(\omega_x^2 x^2 + \omega_y^2 y^2\right) - \frac{3\gamma}{2^{1/2}}\left(\frac{1}{3}y^3 - x^2 y\right), \tag{2.25}$$

which corresponds to two particles interacting via a Hénon-Heiles-type potential (73).

Furthermore, let us do the following rescalings:

$$\begin{aligned} y &\rightarrow \frac{2^{1/2}}{\gamma}y\,, \qquad x \rightarrow \frac{2^{1/2}}{\gamma}x\,, \\ t &\rightarrow t/3^{1/2}\,, \qquad H \rightarrow \frac{6}{\gamma^2}H\,. \end{aligned} \tag{2.26}$$

This gives the scaled Hamiltonian:

$$H = \frac{1}{2}\left(p_x^2 + p_y^2\right) + \frac{1}{6}\left((3\beta)^2 x^2 + (2+\beta)^2 y^2\right) - \left(\frac{1}{3}y^3 - x^2 y\right), \tag{2.27}$$

and the Hamilton Eqs. are

$$\begin{aligned} \dot{x}_i(t) &= p_i(t)\,, \qquad x_i = \{x, y, z\} \\ \dot{p}_x(t) &= -x(t)\left(\beta + 2y(t)\right)\,, \\ \dot{p}_y(t) &= -\frac{1}{3}\left(2+\beta\right)y(t) + \left(y(t)\right)^2 - \left(x(t)\right)^2\,. \end{aligned} \tag{2.28}$$

The resulting model is a softened *Hénon-Heiles* system, since by making $\beta \to 0$, ω_x goes to zero, resulting in a floppy mode. Thus, β is a control parameter that allows us to reduce the stiffness of the low frequency vibrational modes. This results in a lowering of two saddle points height. In the left panel of figure 2.8 we have depicted the isopotential for a fixed β and different energies. We also show the three saddle points P_1, P_2, and P_3 (red dots) and the local minimum for the potential (black dot) where the potential energy is zero. In the right panel of figure 2.8 we may appreciate how the height of the saddle points P_1 and P_2 are the same and smaller than P_3. Moreover, in figure 2.9 we have plotted the saddle points' height V vs β. When $\beta = 0$ the potential barriers located at P_1 and P_2 drop to zero, while the other barrier drops to $\simeq 0.05$ (see fig. 2.9).

In the case for which $\beta = 1$, all saddle points have the same height. This Hamiltonian corresponds to the model used by *Hénon* and *Heiles* to study the motion of a star in a galaxy with cylindrical symmetry (69). For a certain choice of parameters it has been proven to be an integrable problem (70), but it is not in general. Moreover, numerical results suggest that when the energy of the system is $E < 1/12$, the system is non-chaotic and non-ergodic, yet above this energy the region with chaotic behavior in phase space increases with the energy up until $E = 1/6$ where the whole phase space is chaotic and, which is also, saddle point's height (74; 73).

In this way, it seems that as the energy increases the dynamics become chaotic and ergodicity is established. However, in this work we show that this is not always the case for the softened model. Actually, as the energy increases, there are certain islets in the phase space for which quasi-periodicity is established. This is done in the following section.

2.3.2 Relaxation properties of the softened Hénon-Heiles model

In this section we present the results obtained from solving numerically the Hamiltonian Eqs. (Eqs. (2.28)). We first fix β and the energy, ΔE, above the lower saddle points height (see fig. 2.8), then we took $N = 16000$ uniformly random chosen initial conditions, i.e., linear moment orientation and

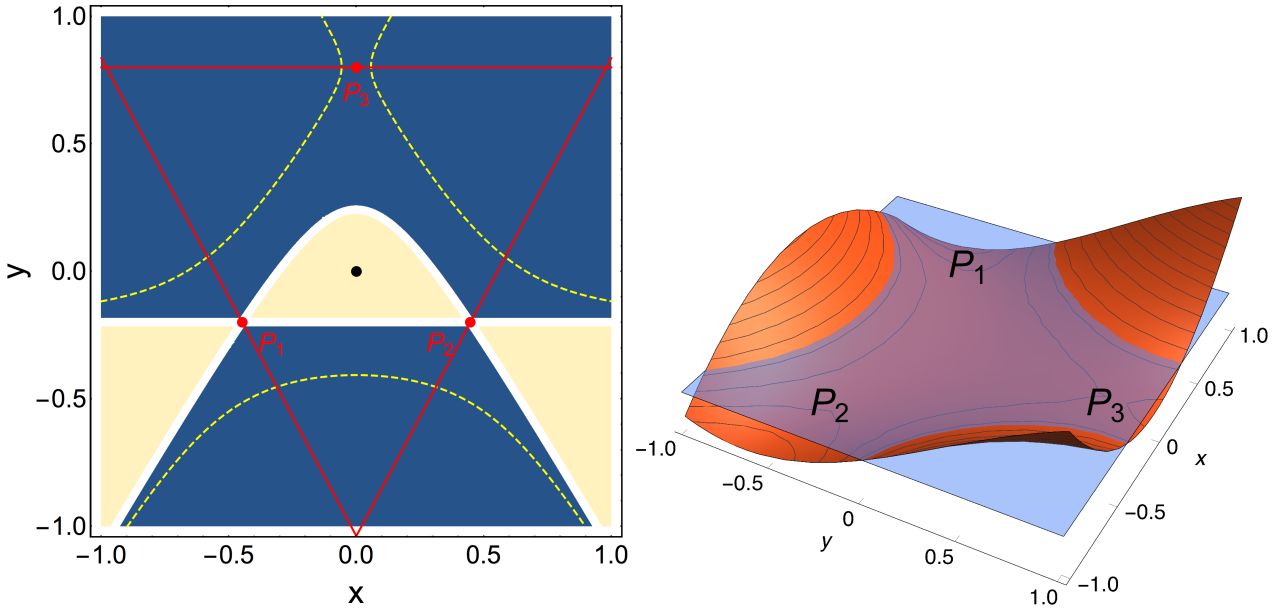

Figure 2.8: Energy landscape showing an isopotential with $\beta = 0.4$. **left panel** The dashed line correspond to the isopotential with energy, $\Delta E = 0.07$, above the lower saddle points height (yellow) while the inner soften triangle corresponds to $\Delta E = 0$. Each line of the red triangle goes through a saddle point and has the direction of the eigenvector corresponding to the positive eigenvalue of the Hessian matrix in the corresponding saddle point. **right panel** Here we show a 3D plot of the potential. The transversal plane corresponds to $\Delta E = 0.07$.

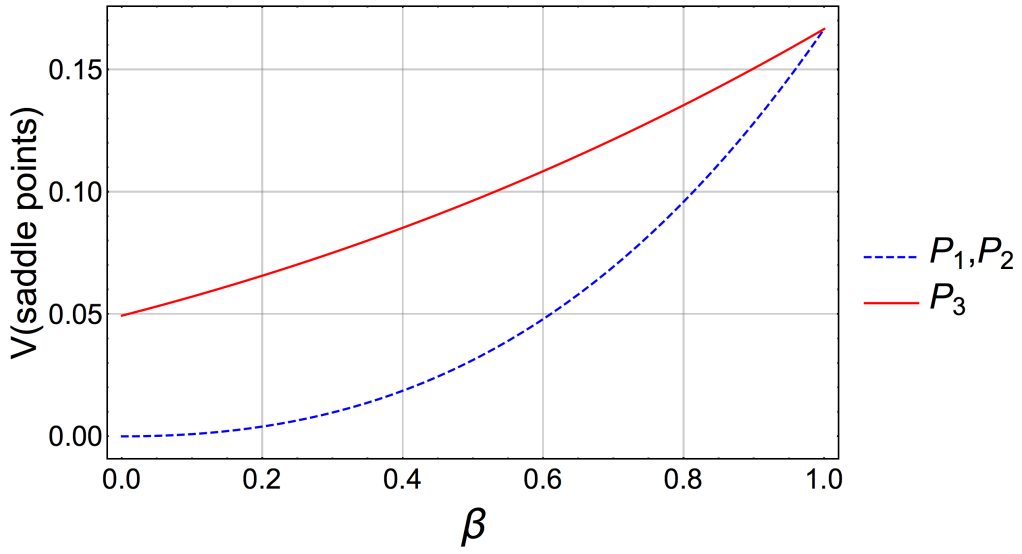

Figure 2.9: Plot of the saddle point heights as a function of β. The blue dashed curve corresponds to the saddle point height at P_1 and P_2, while the red continuous curve corresponds to the saddle point height at P_3 (see fig. 2.8)

position, given the fixed energy. Then we let them evolve and we study the distribution of their escape time, i.e., the time taken to escape the well through any of the exit channels denoted as P_1, P_2 and P_3 (see figure 2.8). We do this for different values of the parameters β and ΔE, which we present in figure 2.10. The blue line in figure 2.10 corresponds to the energy difference between the upper saddle point and the lower saddle points, i.e., for a given fixed β when ΔE is under the blue curve there are two exit channels, namely, P_1 and P_2; while when ΔE is above the blue curve, there are three exit channels.

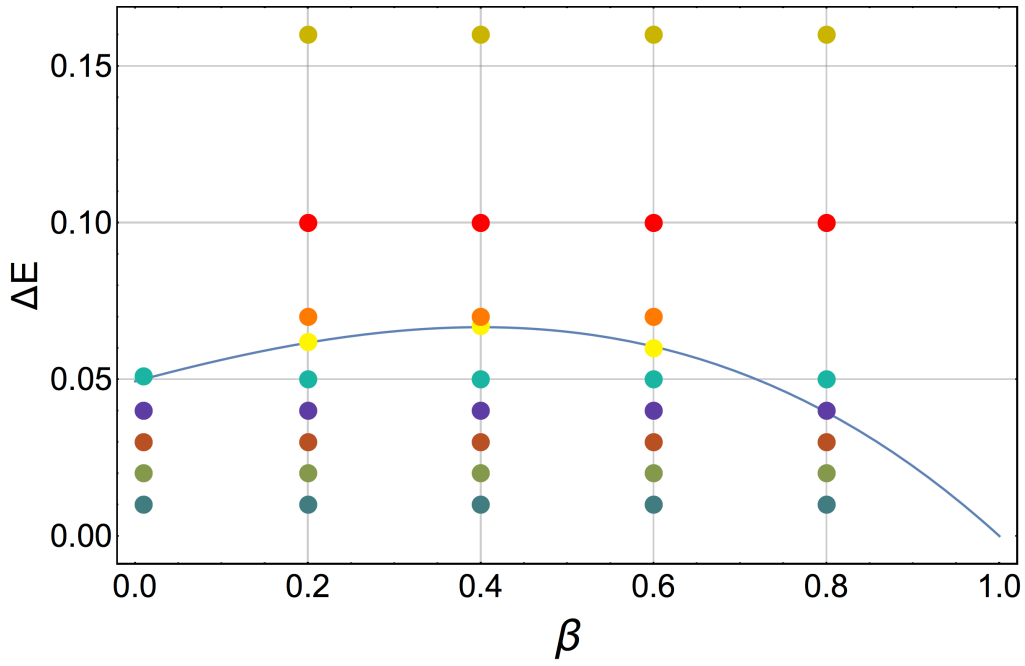

Figure 2.10: Sets of parameters $(\beta, \Delta E)$ used in our simulations to study relaxation. Points of the same color have the same energy ΔE above the lowest saddle points. The blue curve corresponds to the energy difference between the high and low saddle points, i.e., for ΔE under the blue curve there are two exit channels, namely, P_1 and P_2 and for ΔE above the blue curve, there are three exit channels.

In figures 2.11, 2.12, 2.13 and 2.14 we present the population $N(t)$ inside the well as a function of time in Linear-Log and Log-Log plots. We also present the potential contour corresponding to each of the values for ΔE for a fixed β. Rather than using legends in each of the plots, we used instead the same colors, i.e., the red curves in the potential contour plot and in the *N(t) vs t* correspond to the same value of ΔE which we show in figure 2.10. The first thing one may notice is that, in general, the escape flow at a given time follows an exponential decay. However, there are some values of β and ΔE for which the escape flow at a given time has a crossover into a second exponential decay and *sticky states* appear, but we will come back to this later.

Notice that for small t it seems that $N(t) \sim \exp(-\alpha t)$. In figure 2.15 we present the values of α as

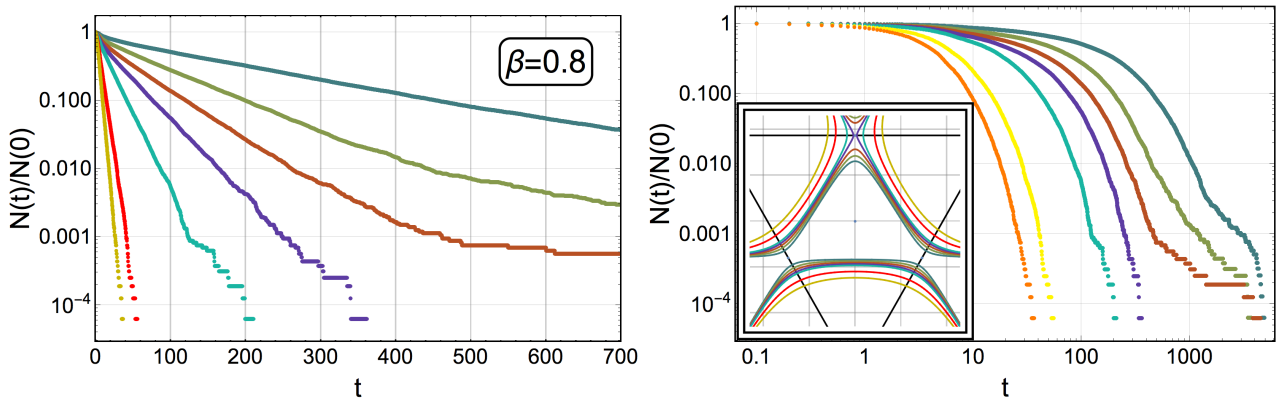

Figure 2.11: For $\beta = 0.8$: (**left panel**) The population in the potential at time t in a Log-Linear plot, for different energies as indicated in the color code of figure 2.10 . (**right panel**) The population in the potential at time t in Log-Log. (**Inset**) The isopotential for different values of ΔE(see fig. 2.10).

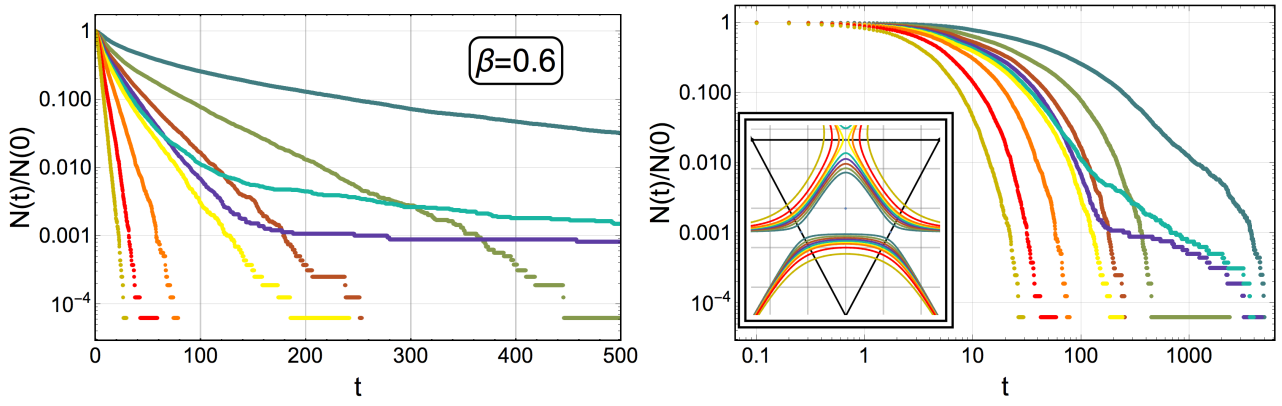

Figure 2.12: For $\beta = 0.6$: (**left panel**) The population in the potential at time t in Log-Linear, for different energies as indicated in the color code of figure 2.10 . (**right panel**) The population in the potential at time t in Log-Log. (**Inset**) The isopotential for different values of ΔE(see fig. 2.10).

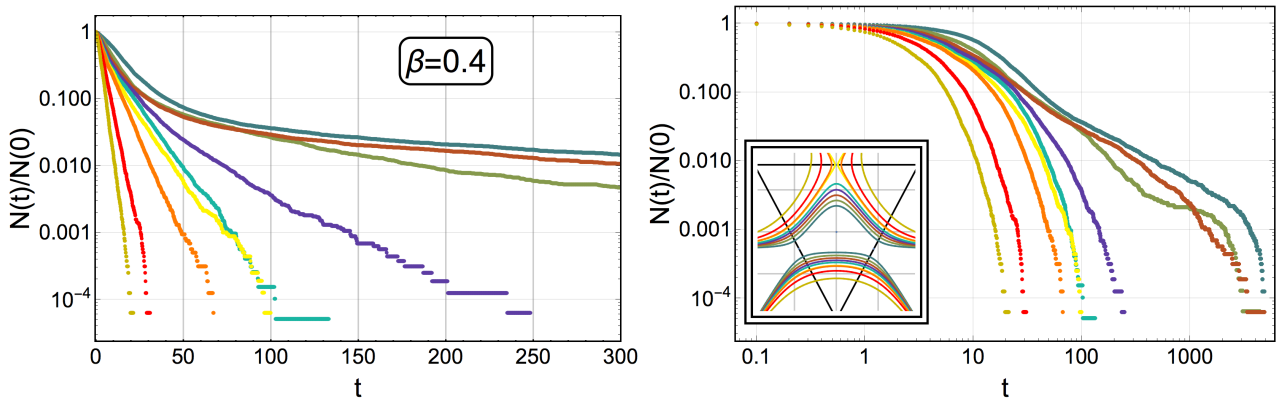

Figure 2.13: For $\beta = 0.4$: (**left panel**) The population in the potential at time t in Log-Linear, for different energies as indicated in the color code of figure 2.10 . (**right panel**) The population in the potential at time t in Log-Log. (**Inset**) The isopotential for different values of ΔE(see fig. 2.10).

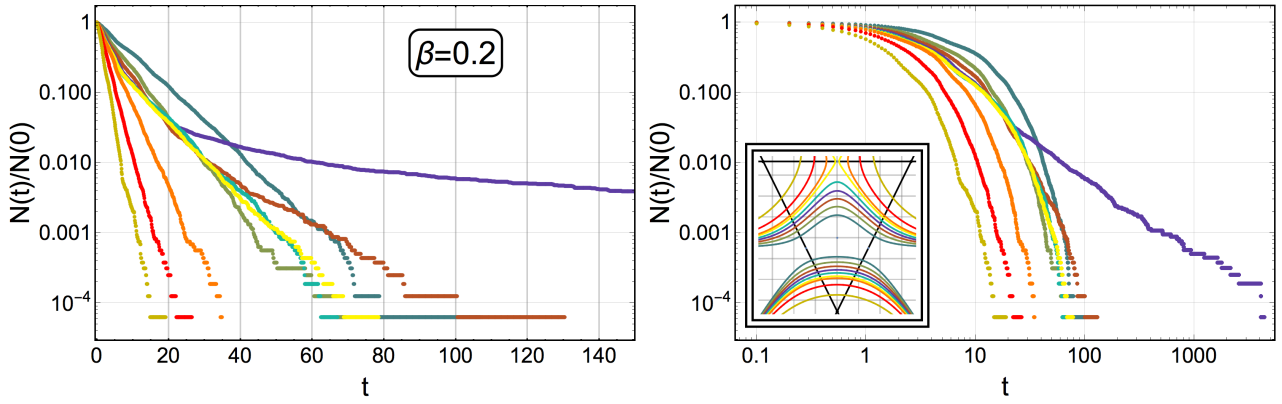

Figure 2.14: For $\beta = 0.2$: (**left panel**) The population in the potential at time t in Log-Linear, for different energies as indicated in the code of figure 2.10 . (**right panel**) The population in the potential at time t in Log-Log. (**Inset**) The isopotential for different values of ΔE (see fig. 2.10).

a function of β and ΔE, obtained by fitting the curves in figures 2.11, 2.12, 2.13 and 2.14 in the short-time regime (see Appendix B). The dashed line divides the scenario in which there are only two exit channels (which correspond to the two lower saddle points) from the scenario where there are three exit channels (see fig. 2.8).

To understand this exponential decay behavior for the unsoften Hénon-Heiles model ($\beta = 1$), first Bauer and Bertsch and then Zhao *et al.* (74; 76) used rather simple arguments. They considered that all initial conditions contained in the energy landscape well would flow out and assumed that the population change rate equals the flux with momentum orientation between $-\pi/2$ and $\pi/2$ relative to the normals of the exit channels line. Hence

$$\frac{dN(t)}{dt} = -N(t)\rho \int_{-\pi/2}^{\pi/2} d\phi \int_{r_0}^{r_1} dl\,|\vec{v}(x,y)|\cos\phi\,, \tag{2.29}$$

where $\rho = 1/2\pi S(\Delta E)$ is the distribution of the variables (x, y, θ), $\vec{v}(x,y)$ is the velocity field, dl goes over the channels' entrance and $S(\Delta E)$ is the area of the well. The integral goes over the opened exit channel lines and, the points r_0 and r_1 correspond to the classical return points at these opened exit channel lines. In the case where $\beta = 1$, all exit channels are identical. Then, integrating over the exit channel P_3 and multiplying by 3 yields

$$\frac{dN(t)}{dt} = -\frac{\sqrt{3}\Delta E}{S(\Delta E)} N(t)\,. \tag{2.30}$$

Hence, $N(t) \sim e^{-\alpha t}$, with $\alpha = \sqrt{3}\Delta E/S(\Delta E)$.

In the softened Hénon-Heiles model, the exit channels P_1 and P_2 are identical and different from P_3. Following this same idea, we determined $\alpha(\beta, \Delta E)$ by estimating the escaping flux numerically from Eq. (2.29), but evaluated for the open channels for a given energy where

$$\begin{aligned} |v(x,y)| &= \left[2\left(\Delta E + \frac{1}{12}\beta^2(1+\beta)\right.\right. \\ &- \left.\left.\frac{1}{6}\left(3\beta x^2 + \left(2+\beta\right)y^2\right) + \left(\frac{1}{3}y^3 - x^2 y\right)\right)\right]^{1/2}. \end{aligned} \tag{2.31}$$

The first two terms on the right hand side of Eq. (2.31) are simply the energy above the lower saddle points and the lower saddle points energy height.The third term in the right hand side of Eq. (2.31) is the softened Hénon-Heiles potential. The classical returning points as well as the area of the wells, $S(\Delta E)$, were also determined numerically for different values of ΔE.

These results can be compared with the actual fitting of α obtained from the numerical results of $\log N(t)$ for small t, as obtained in figures 2.11, 2.12, 2.13 and 2.14. In figure 2.16 we compare both

methods, namely, the blue points correspond to the fitting methods while the orange curves correspond to the numerical flux estimation method. The discontinuity around $\Delta E \approx 0.05$ corresponds to the threshold energy where the exit channel P_3 is available. We should clarify that the orange curves were obtained by interpolating numerical results, i.e., no analytical Eq. was obtained. One may appreciate how this heuristic approach works quite well for small ΔE, not so much for when the flow may come out through the upper channel, i.e., P_3. This has to do with the fact that in this regime, not all initial conditions in configurational space flow out of the basin, as we will show later.

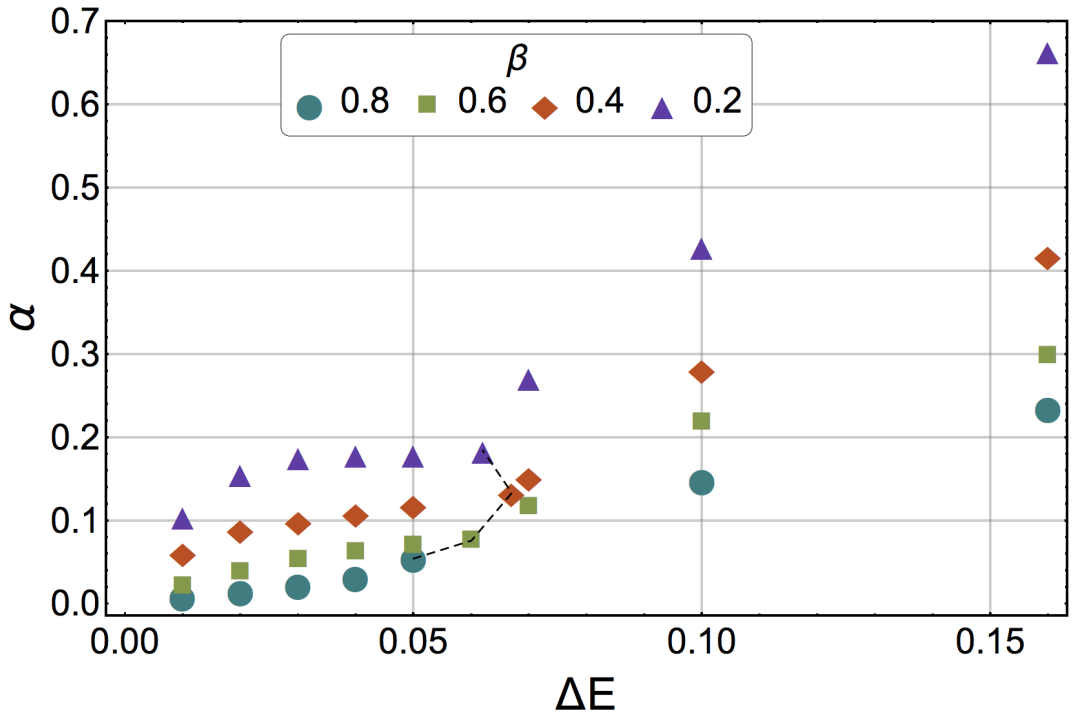

Figure 2.15: $\alpha(\beta, \Delta E)$ obtained numerically by solving the Hamilton Eqs. (2.28). The dashed line separates the region where the exit channel corresponding to the saddle point P_3 is forbidden (left) and the region where it is accessible (right).

From figures 2.15 and 2.16 is clear that the relaxation time $1/\alpha$ decreases as the stiffness of the model is reduced, since in general α grows as β is reduced for a fixed energy. This is explained in general by two effects. The first is a reduction of the energy barrier heights along the softened normal modes (see fig. 2.9), and the second is a widening of the opening channels.

2.3.3 Dynamical heterogeneity and sticky states

To have a better grip and to qualitatively differentiate which conditions flow out following an exponential decay from the region which flows out following a power law, we fixed $\beta = 0.4$ and $\Delta E = 0.02$

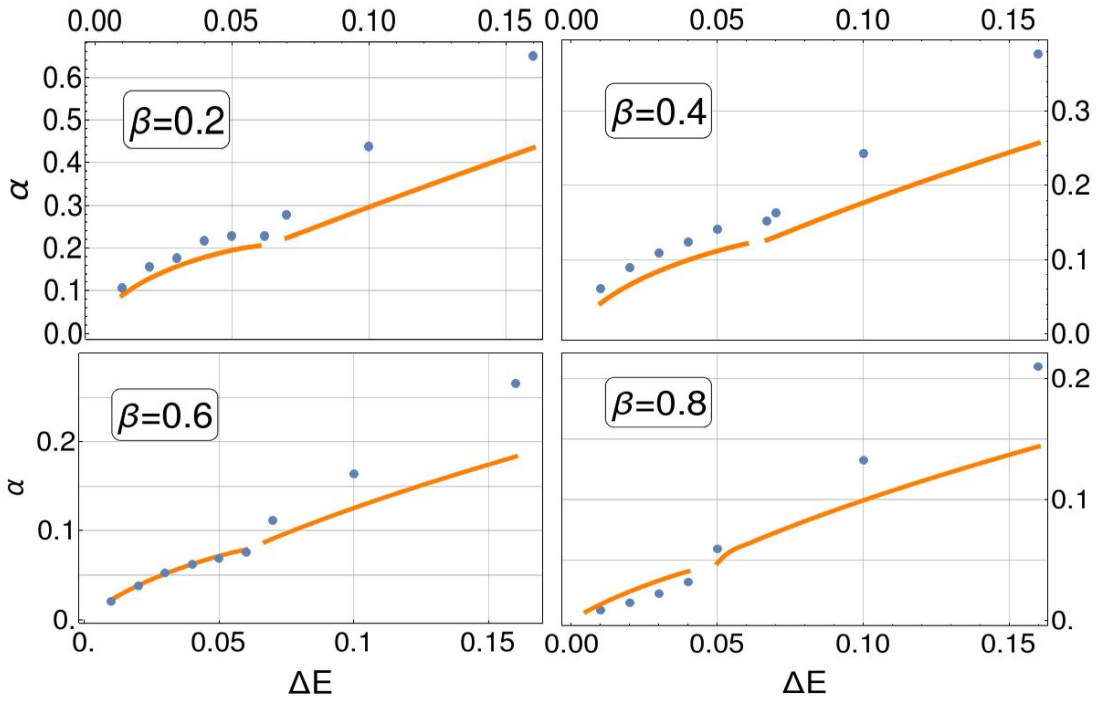

Figure 2.16: $\alpha(\beta,\Delta E)$ obtained from numerically solving the Hamilton Eqs. (2.28) (blue dots) and by considering the initial conditions escape flux (see Eq. (2.29)) (yellow lines). The regime change around $\Delta E \approx 0.05$ corresponds to the threshold where the exit channel P_3 is available.

and solved numerically the Hamilton Eqs. (2.28) for $N \simeq 5\cdot 10^4$ different uniformly randomly chosen initial conditions, i.e., (x,y,θ). In the left panel of figure 2.17 we have plotted $\sim 50\%$ of the studied initial positions which flow out first , i.e., we plot the configurational space region that corresponds to the exponential decay regime of $N(t)$, and we have colored each point according to their initial momentum orientation. We also did this for the initial conditions which flow out the slowest, corresponding to the power law regime of $N(t)$, and we show this in the right panel of figure 2.17. There are several features we can extract from this. First, notice that the conditions that flow out first are those with an initial momentum oriented towards the exits. Yet, there are some initial positions which define two regions, namely, region I and region II (see upper panel in figure 2.17), which does not flow out during the exponential decay regime no matter what their initial moment orientation is. This is further verified in the right panel of figure 2.17 from which we may qualitatively appreciate a density gradient in the y direction for $y>0$ and in the $-y$ direction for $y<0$.

Also notice that the bulk of the initial positions which flow out slowly is concentrated in a vicinity of $x \simeq 0$. However, there is clearly an overlap in this vicinity with the initial positions that exit quite fast. For this reason, in figure 2.18 we have plotted in the left panel the initial condition coordinate

x and the initial momentum orientation θ with respect to the horizontal line for 50% for the initial conditions that flows out first, while in the right panel of figure 2.18 we plotted the initial condition coordinate y and the initial moment orientation θ of the slowest flowing initial conditions. In both plots the color is a function of the exit time, i.e., red corresponds to the smallest exiting time while navy blue corresponds to the largest exiting time. Notice that from the left panel of figure 2.18 one may appreciate fairly well that the configurational space region that flows out first is the one next to the left (right) exit channel and have initial moment orientation between 2.3 and $3\pi/2$ (4.5 and $2\pi+1$), then the initial conditions region that follows has an initial momentum orientation contained in these intervals but with smaller absolute value of the initial position coordinate x, in other words, the initial moment orientation still corresponds to that directed towards one of the exits channels. Now, the initial conditions region that follows has an initial moment orientation in the vicinity of $\pi/2$ and is distributed around $x \pm 0.3$. This means that this initial conditions region collides with the potential barrier before being able to flow out.

Now, from the right panel in figure 2.18 we may appreciate that the initial conditions region which takes the longest to flow out is distributed all over the classically permitted interval in the y axis but with either $\pi/2$ or $3\pi/2$ as the value of the initial moment orientation. All this suggests that the region that takes the longest to flow out corresponds to oscillating trajectories in the y direction and in a quasiperiodic manner with $x(t) \simeq 0$, i.e., sticky orbits appear.

Going one step further, in figure 2.19 we show a *Poincaré* section for one of the initial conditions which takes a long time to flow out, obtained in the case of $\beta = 0.4$ and $\Delta E = 0.02$. Clearly, this type of section corresponds to a quasi-periodic trajectory. Eventually, the small deviations amplify and the trajectory escapes the well.

2.3.4 Application to glasses

The previous results can be put in many ways into the context of glasses. First, the softening of the energy barriers due to flexible modes observed in the previous model can be generalized for glasses. To this end, consider N atoms described by a pairwise potential, say, $V(\{x_i\})$ where $\{x_i\}$ is the set of generalized normal coordinates expanded around a meta-stable state with $i = 1, ..., 3N$ and let us assume that $V(\{0\}) = 0$, hence

$$V(\{x_i\}) = \frac{1}{2}\sum_{i=1}^{3N} \omega_i^2 x_i^2 + V_{NL}(\{x_i\})\,. \tag{2.32}$$

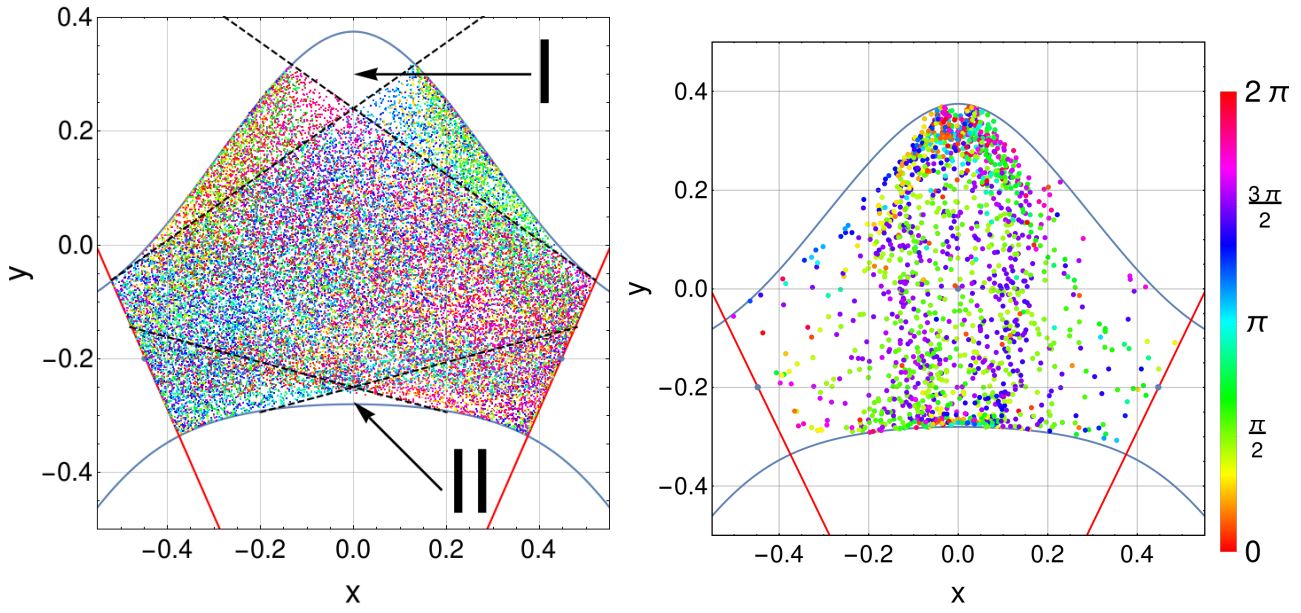

Figure 2.17: Escape decay regime as a function of the initial position for $\beta = 0.4$ and $\Delta E = 0.02$. The coloring corresponds to the initial momentum orientation with respect to the horizontal (see legend). (**left panel**) Particles which escape under the exponential decay regime. The black dashed lines are an eye-guidelines to indicate the cone-like regions of particles with initial momentum orientation directed towards one of the exits, and also indicate the regions I and II where particles there take longer to escape no matter what their initial moment orientation is. (**right panel**) Particles which escape under the power law regime as a function of the initial positions. The isopotential curve is indicated in blue while the exits of the potential basin is indicated by lines.

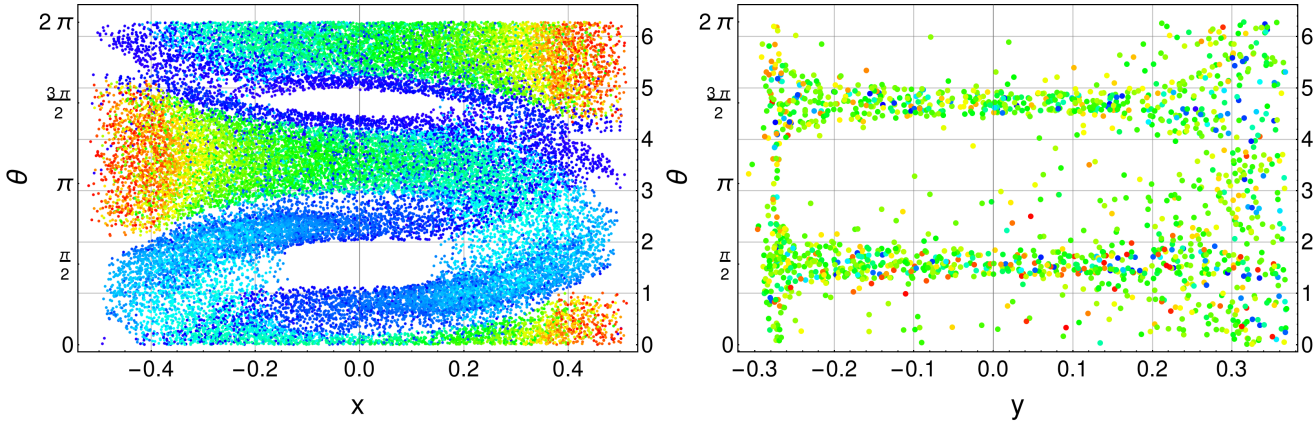

Figure 2.18: Decay regime as a function of the initial position x and initial moment orientation θ in the case of $\beta = 0.4$ and $\Delta E = 0.02$. (**left panel**) Particles which escape under the exponential decay regime. (**right panel**) Particles which escape under the power law regime. The coloring corresponds to the time taken to escape, such that red is short exit times and navy blue is for large exit times (see legend in Fig. 2.17).

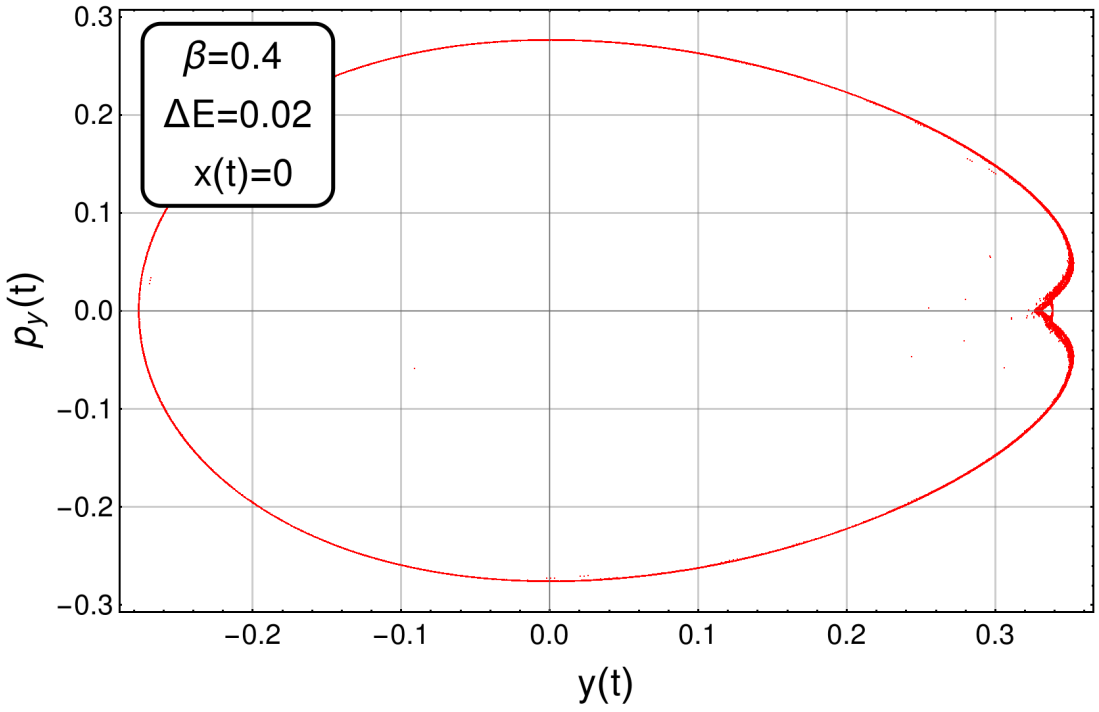

Figure 2.19: Poincaré map for $\beta = 0.2, \Delta E = 0.04$ and some initial condition for which the particle takes a long time to exit the basin, corresponding to a sticky state.

Here $V_{NL}(\{x_i\})$ denotes the non-linear part of the potential. In general, floppy modes occur by lowering interactions, usually by more than an order of magnitude. In chalcogenide glasses, stiffness can be increased by adding cross-linking modifiers like Ge which add stronger interactions (18). Floppy modes can also be produced by reducing sizes of some atoms when using Lennard-Jones potentials (23; 60). Thus, if we were to loosen the stiffness of a fraction f of the normal modes, i.e., decrease ω_j with $j = 1, ..., 3Nf$, in general, one would expect a variation in the non-linear part of the potential in the sense that it will ultimately depend on the kind of potential that describes a given supercooled liquid and the physical way in which one modifies the stiffness of the normal modes. Since the details depend upon the particular potential, here we adopt a worst case scenario, i.e., we may assume that the non-linear part of the potential is kept fixed when the stiffness is loosen. Therefore, we denote the potential with a fraction f of floppy modes as $V_F(\{x_i\})$, such that

$$V_F(\{x_i\}) = \frac{1}{2}\sum_{i=1}^{3N(1-f)} \omega_i^2 x_i^2 + \frac{1}{2}\sum_{j=1}^{3Nf} \left(\lambda_j \omega_j^2 x_j^2 + V_{NL}(\{x_j\})\right). \tag{2.33}$$

where we have denoted the frequency of floppy normal modes as $\sqrt{\lambda_j}\omega_j$ and $0 < \lambda_j < 1$. Then, notice that

$$V_F(\{x_i\}) = V(\{x_i\}) - \frac{1}{2}\sum_{j=1}^{3Nf}\left(1-\lambda_j\right)\omega_j^2 x_j^2 \,. \tag{2.34}$$

which implies that

$$V_F(\{x_i\}) \leq V(\{x_i\}) \,, \tag{2.35}$$

since the second term in Eq. (2.34) is always positive. Thus, in general the energy barrier height decreases in the direction of floppy modes in comparison to rigid modes, and one expects relaxation in the direction of floppy modes. It is clear that this general behavior is what lies in our soft Hénon-Heiles model, which is the extreme case of two degrees of freedom (fixing the center of mass). Yet even this two degrees of freedom model can be used to understand some features of glass relaxation.

For example, recently there has been a lot of theoretical interest in the β-relaxation (not to be mistaken with the β parameter in our model) or Johari-Goldstein relaxation for glass-forming materials, since it has been revealed its connection with the glass transition (93). This phenomenon becomes visible below the melting temperature. Yet, the origin of this has generated controversy (94; 24; 95), but it seems quite likely that this relaxation is concerned with the small-amplitude rotational jump motion of molecules (96–98). In Ref. (24), Tanaka proposed a two-order parameter phenomenological model for rigidity and glass relaxation which is based on local fluctuations of reorientational jumps, identified with the β-relaxation. These fluctuations are observed within rigid metastable islands. The relaxation of these rigid islands is also known as the α-relaxation process (not to be mistaken with the α parameter in our model), which slows down when reaching the glass transition temperature upon cooling. Hence why the β-relaxation becomes visible below the melting temperature where the α-relaxation time starts to pick up, and molecules start being caged. The origin of the α-relaxation has also generated controversy in glass-forming liquids and it seems to be one of the key ingredients of the glass transition. Both, α and β relaxations seems to be important in the glass transition, since the first one is associated with a long range ordering while the second one with a short range ordering, and the competition between these two creates an energetic frustration causing the glass transition. Now, in most glasses, there happens to be an overlap between the α-relaxation and the β-relaxation. Much dissent has caused the fact that it is not clear whether this overlap is for the most part the α-relaxation mode excess wing or the so-called slow-β-relaxation mode. Here lies the main purpose of Tanaka's two-order parameter mode (24).

In this sense, our model may be applied to the Tanaka's rigidity relaxation model. Within this model, there are local fluctuations with reorientational jumps (24). Consider three-dimensional asymmetrical molecules caged by a rigid surrounding metastable island. For each molecule, the rotational state can be described by two Euler angles coordinates, the polar angle η and the azimuthal angle ϕ. We associate the coordinates x and y of our softened Hénon-Heiles model to these angles. Due to the asymmetry of the molecule, the interactions with the rigid cage will lead to different elastic constants for each Euler angle, and thus Eq. (2.25) can be used as a model. A reorientational jump will be associated with an exit of the model's central basin. Since in our model any given initial condition exits the basin once the momentum orientation θ points outwards through any of the available exit channels, then the characteristic β-relaxation time τ is proportional to the mean exit time in our model. In the case where the flux method applies, the mean time for a reorientational jump is simply the inverse of α, thus $\tau \sim 1/\alpha$. The exponential law decay is in agreement with the experimental observed Arrhenius law for relaxation (24) . Yet our results implies that the non-linear part can lead to a complex dynamics since for some states and glasses, the relaxation can be slowed down in a power law fashion for an important number of cages, where the molecules stick for certain orientations. It is also known that this kind of power law also occurs in glasses (24).The regime where this happens for the softened model and for real glasses is an open problem. Notice that when many rotational traps are present with different relaxation times, stretched exponential laws with special magic exponents are obtained (38; 99).

2.4 Discussion

The two-level model shows an Arrhenius behavior. But there is a way to obtain the fragile time relaxation. Notice from Eq. (2.11) that the relaxation time is simply the inverse of the sums of all the transition probabilities per time unit. In fact, this is the way one computes the transition time when performing a Kinetic Monte Carlo simulation (100; 61). Therefore, let us consider a large number of energy barriers and distributed by a probability density function $P(E)$ such that the relaxation time τ may be written as,

$$\tau = \left(\int \Gamma(E) P(E) dE \right)^{-1}, \tag{2.36}$$

while $\Gamma(E) \sim \exp(-\beta E)$. Notice that in the cases where all energy barriers have the same height E_0, then $P(E) = \delta(E - E_0)$ and we recover Arrhenius' Law. Now, since we are merely interested in this

derivation as a proof of concept, let us assume a Gaussian distribution such that the random variables E are distributed according to $N(E_0, \sigma^2)$. Then, it is straightforward showing that,

$$\tau \sim \exp\left(\beta E_0 - \frac{\sigma^2\beta^2}{2}\right)\left(1 + \mathbf{sgn}\left(\frac{E_0 - \sigma^2\beta}{\sqrt{2}\sigma}\right)\mathbf{Erf}\left(\frac{E_0 - \sigma^2\beta}{\sqrt{2}\sigma}\right)\right)^{-1}, \tag{2.37}$$

with the sign function defined as

$$\mathbf{sgn}(y) = \begin{cases} 1, & y \geq 1 \\ -1, & y < 0 \end{cases}. \tag{2.38}$$

Now, let us define $x = T_g/T$, where T_g is the glass transition temperature. Furthermore, let us define $u = E_0/T_g$ and $\Omega = \sigma/T_g$. Then, Eq. (2.37) becomes

$$\tau \sim \exp\left(x\left(u - \frac{\Omega^2 x}{2} - \frac{1}{x}\ln\left[1 + \mathbf{sgn}\left(\frac{1 - \frac{\Omega^2 x}{u}}{\sqrt{2}\Omega/u}\right)\mathbf{Erf}\left(\frac{1 - \frac{\Omega^2 x}{u}}{\sqrt{2}\Omega/u}\right)\right]\right)\right). \tag{2.39}$$

Notice that the exponent of Eq. (2.39) is reminiscent of a free energy. Now, we are interested in the region where $x \lesssim 1$, which is close to the glass transition. Now, let us also assume that $\frac{\Omega^2 x}{u} \gtrsim 1$, which reduces to $\sigma^2 \gtrsim E_0 T_g$. In that case, it is a feasible task to show that

$$\ln\tau \sim Ax - Bx^2 + Cx^3, \tag{2.40}$$

where

$$\begin{cases} A = u\left(1 - \frac{1}{\sqrt{\pi}}\right) - \frac{2}{\pi}\Omega + \frac{u^2}{\sqrt{2\pi}\Omega} \\ B = \frac{\Omega^2}{2}\left(1 - \frac{1}{\sqrt{\pi}}\right) + \frac{u\Omega}{\sqrt{2\pi}} \\ C = \frac{\Omega^3}{3\sqrt{2\pi}} \end{cases}. \tag{2.41}$$

Notice that $B > 0$, $C > 0$ for all positive values of u and Ω while $A > 0$ in the region of interested. In Fig. 2.20 we have plotted Eq. (2.40) together with Arrhenius' Law in an Angell-type plot.

2.5 Conclusions

Up to this point we have shown two models to gain insight into how relaxation occurs, as well as, how complex it is. To summarize:

- We developed a simple solvable two-level model which has a first order phase transition to a crystal and a dynamical phase transition to a glass when cooled fast enough.

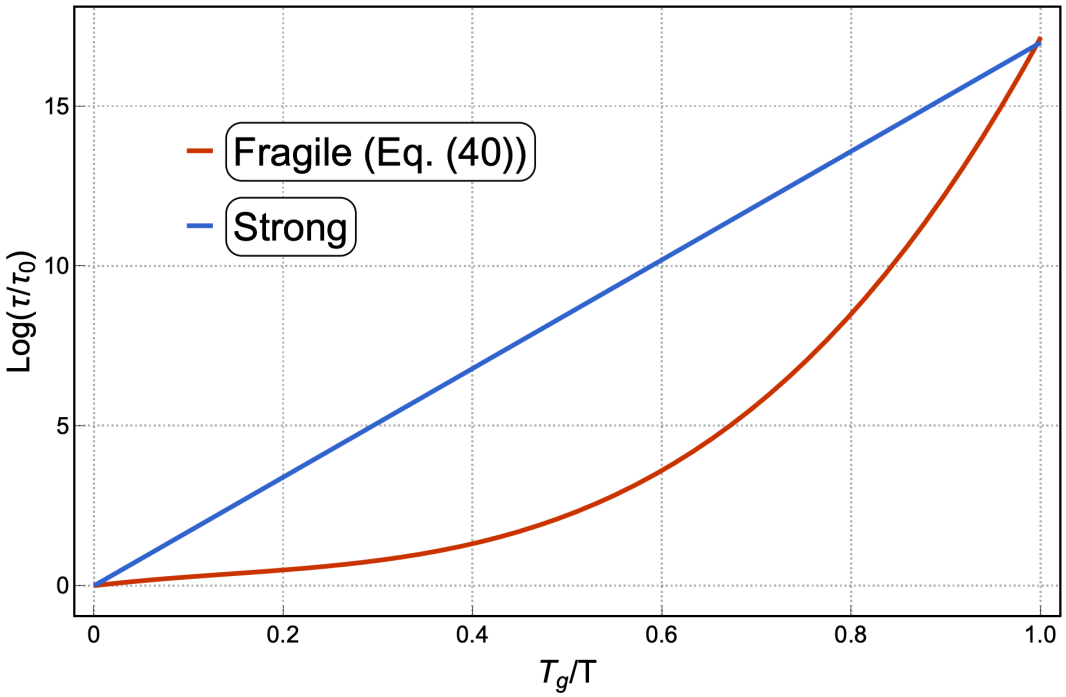

Figure 2.20: Plot of relaxation time *vs* $x = T_g/T$ for a strong and fragile glass, modeled by the Arrhenius' Law and Eq. (2.40), respectively. This was obtained by assuming a Gaussian distribution of energy barriers. The dispersion consideration allows the fragile behavior. We fixed $\Omega \gtrsim \sqrt{u}$.

- We solved this model analytically and obtained an equation which relates the relaxation time with the vibrational modes.
- We showed that as the vibrational mode frequencies tend to zero, the system requires more time to probe the energy landscape, in this sense, the relaxation time has two contribution, namely, the exponential weight that takes into account the energy barrier and the vibrational modes which corresponds to a characteristic probing time of the minimum where the system is found.
- We considered a non-linear, zero temperature model and studied the relaxation as the energy barriers decrease.
- We showed that this model has dynamical heterogeneity, leading to different relaxation time scales.
- In this sense, when there's coupling between the vibrational modes, the relaxation time decreases.

In addition to the previous points, we highlight that, *i*), the dispersion of energy barriers is related with the fragile behavior, *ii*), the dispersion of energy barriers is also related with the vibrational modes and, *iii*), these vibrational modes contribute to the vibrational entropy. The latter may or may not play a crucial role in the topology of the energy landscape as we will see in what follows.

Chapter 3

On the rigidity properties of glass forming systems

3.1 A dynamical approach to rigidity

Understanding how rigidity happens, i.e., how a given system goes from being rigid to be able to flow and *vice versa* is a very important problem which impacts fields ranging from solid state, condensed matter as well as biology (101). The fact that glasses have a dynamical transition makes them the perfect system to study rigidity, but this does not mean it is an easy task at all. In the journey towards an understanding of the rigidity transition, it is accurate to say that a milestone was set with Phillips and Thorpe's constraint theory of rigidity. This has provided the baseline to understand rigidity and how this is related with the network topology (18; 52). From there on, a lot of research has been done. This research allowed the incorporation of thermodynamics in rigidity theory (58; 53; 54; 102; 103; 55; 104) as well as the Boson peak (105–107). Molecular dynamics simulations in realistic systems have been of invaluable help regarding this point (see for instance (108)). Stochastic models gave similar results (1; 3). Boolchand and coworkers have made different studies concerning rigidity in melts and glass aging using optical, mechanical and thermodynamical properties (109; 110).

Basically, our understanding of rigidity relies on Philips and Thorpe's iconic works. Rigidity is also very much related with usual thermodynamic phase transitions as any transition involves the development of a generalized rigidity to keep phase order against thermal fluctuations (111). However, our understanding of liquid to crystal phase transition relies on the trade-off between internal energy and entropy, where below a certain temperature the internal energy has a dominating role over

the free energy. This then justifies the decrease in configurational entropy when crystallization happens and somehow rigidity is embedded in this process to the point in which we generally assume that the rigidity transition is necessarily accompanied by a thermodynamical phase transition. Yet, in glasses this is not that case, as well as in 2D systems. Hence, the rigidity transition is not well understood. Furthermore, since the glass transition is a dynamical transition and glasses fail to fit this idea of liquid-to-solid transition, then one may ponder that the origin of rigidity comes from a dynamical transition rather than a thermodynamical one. In addition, this would have great impact on biological processes, which are generally assumed as out-of-equilibrium processes, and present liquid-solid phase transitions (112; 113).

The way in which rigidity is conventionally measured is by using the relative concentration as a coordination number proxy(18). Although this is a clear defined protocol in a solid, in a liquid it is more difficult to have such a picture, given the non-periodicity and, hence, the inability to use mean field approaches in many cases. As a central idea of this thesis, we propose using the tools from viscoelastic theory, in particular, the visco-elastic response in space and time. In fact, the lack of elastic behavior against shear stress turns out to be the main defining feature of a Newtonian fluid. However, elasticity of liquids depends upon the time and spatial scales in which the system is probed or perturbed. Thus, viscoelasticity will contain very valuable information concerning the rigidity of dense liquids close to a glass transition.

As previously mentioned, the main feature that defines a rigid system is the resistance to shear-stress. Rigidity is related to the propagation of transversal waves. Thus, a natural starting point is to look at wave propagation, which involves a frequency ω and a wavevector $\boldsymbol{k}$. Therefore, rigidity of liquids involves time and space density-density and velocity-velocity fluctuations, which are well described by the dynamical structure factor. Here we are concerned with the transversal part of the dynamical structure factor, defined as (114),

$$S(k,\omega) = \int_0^\infty dt e^{-\imath\omega t} C_T(k,t)\,. \tag{3.1}$$

where $C_T(k,t)$ is the transversal current density-density correlation function,

$$C_T(k,t) = \langle J_T^*(\boldsymbol{k},t) J_T(\boldsymbol{k},0)\rangle\,, \tag{3.2}$$

and the brackets $\langle ...\rangle$ represent an ensemble average as well as an average over the different directions of $\boldsymbol{k}$. $J_T(\boldsymbol{k},t)$ is the transversal density current:

$$J_T(\boldsymbol{k},t) = \frac{1}{\sqrt{2N}k}\sum_{i=1}^{N} \boldsymbol{k}\times\boldsymbol{v}_i(t)\exp\left(\imath\boldsymbol{k}\cdot\boldsymbol{r}_i(t)\right)\,. \tag{3.3}$$

Here, $\boldsymbol{v}_i(t)$ and $\boldsymbol{r}_i(t)$ are the velocity and position of the i^{th} particle of a given system at time t. The $1/\sqrt{2}$ factor takes into account the two transverse currents in three-dimensional systems. This factor is replaced by one in two dimensions.

The resulting correlation functions can also be used to find the complex susceptibility $\xi(k,z)$ (where $z=\omega+i\epsilon$) when an external field probe $F(t)$ is appplied to the system. It can be proved that the susceptibility is given by (114),

$$\xi(k,z) = iz\beta S(k,z) - \beta C_T(k,0) \tag{3.4}$$

where $\beta = 1/k_B T$ with T the temperature and k_B the Boltzmann constant. In the next section we apply such ideas to test them.

3.1.1 Testing rigidity in glass-forming systems: Hard-disks model

Let us now apply the previous ideas to hard disks. This model is able to produce glasses and crystals. Here we consider a monodisperse and a bidispersive mixture of hard disks. In the monodisperse hard-disk system, the diameter of the disks is σ, while in the bidisperse case there are two kinds of disks, $\mathscr{A}$ and $\mathscr{B}$, each with diameters $\sigma_{\mathscr{A}}$ and $\sigma_{\mathscr{B}}$, respectively. For the monodisperse system, the packing fraction is given by $\eta = N\pi\sigma^2/A$ where A is the total area. For the bidisperse system $\eta = [N\pi(x\sigma^2_{\mathscr{A}} + (1-x)\sigma^2_{\mathscr{B}}]/A$, where x is the relative concentration of disks $\mathscr{A}$. In our simulation, we take $x = 1/2$ and $\sigma_A = 1.4\sigma_{\mathscr{B}}$. The monodisperse hard-disk system is interesting in many senses as crystallization takes place by two phase transitions. First the liquid goes into coexistence at $\eta \approx 0.70$ with the hexatic phase at $\eta \approx 0.7175$. This is captured by the orientational order parameter, such that in the hexatic phase orientational order appears and the transition is characterized by the Mayer-Wood loop in the $P-v$ diagram (116). As the packing fraction increases, a second order transition from hexatic to solid is observed at $\eta \approx 0.72$ (116; 115). While the hexatic phase has short range positional order and quasi-long-range orientational order, the solid has quasi-long range positional order and long-range orientational order. In this regard, positional order parameter is used to distinguigh between the hexatic and solid phase (116). Recently it has been observed that a small polydispersity destroys the hexatic phase (115). Moreover, the bidisperse system at $x = 1/2$ is able to generate a glass (117; 115; 118). In fact, there is a nice correlation between disk's mismatch, glass forming ability, configurational and vibrational entropy (118).

Additionally, we should mention that the ideas of the glass transition in 3D do not extrapolate to

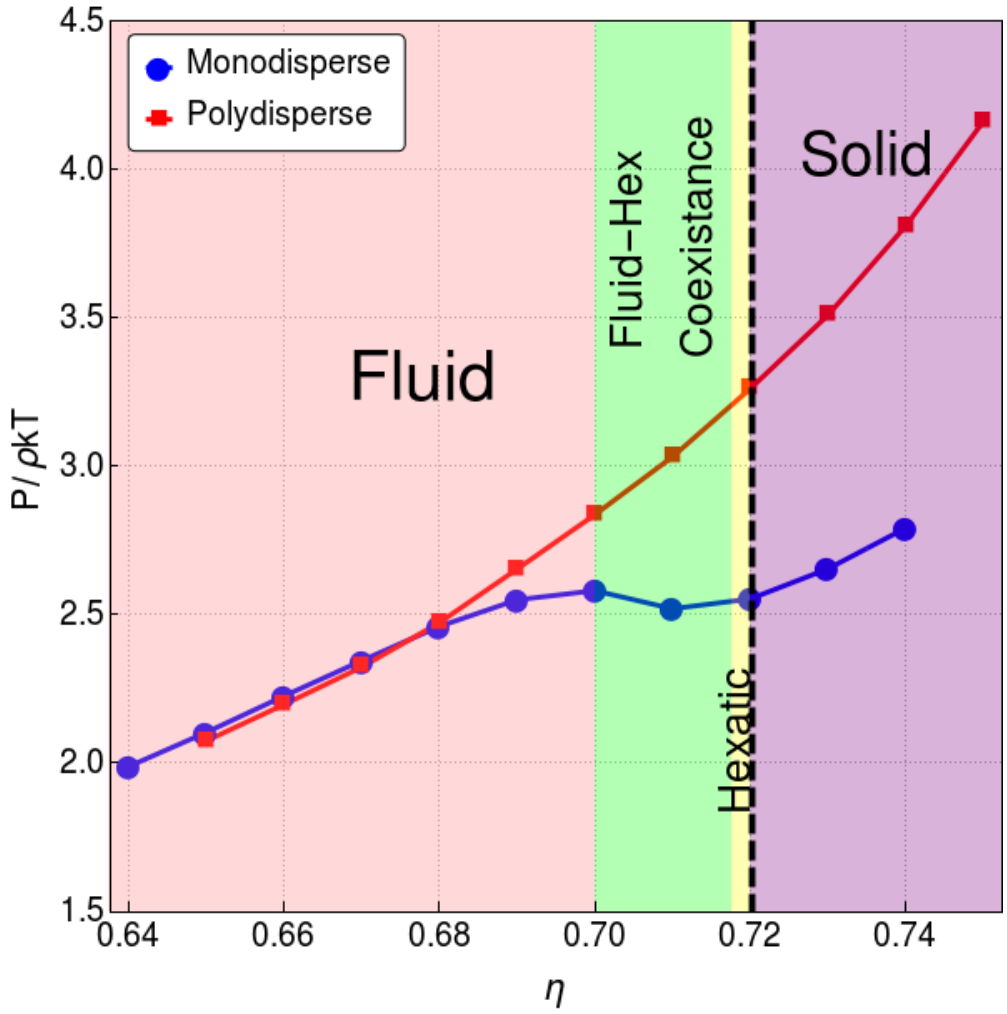

Figure 3.1: Pressure vs packing fraction in the studied region for monodisperse hard-disks (blue curve) and bidisperse hard-disks (red curve) as shown in the plot legend. For the case of monodisperse hard-disks, below $\eta \approx 0.7$ the system is in the fluid phase (colored pink), between $\eta \approx 0.7$ and $\eta \approx 0.7175$ the fluid coexist with the hexatic phase (colored green). Above $\eta \approx 0.7175$ the system is in a hexatic phase (colored yellow). At $\eta \approx 0.72$, a second order phase transition from hexatic to solid occurs (marked with a dashed line), and above $\eta \approx 0.72$ the system is in the solid phase (colored purple) (115). This plot was obtained from a simulation with $N = 2500$ hard-disks.

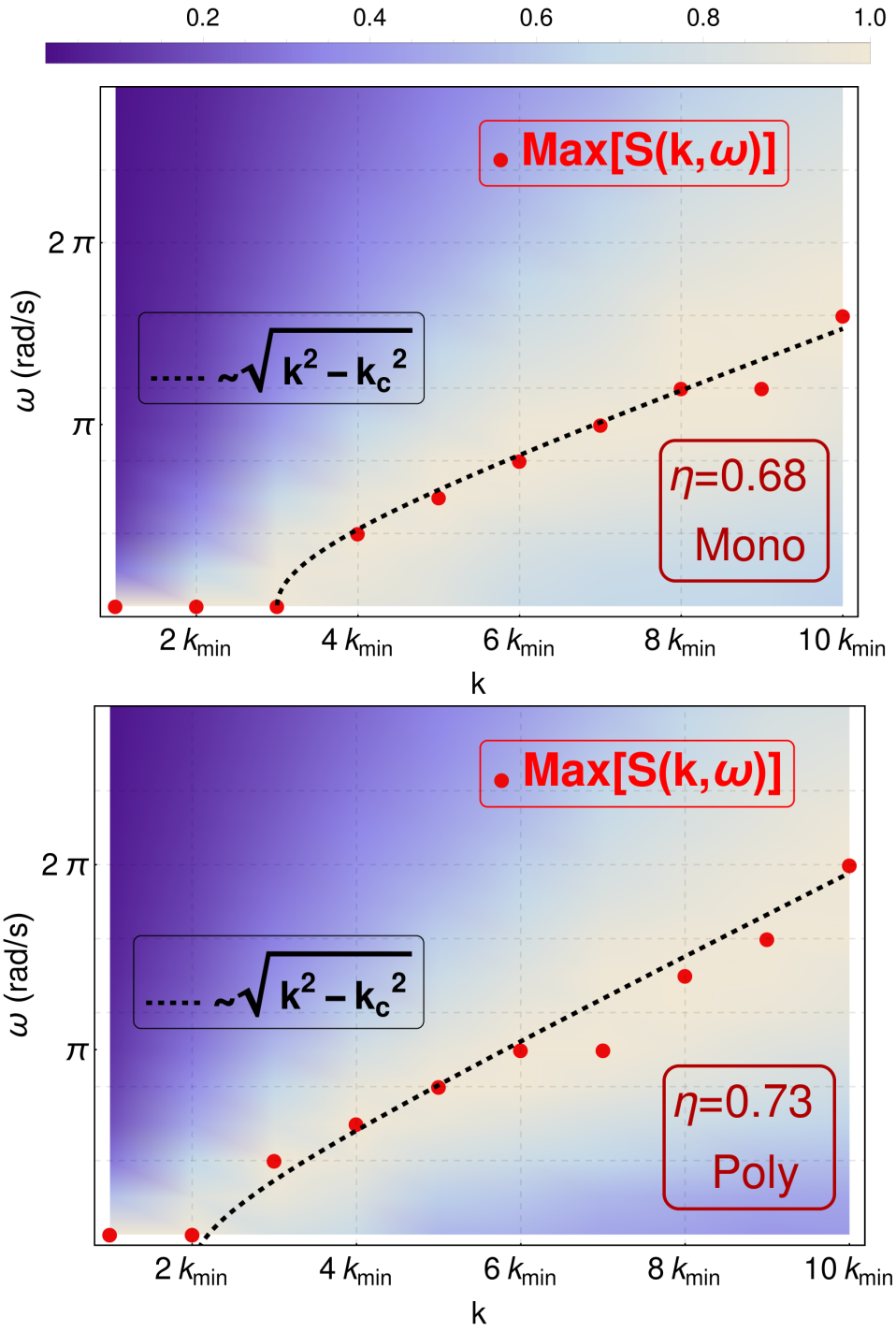

Figure 3.2: Contour plot of the normalized transversal dynamical structure factor $S(k,\omega)/(\max S(k,\omega))$ for $N = 2500$ in the case of (**Upper panel**) monodisperse hard-disk system with packing fraction is $\eta = 0.68$ and (**Lower panel**) polydisperse hard-disk system with packing fraction is $\eta = 0.73$. The red dots are the observed maxima. The dotted curve allows to compare with the indicated functional form. Notice the presence of a dynamical gap at $k < 2k_{min}$ in both cases (although at different packing fractions).

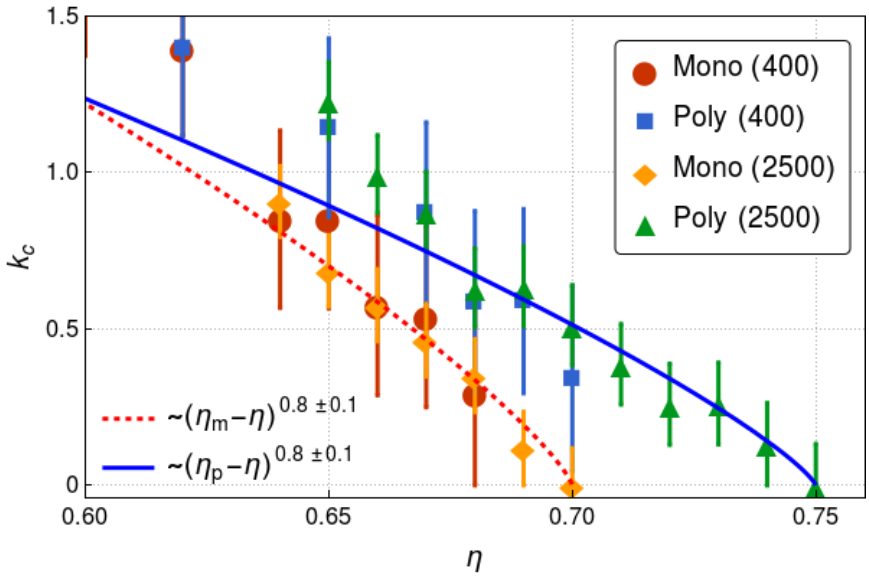

Figure 3.3: Dynamical gap vs packing fraction η. The data points correspond to the simulations while the dashed lines corresponds to fits (see legends). For $N = \{400, 2500\}$ in the case of monodisperse disks, the critical packing fraction for which $k_c = 0$ is $\eta_m = 0.7$ while for polydisperse disks $\eta_p = 0.75$. The error bars correspond to the resolution given by $2\pi/\sqrt{A}$, where A is the total area of the system.

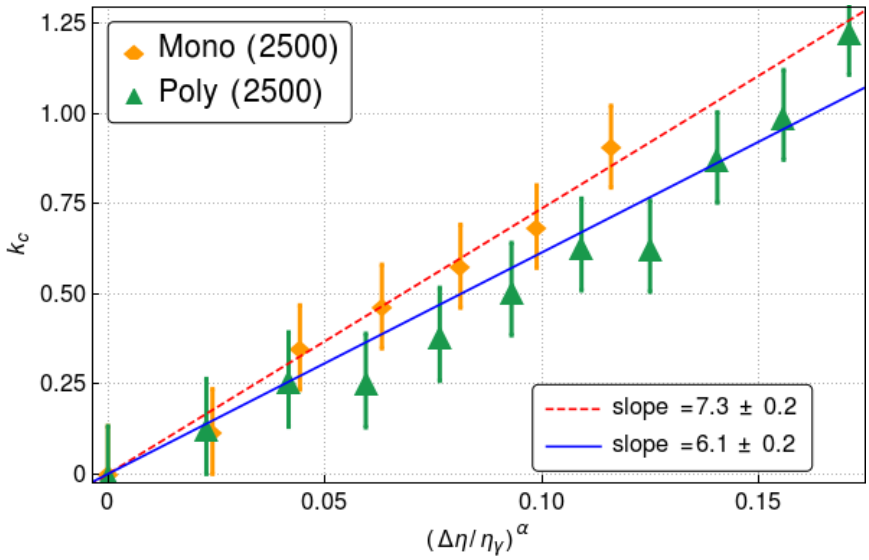

Figure 3.4: Plot of the dynamical gap vs reduced packing fraction $\left(\Delta\eta/\eta_\gamma\right)^\alpha$, where $\gamma = \{m, p\}$. The data points correspond to the simulations while the dashed lines corresponds to fits (see legends). The computations were made for systems with $N = 2500$ disks,

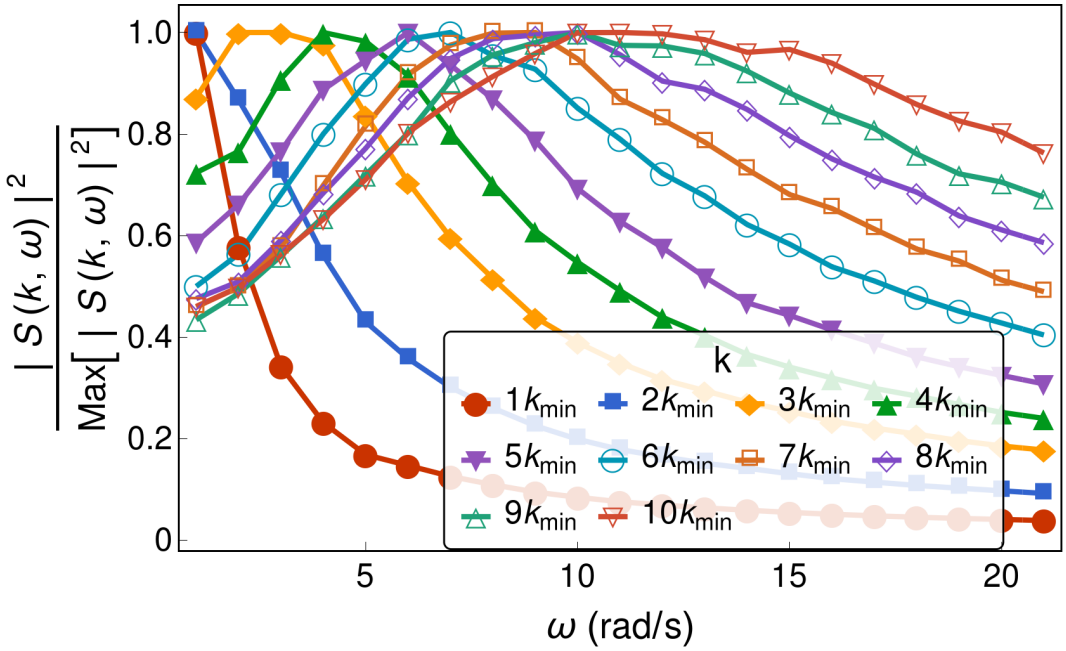

Figure 3.5: The transverse density current correlation function as a function of ω for different wavenumbers. This was obtained for polydisperse hard-disks at a packing fraction 0.73. Notice that for all curves where for $k < 3k_{min}$, the maximum is located at $\omega = 0$. For $k > 3k_{min}$, the peak moves to higher frequencies as k increases, indicating transversal wave propagation although with an increased damping.

2D glasses. Recent research in this direction provide a view on these differences (119–121). Hence, care must be taken and, in fact, these long range fluctuations have an effect on the size-dependence of the melting point (122). The results were obtained from an Event-Driven Molecular Dynamics simulation with $N = 2500$ hard-disks. An event driven molecular dynamics simulation called *DynamO* (123) was used while, in the case of bidisperse, the initial configuration was generated using the code developed by Torquato *et al.* (124). For hard potentials, particles interact only when the distance between them is equal to the sum of their radius. While this condition is not fulfilled, the velocity of the particles remain the same. Event-Driven Molecular Dynamics takes advantage of this by locating the next collision (i.e., the time when the collision will occur and the pair of particles that will collide), evolving the simulation up to that time and implementing the collision dynamics (125). The hydrostatic pressure is computed from the trace of the pressure tensor and divided by 3. However, since we are simulating 2D systems, the element $P_{zz} = 0$, therefore, we have rescale by 3/2. The way in which DynamO computes this tensor is from the kinetic and interaction contributions, i.e., the kinetic contribution is defined as

$$\boldsymbol{P}^{kinetic} = \frac{1}{V}\sum_{i=1}^{N} m_i \boldsymbol{v}_i \boldsymbol{v}_i \,, \tag{3.5}$$

where V is the volume, N the number of disks, $m_i = 1$ is mass, $\boldsymbol{v}_i$ is the velocity of disk i and $\boldsymbol{v}_i \boldsymbol{v}_i$ is the dyadic product which yields a matrix. The interaction contribution is defined as

$$\boldsymbol{P}^{interaction} = \frac{\sigma}{V t_{sim}} \sum_{i,j}^{event} \Delta \boldsymbol{p}_i \boldsymbol{r}_{ij} \,, \tag{3.6}$$

where t_{sim} is the total time of the simulation, the summation is over each two-particle event (collision), i and j indicate the two particles involved in the event, $\Delta \boldsymbol{p}_i$ is the momentum impulse on particle i, and $\boldsymbol{r}_{ij} = \boldsymbol{r}_i - \boldsymbol{r}_j$ is the separation vector between the interacting particles.

3.1.2 Results

In Figure 3.1 we present the evolution of the compressibility factor $P/\rho k_B T$ where $\rho = N/A$ as a function of η, where the pressure was obtained, as previously mentioned, by means of Eqs. (3.5) and (3.6). This result allows us to confirm that, in the case of monodisperse hard-disks, the system is undegoing a first order phase transition, while the bidisperse hard-disk system is not. Our aim is now to look at the viscoelastic response of both systems. In the upper panel of Figure 3.2 we present the transversal part of the dynamical structure factor $S(k,\omega)$ for the monodisperse system near the phase transition.

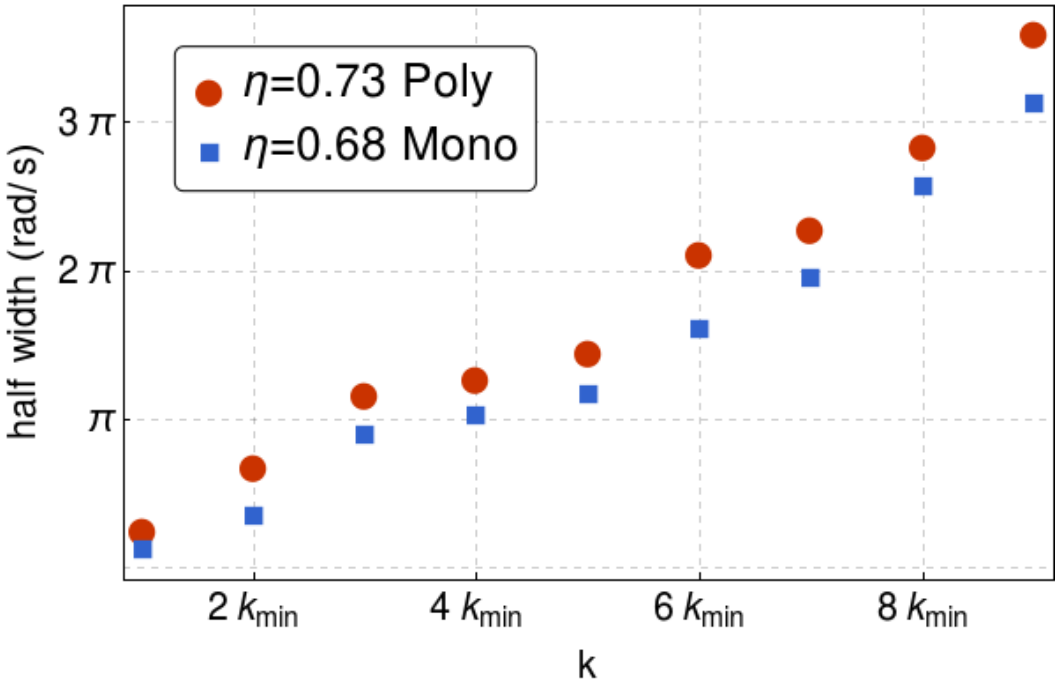

Figure 3.6: Half-width of the transverse density current correlation function as a function of the wavenumber for packing fraction $\eta = 0.68$ monodisperse and $\eta = 0.73$ polydisperse for 2500 hard disks. The half-width can be compared with the imaginary part of the dispersion relation in Eq. (3.12) (see main text for discussion). As k increase, the width becomes larger which is qualitatively consistent with (126; 127).

The colors here represent the values of $S(k,\omega)$ for different wavenumbers k given in terms of the lowest wavenumber $k_{min} = 2\pi/L$, where $L = \sqrt{\pi\eta/N}4/\sigma$. As k increases, the peaks in $S(k,\omega)$ shift to larger values of ω. A gap is seen between the peaks for $k \leq 2k_{min}$. Also, in Figure 3.2 we compare with the function $\omega(k) \approx \sqrt{k^2 - k_c^2}$, which shows a good agreement with a recent theoretical solid-state approach to liquids (126; 128; 129) (see Ref. (127) for a recent review on the subject). The lower panel of Figure 3.2 shows that the bidisperse melt also shows a similar transversal branch with a gap and a critical k_c. Recently, this phenomena has been called the dynamical gap (126).

Figure 3.2 gives a nice glimpse of the viscoelasticity and how a transition from a fluid-like to a solid-like behavior is revealed by the presence of a dynamical gap. What is most important to us, is the observation that for $k < k_c$ all peaks of $S(k,\omega)$ are at $\omega = 0$. Thus, in this region $S(k,\omega) \approx \delta(\omega)$, where $\delta(\omega)$ is the Dirac delta function. Since for $k < k_c$ we have $\omega = 0$, we can consider these states, in terms of rigidity, as floppy, i.e., the system is flexible. Another way to see this result is by observing that here the rigidity transition will depend upon the time-scale of observation.

To test these ideas, we further follow the behavior of k_c as a function of η up to the freezing packing fraction for the monodisperse case. Figure 3.3 shows the dependence of k_c. As expected, $k_c \to 0$ as $\eta \to \eta_m$, where $\eta_m = 0.7$ is the packing fraction where the system becomes solid for this system size. We should stress that for a larger system such as $N = 10^4$, $k_c \to 0$ at a packing fraction equal to ≈ 0.72 in the case of monodisperse hard-disks, in agreement with the hexatic-to-solid phase transition (115). This has to do with the long range fluctuations, which have an effect on the size-dependence of the melting point (122; 119–121). Figure 3.3 also shows the evolution of k_c for the bidisperse case. It is observed that $k_c \to 0$ as $\eta \to \eta_p$, where $\eta_p = 0.75$.

Thus, Figure 3.3 clearly shows that a rigidity transition will take place as the fluid density increases. Figure 3.3 has other interesting features. The first is that the bidisperse fluid presents a bigger dynamical gap for the same given packing fraction. From a rigidity point of views this is expected as the effective number of contacts is reduced. In fact, a previous test in solids showed how one can, by decreasing the size of some disks in a monodisperse system, create a Boson peak (105–107). Thus, Figure 3.3 gives a nice alternative to test in a quantitative way the underlying rigidity of the solid.

Another revealing aspect of Figure 3.3 is that the critical k_c seems to follow the law,

$$k_c \sim (\eta_\gamma - \eta)^\alpha \tag{3.7}$$

where $\gamma = m$ or $\gamma = p$ depending whether the system is monodisperse (m) or polydisperse (p). As k_c is the inverse of a dynamical length scale, α represents the scaling of this rigidity, suggesting to be a

critical exponent for the size of rigid clusters. Thus, it is expected to depend upon the dimensionality of the system (130).

To test this possibility we fitted the curves shown in Fig. 3.3 to the functional form given in Eq. (3.7). We obtained $\alpha = 0.8 \pm 0.1$ in both cases. We further fitted k_c *vs* $(\Delta\eta/\eta_\gamma)^\alpha$, where $\Delta\eta = \eta_\gamma - \eta$. In Figure 3.4 we show the fits and the legend shows the slope values.

In the hydrodynamic regime, $C_T(k,t)$ (Eq. (3.2)) satisfies the transverse part of the linearized Navier-Stokes Equation. Under very general arguments, it can be proved that the expression for $S(k,\omega)$ is given by (114),

$$S(k,\omega) = \frac{2v_0^2 k^2 \Gamma(k)/\tau(k)}{\left(\omega^2 - \left(k^2\Gamma(k) - \frac{1}{2\tau^2(k)}\right)\right)^2 + \left(k^2\Gamma(k) - \frac{1}{4\tau^2(k)}\right)\frac{1}{\tau^2(k)}} \tag{3.8}$$

Here $\Gamma(k) = G_\infty(k)/\rho$, where $G_\infty(k)$ is the wavenumber-dependent high-frequency shear modulus, ρ is the density, $v_0^2 = C_T(k, t=0)$ and $\tau(k)$ is the wavenumber-dependent relaxation time (114).

The condition for shear wave propagation is obtained from equating to zero the derivative of Eq. (3.8) with respect to ω. The resulting inequality for shear wave propagation is,

$$k^2\Gamma(k) > \frac{1}{2\tau^2(k)}\,. \tag{3.9}$$

As k decreases, $\Gamma(k)$ decreases much faster than $\tau(k)$. Thus, the inequality in (3.9) eventually breaks at a certain k_c, such that

$$k_c^2 \approx \frac{1}{2\tau^2(k_c)\Gamma(k_c)}\,. \tag{3.10}$$

In fact, Trachenko *et at.* (126; 127) studied the dynamical gap and provided a variation to the Navier-Stokes Eq. which in turn leads to the well-known telegraph's Eq., from that they obtain the following equationf for ω,

$$\omega^2 + \mathrm{i}\frac{\omega}{\tau} - V_t^2 k^2 = 0\,. \tag{3.11}$$

where τ is a relaxation time. Solving for ω yields

$$\omega_\pm = -\frac{\mathrm{i}}{2\tau} \pm V_t\sqrt{k^2 - k_c^2}\,, \tag{3.12}$$

the energy dispersion with a damping and a gap determined by $k_c = 1/2\tau V_t$, a result similar to Eq. 3.10 as $V_t \approx \sqrt{G_\infty(k)/\rho}$ for $k >> k_c$. Also notice that when $k_c = 0$ then V_t is the transverse sound of speed in the medium.

Notice that ω has a finite imaginary part. In Fig. 3.2 the frequency corresponds to the real part. Now, from linear response theory, it is easy to see that the inverse of the left-hand-side of Eq. (3.11)

is proportional to the susceptibility, hence, by Eq. (3.4) we would expected the imaginary part being encoded in the width of the peaks of the transverse density current correlation function. In Fig. 3.5 we have plotted $S(k,\omega)$ *vs* ω for different values of k, while in Fig. 3.6 we have plotted the width of the transverse density current correlation function *vs* the wavenumber, for 2500 hard disks with packing fractions $\eta = 0.68$ monodisperse and $\eta = 0.73$ polydisperse, respectively. As k increases, the width becomes larger, which would imply smaller relaxation times, in agreement with Refs. (126; 127; 114).

To test numerically Eq. 3.12 we proceed as follows. Consider for example the case of the polydisperse system for $\eta = 0.68$. First V_t is obtained from considering $k \gg k_c$ from where $\omega \approx V_t k$. This is the slope of the dotted line in Fig. 3.2, from where $V_t \approx 0.24\pi/k_{min}$. Next from Fig. 3.6 we obtain $1/(2\tau) \approx 0.68\pi$. Using Eq. 3.12 we find that $k_c \approx 2.83 k_{min}$, in good agreement with Fig. 3.2, in which $k_c \approx 2k_{min}$.

It is worthwhile to remark that our data satisfy Eq. (3.8), which contains the Maxwell relaxation relationship for viscoelasticity, as it can be proved that in the long wavelength limit, the relaxation time $\tau(k)$ is given by (114),

$$\tau(0) = \frac{\nu}{G_\infty(0)} \tag{3.13}$$

where ν is the viscosity. This relation holds for any k dependence of $\tau(k)$, even if we make the crude assumption of taking $\tau(k) = \tau(0) = \tau$.

Let us now return to investigate the connection of constraint theory with the dynamical gap. As the fluid is isotropic, we can obtain a relationship between k_c and the number of floppy modes as follows. First we can approximate the behavior for $k < k_c$ by a delta function, resulting in a simplified version of $S(k,\omega)$,

$$S_f(k,\omega) \approx \delta(\omega)\Theta(k_c - k) + \Theta(k - k_c)S(k,\omega) \tag{3.14}$$

where $\Theta(x)$ is the Heaviside function. The total number of modes with zero frequency in three dimensions is proportional to the volume of a sphere with radius k_c in the k-space,

$$N_f(k_c) \approx 2\int_0^{k_c} 4\pi k^2 dk = \frac{8\pi}{3}k_c^3 \tag{3.15}$$

where the factor 2 comes from the possible transversal waves polarizations. In 2D we have $N_f(k_c) \approx \pi k_c^2$.

The fraction of floppy modes (f) with respect to the total number of modes is obtained by normalization,

$$f_{3D} \approx \frac{2}{3}\left(\frac{k_c}{k_D}\right)^3,\ f_{2D} \approx \frac{1}{2}\left(\frac{k_c}{k_D}\right)^2 \tag{3.16}$$

The normalization factor k_D ($\gg k_c$) is the Debye wavevector (131) while the subscripts $3D$ and $2D$ refer to the dimensionality of the system. We can conclude that floppy modes are related with the dynamical gap seen in the viscoelastic properties.

Using Eq. (3.7), one can obtain a relationship between η and f valid for the monodisperse and polydisperse system,

$$f_{2D} \sim \frac{1}{2k_D^2}\left(\frac{\Delta\eta}{\eta_\gamma}\right)^{2\alpha} \tag{3.17}$$

In principle, we can go further by relating the previous results to obtain a dynamical average coordination. However, the lattice may have a strong heterogeneous character as floppy regions favor the maximization of vibrational entropy (58) and care must be taken since it is possible that the system may gain structure and order (132) as in the case of the network studied in (104) where floppy regions appear in a given coordination number window above the rigidity threshold. Relaxation is affected by this heterogeneity (133; 77; 62; 134).

For angular and radial forces are present it is known that the fraction of floppy modes $f_{3D} = 2 - 5z/6$, whereas for solely radial forces $f_{3D} = 1 - z/6$ (52). In $2D$, we have for pure radial forces $f_{2D} = 1 - z/4$. Using Eq. (3.16), for pure radial forces and in 2D we have the trend,

$$z_{2D} \sim 4\left(1 - \frac{1}{2k_D^2}\left(\frac{\Delta\eta}{\eta_\gamma}\right)^{2\alpha}\right) \tag{3.18}$$

This number can be compared with results obtained from the first-neighbor-counting obtained from collisions (135). In particular, we observe that for $k_c = 0$ we recover the condition for rigidity, and as k_c grows, the coordination number decreases as expected for a fluid system. Furthermore, it is known that the coordination number may be obtained integrating the radial distribution function in a small sphere of radius equal to the distance between two particles. The radial distribution function is related to the structure factor which in turn may be put in terms of the current density correlation function (114). Thus, it seems plausible to relate the coordination number with the current density correlation function and, in particular, with the dynamical gap. The outline is shown in Appendices C and D, however, we leave that for future work.

The ideas presented in this section is far from being concluded. Nevertheless, we end it by emphasizing that the dynamical gap may serve as an order parameter as well as a way to compute the floppy modes in a seemingly easy manner. In this manner, floppy modes not only affect the relaxation in glass forming systems but also affect the rigidity.

The last piece of the puzzle is provided in the following, where we show how the vibrational modes contribute to the vibrational entropy, that when maximized, leads to the formation of floppy mode

domains. Now, when the right coordination number is tuned, at a certain temperature there is a phase transition from a heterogeneous phase to a homogeneous phase, which we further relate to the liquid-liquid transition.

3.2 The intermediate phase and the liquid-liquid transition

3.2.1 Introduction

It is no surprise that a single-component liquid may have multiple liquid phases. In fact, they may coexist and when this happens, this phase transition is called the liquid-liquid transition (LLT), where a high-density liquid (HDL) coexist with a low-density liquid (LDL). There is an increasing number publications in which they provide experimental and numerical support for the LLT in different systems which what they usually have in common is the internal tetrahedral structure (136–141). Nevertheless, there is still a lack of evidence which makes the LLT subject of much debate. This has to do with the fact that in some systems, the LLT occurs at high temperatures and high pressures making it hard to measure it experimentally. In the case of water, however, the LLT occurs in the metastable supercooled region. In general, this is also true for molecular systems (142–148) which also makes it difficult to observe it experimentally. Nonetheless, evidence points to the LLT being a first-order phase transition. In the case of water, for instance, the critical temperature is around $T_c \approx 245K$ and a critical pressure $P_c \approx 200\ MPa$. Furthermore, this coexistence line has a negative Clapeyron slope (148).

The LLT picture in water seems rather appealing since it may explain certain features such as the thermodynamical and dynamical anomalies when reaching the supercooled region and, perhaps, there could be a connection between the LDL and HDL with the low and high density amorphous ice (143; 147). In the latter case, it is worthwhile mentioning that a few years ago Sellberg *et al.* were able to quench droplets of liquid water below the homogeneous ice nucleation temperature and study the structure factor in an effort to experimentally relate it with the low density amorphous ice (LDA) (149).

As previously mentioned, one thing where there seems to be consensus is that the LLT is due to the microscopic tetrahedral geometry. Several theoretical approaches have been used to understand this LLT (see for instance (144)). The HDL is characterized by low volume and high disorder while the LDL is characterized by a high volume and low disorder with a structure similar to the LDA (149). In

a recent work by Kobayashi and Tanaka (146), they propose a two-order parameter model of the LLT based on the idea of locally-favored structures. In this regard, we propose the vibrational entropy as the thermodynamical quantity that triggers the liquid-liquid transition, similar to the intermediate phase transition observed in chalcogenides. In addition, this model shows reversibility and a jump in the specific heat in correspondence with a first-order phase transition, which is in agreement with experiments (140; 146; 145).

As has been mentioned previously, in network glasses including chalcogenides, the coordination may be tuned by changing the chemical compositions. As the coordination number, z, increases, there is a rigidity transition which is predicted in covalent networks by constraint counting (18; 52) to occur at $z_c = 2.4$. Interestingly, as the composition is varied, an intermediate phase has been revealed in the vicinity of the rigidity onset (31; 32) where a number of features change dramatically. For example, it has been shown that glass formers in this intermediate phase are reversible in terms of heat absorption and release at glass transition, and also become strong in terms of dynamical fragility. These features are singular with respect to those of the glass formers out of the phase. On the other hand, the calorimetry experiments imply a first-order phase transition in some strong glass-forming liquids above the glass transition temperature. In Ref. (104), it was shown how this first order phase transition is a homogeneous-heterogeneous first-order phase transition triggered by the vibrational entropy. It was further shown that this phase transition occurs in a coordination number window proportional to the vibrational entropy gain per floppy mode. We propose that this intermediate phase transition is intrinsically a LLT.

There are many examples of systems where the increase of entropy generates order and heterogeneity (132). The ingredients necessary for this type of behavior are two-fold, namely, high configurational degeneracy and the ability of a given system to cluster degrees of freedom carrying the most part of the entropy. In principle, both are part of the features in liquids. The key idea is understanding that floppy modes store large amounts of entropy (150).

In network glasses, the material properties relying on structures can be tuned by changing the chemical compositions that have different abilities to make covalent connections with neighboring atoms. In chalcogenides $Ge_xAs_ySe_{1-x-y}$, for example, selenium (Se) forms only two bonds while arsenic (As) and germanium (Ge) form three and four respectively. First pointed out by Maxwell (151), a general network will lose rigidity as the network connectivity is reduced to below certain critical

connectivity when the average number of constraints per atom, n, is equal to the degrees of freedom, i.e., $n_c = d$ in spatial dimension d. This rigidity loss also applies to the chalcogenides when selenium concentration is high, predicted by Phillips in (29; 30), where he showed that counting both radial and angular constraints of covalent bonds gives $n_{\mathrm{Se}} = 2$, $n_{\mathrm{As}} = 9/2$, and $n_{\mathrm{Ge}} = 7$, indicating a chalcogenide glass is marginally rigid at a composition with average number of covalent bonds $r_c = 2.4$. Since then, more and more works have shown that the thermodynamic and dynamic features of glass-forming liquids (not limited to chalcogenides) are strongly regulated by the rigidity transition of the microscopic networks (152–155). One of the most interesting discoveries is the intermediate phase (IP) near r_c (156–159), which remains a big puzzle.

The intermediate phase appears to be singularly distinct from the adjacent rigid or floppy phases: the non-reversible heat, a glass-transition equivalent of the latent heat, vanishes (156); the stress heterogeneity disappears (157; 158); the molar volume and fragility are sharply smaller (159). All available pieces of evidence suggest that the glass undergoes some transitions when entering IP from either side (159). However, both, Maxwell's rigidity theorem and the rigidity percolation theory that takes into account fluctuations of random networks (160–162) predict only a single transition in network constraint number n. Noticed the interval of the two rigidity transition points in two theories, Thorpe and his colleagues proposed a self-organized transition scenario, which predicts a rigidity window in between two transitions – one corresponding to the loss of percolating rigidity as in the rigidity percolation theory and the other corresponding to the loss of ability to relax stress as in the Maxwell's theorem (163; 164). This stress-free rigidity window relies on a subtle balance between the fluctuation or entropy facilitating the rigidity percolation and the energy eliminating the stress throughout the range, which is, however, fragile to the ubiquitous perturbations such as Van der Waals (VdW) forces and temperature (165). Despite in a more recent paper (166), Kirchner and Mauro provide a robust approach of computing the constraint number to determine IP in the presence of finite temperature, the heterogeneous nature captured by a diverging correlation length at $n = n_c$ (167), in fact, still contradicts the observations of a homogeneous IP.

An alternative set of theoretical insights on IP is from the molecular dynamics simulations (168–170), where a similar intermediate range of homogeneous structures is revealed by continuously tuning the pressure instead of composition. In the simulation, as the pressure gradually increases, the amorphous structure undergoes a liquid-liquid transition (LLT) from a more structured low-modulus low-density amorphous phase to a more homogeneous rigid high-density phase (171). When the

composition is varied, the transition pressure shows a non-monotonic pattern with a lower value in an intermediate range near r_c, same as the pattern of the stress percolation pressure in chalcogenides (157). In addition, in experiments, a transition between two thermodynamically different liquids is indicated by a lambda peak in specific heat at a temperature above the glass transition in some strong glass-formers close to the rigidity threshold, including silica (SiO_2) (172–174; 139). These materials imply that the glass in IP may be in a rather different thermodynamic phase resulted from a transition above the glass transition, and the transitions to IP directly reflect such liquid-liquid transitions. So what are the two different liquid phases in network glass?

In Ref (175) it was shown, with a network model, that the vibrational entropy facilitates the rigid-floppy separated heterogeneous network structures close to the rigidity transition n_c as floppy modes store large amounts of vibrational entropy (150), while cost little configurational entropy in marginally rigid networks. On the opposite, the elastic energy is lower in homogeneous structures with stresses evenly distributed (165). So under cooling, a network near n_c inevitably undergoes a first-order transition from an entropy-dominated heterogeneous phase to an energy-dominated homogeneous phase. The interplay between the glass transition temperature T_g and the LLT temperature T_{LLT} would then be key in determining in which liquid phase the material is frozen at the glass transition and all the consequential features. Here, we investigate the transition separating the two liquid phases by studying the thermodynamics of the same network model. We show that the network undergoes a first-order phase transition where the free energy crosses over, the associated energy and the entropy are discontinuous, and the specific heat jumps in the thermodynamic limit. Finally, we discuss how this liquid-liquid transition could be probed in experiments in order to understand the intermediate phase.

3.2.2 Model

We consider a two-dimensional triangular lattice of N particles with periodic boundary conditions (165; 176; 175), where a small deformation of the lattice is imposed to avoid non-generic singular modes, yet this deformation is periodic for reproducibility between simulation samples. We model all radial and angular constraints of covalent interactions by $N_s = Nn$ linear springs of stiffness k, connecting the nearest neighbors on a triangular lattice, as shown in Fig. 3.7. We incorporate quenched disorder of glassy energy landscape by setting mismatches between the springs' rest length and the fixed lattice bond lengths: $l_\gamma = l_{\gamma,0} + \epsilon_\gamma$ for spring γ. Mismatches $\{\epsilon_\gamma\}$ are independent identically distributed (i.i.d.)

random Gaussian variables with mean zero and variance ϵ^2. By setting $k_B = 1$, $k\epsilon^2 = 1$ defines the unit of, both, energy and temperature. Furthermore, we include also the weak VdW interactions by adding weak fixed springs of stiffness $k_w \ll k$ connecting any particle to all its six next-nearest neighbors as shown in Fig. 3.7. The mean-field effect of these weak long-range nonspecific interactions can be captured by a control parameter $\alpha = k_w/k \ll 1$ (155; 176).

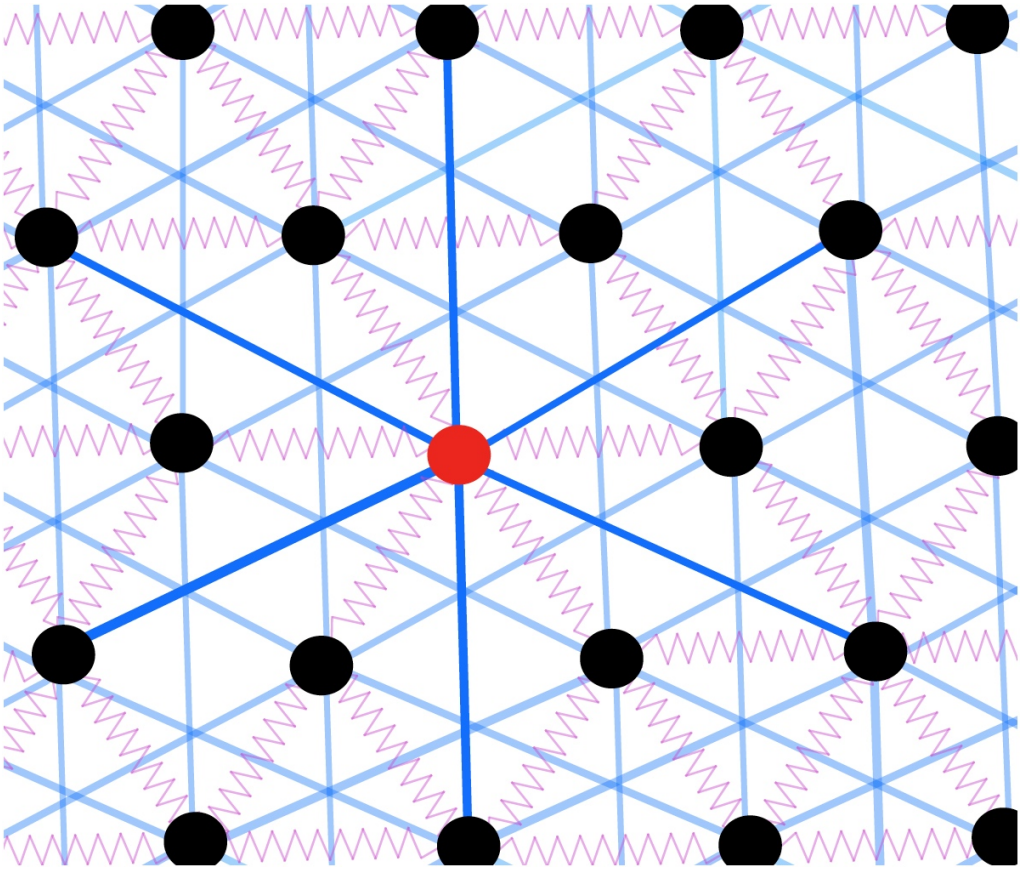

Figure 3.7: Sketch of the model. The black circles represent the particles, the purple springs represent the strong interaction between nearest neighbors while the blue lines represent the VdW interactions between next nearest neighbors. We color one of the particles in red with bold blue lines for illustration purposes.

In the model, the microscopic configuration depends on how the network is connected or which lattice bonds are occupied by strong springs, denoted by $\Gamma \equiv \{\gamma \leftrightarrow (i,j)\}$, for particle i and j connected by spring γ. Given Γ, when particles deviate from the mechanical equilibrium by $|\delta\mathbf{R}\rangle$, the elastic energy potential to the linear order is,

$$V(\Gamma, |\mathbf{R}\rangle) = H(\Gamma) + \frac{1}{2}\langle\delta\mathbf{R}|\mathscr{M}(\Gamma)|\delta\mathbf{R}\rangle, \tag{3.19}$$

where H is the energy of the inherent structure of configuration Γ and the second term corresponds to the vibration from equilibrium with $\mathscr{M}$ being the Hessian matrix of energy H. We thus perform a Metropolis Monte Carlo simulation (177) to sample the configurations according to their Boltzmann weight $e^{-F(\Gamma)/T}$ with free energy,

$$F(\Gamma) = H(\Gamma) - TS_{\text{vib}}(\Gamma), \tag{3.20}$$

with the volume of thermal vibrations counted in the vibrational entropy,

$$S_{\text{vib}}(\Gamma) = n_c N \ln T - \frac{1}{2}\ln\det\mathscr{M} = -\sum_{\omega}\ln\omega(\Gamma) + c, \tag{3.21}$$

where ω^2 are the eigenvalues of the Hessian matrix $\mathscr{M}$ and n_c is the critical constraint number, which is equal to 2 in two dimensions.

Without loss of generality, we assume the independence of mismatch ϵ_γ on the particle distances of the distorted lattice r_{ij} so that the Hessian matrix becomes only a function of the occupation $\{\sigma\}$, where $\sigma_{ij} = 1$ if particle i and j are connected by a spring and $\sigma_{ij} = 0$ otherwise. The stress energy of the network at mechanical equilibrium can thus be computed by,

$$H(\Gamma) = \frac{1}{2}\langle\epsilon|\mathscr{K} - \mathscr{K}\mathscr{S}\mathscr{M}^{-1}\mathscr{S}^T\mathscr{K}|\epsilon\rangle\,, \tag{3.22}$$

where $\mathscr{K}$ is the diagonal spring stiffness matrix and $\mathscr{S}$ is the structural matrix, both depending only on occupation $\{\sigma\}$. The detailed derivations and expressions of these matrices and the numerical implementation are documented in the Appendix E.

3.2.3 Results

Network structures

As proven in Ref. (150; 175) and directly inferred by Eq. 3.21, vibrational entropy is large for floppy modes with a vanishing ω. When the total number of constraints is fixed, the total entropy can gain from additional floppy modes in a phase separation of a very rigid subnetwork where the springs cluster and a very floppy counterpart where floppy modes cluster. This phase separation is shown in the snapshot of a system of 576 particles at high temperature in the upper panel of Fig. 3.8. On the contrary, networks with constraints homogeneously distributed store lower elastic energy than other configurations given the number of springs, as shown in Ref. (165). At low temperature, when elastic energy dominates, homogeneous microscopic structures with no rigid-floppy phase separation will

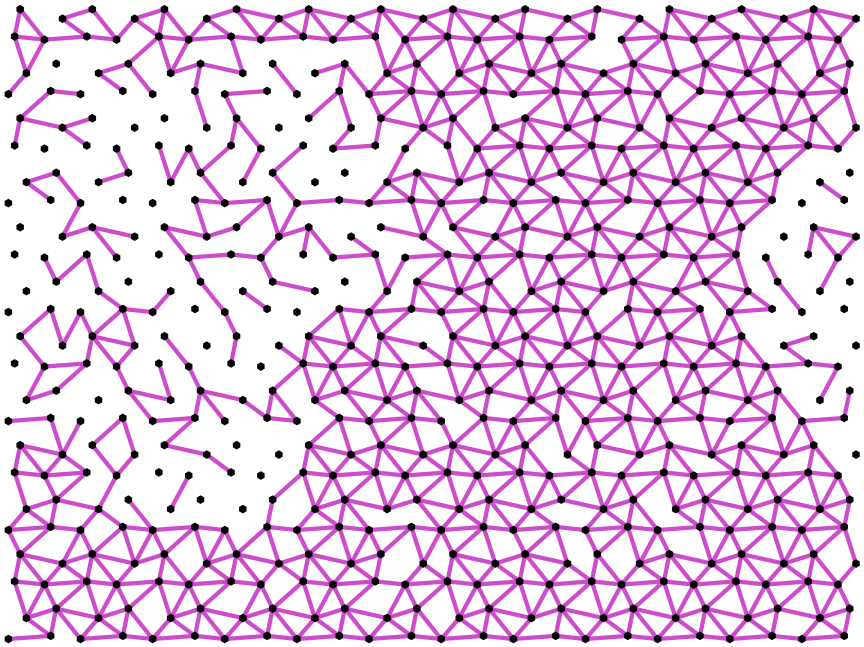

(a)

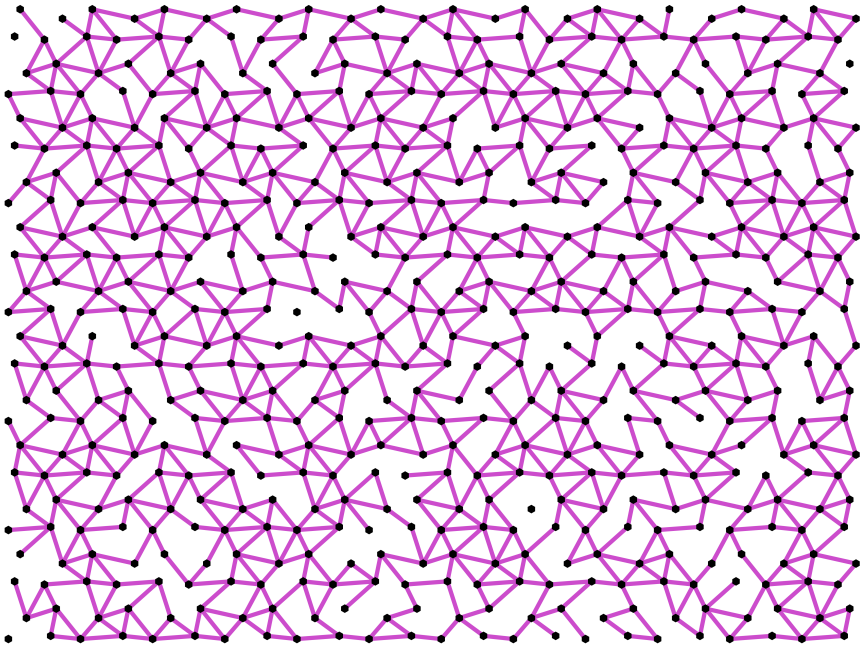

(b)

Figure 3.8: Snapshot of the system above (**a**) and below (**b**) the critical temperature for a system of 576 particles with the constraint number $n = 2.06 > n_c$. The purple lines represent the springs. **a**) Heterogeneuous structure: At high temperature $T = 10$, the entropy dominates over the internal stress energy, in particular, the vibrational entropy maximizes by phase separating into rigid and floppy regions. **b**) Homogeneous structure: At low temperature $T = 0.001$ the energy of the inherent structures dominates over the internal energy, this energy minimizes by a homogeneous distribution of constraints.

be sampled, as shown in the lower panel of Fig. 3.8. In the following, we will show that these heterogeneous and homogeneous structures correspond to two distinct thermodynamic liquid phases that are separated by a first-order liquid-liquid transition at a critical temperature T_{LLT}. We will further argue that depending on the relation between T_{LLT} and the glass transition temperature T_g, the liquid can be frozen into different thermodynamic phases, which could be the origin of the singular intermediate phase in network glass.

Thermodynamics

The numerical results of thermodynamics of the model are shown in Fig. 3.9 together with the theoretical predictions of both heterogeneous and homogeneous phases. In the upper left panel of Fig. 3.9, for a given connectivity $n = 2.06$, we find the total free energy of the networks equilibrated at given temperature T can be perfectly fitted by the theoretical predictions of heterogeneous networks at high temperature end (in red) and of homogeneous networks at low temperature end (in blue). Moreover, the numerics and the free energy prediction of heterogeneous networks are consistently lower than the prediction of the homogeneous phase when the temperature is higher than certain transition temperature $T_{LLT} \approx 0.2$. At the free energy crossover T_{LLT}, marked in Fig. 3.9(b)(c)(d), we are also observing the convergence to discontinuous jumps at the transition in the thermodynamic limit $N \to \infty$ from a higher value in high temperature heterogeneous phase to a lower value in the low temperature homogeneous phase in stress energy, vibrational entropy, and the specific heat. This result demonstrates that the heterogeneous and homogeneous structures are thermodynamical phases, separated by a first-order phase transition where, both, energy and entropy are discontinuous.

In Fig. 3.9, the data points of energy $E = \overline{H}^T$ in the upper right panel of Fig. 3.9 and vibrational entropy $S_v = \overline{S_{\text{vib}}}^T$ in the lower left panel of Fig. 3.9 are averages of Eqs. (3.21) and (3.22) over the Monte Carlo courses at given temperature T. The specific heat C in the lower right panel of Fig. 3.9 is obtained from the mean energy fluctuation over the Monte Carlo courses normalized by temperature squared, $C = (\overline{H^2}^T - E^2)/T^2$. Finally, the main numerical result of free energy F in the upper left panel of Fig. 3.9 combines both direct measurement of energy E and the inferred total entropy $S = S_v + S_c$ by integrating over the specific heat C,

$$S(T) = S(\infty) - \int_T^\infty \frac{C(T)}{T} dT, \tag{3.23}$$

as $F = E - TS$. The theory derivations and the way we consistently fit parameters are fully documented

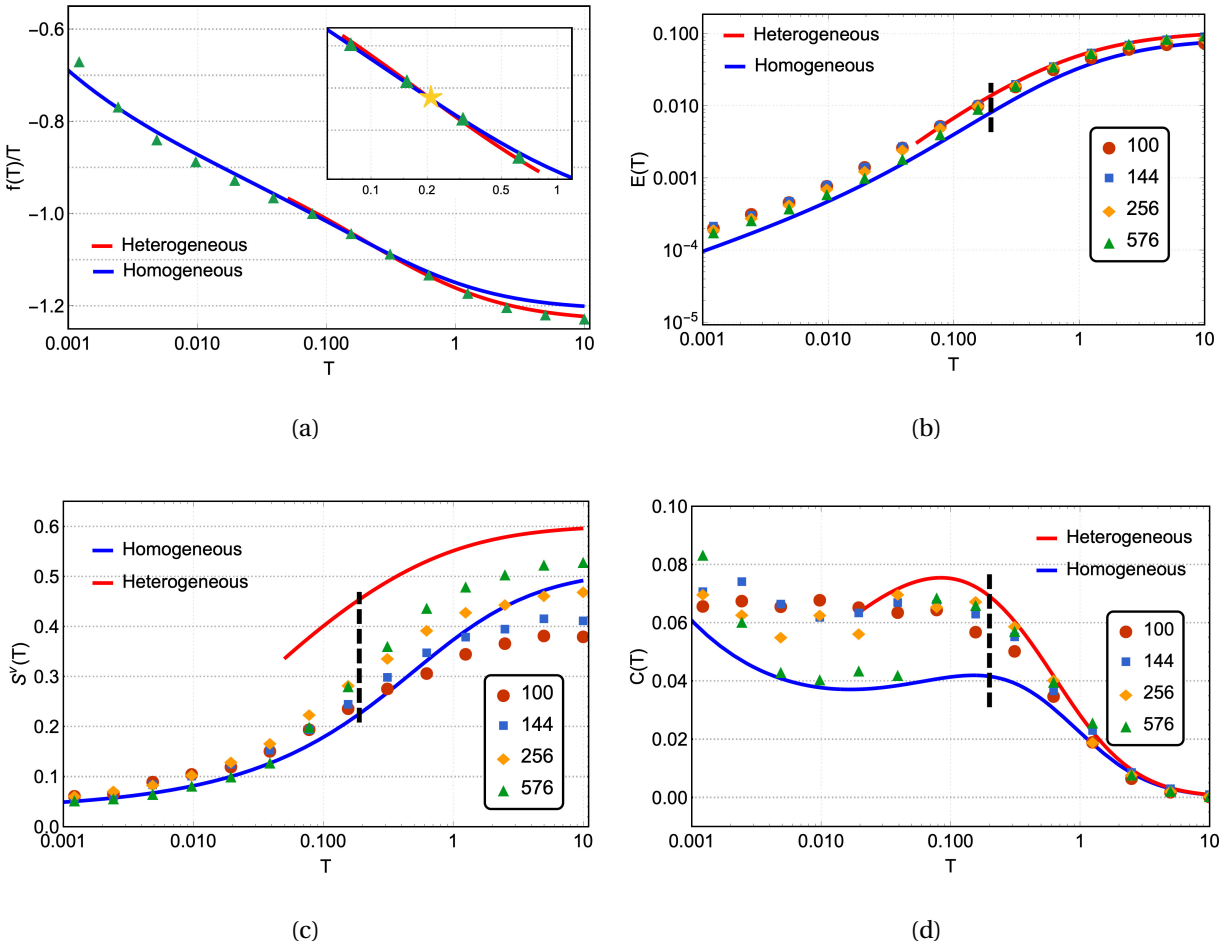

(a) (b) (c) (d)

Figure 3.9: Thermodynamics of the network model near the rigidity transition $n = 2.06$. The thermodynamics is characterized by the basic thermodynamic quantities, including free energy, internal energy, entropy, and specific heat, shown versus temperature as symbols for simulation results and as solid lines for analytical predictions. The simulations are done for different system sizes N (see legends) and the analytical predictions are obtained in the thermodynamic limit $N \to \infty$ for homogeneous networks in blue and heterogeneous networks in red (see Appendix E for detailed descriptions). **a)** The numerical results of free energy follow the prediction of a homogeneous network at low temperatures until the homogeneous-heterogeneous first order phase transition around $T \approx 0.2$ and then cross over to the prediction of a heterogeneous network. The yellow star in the inset marks this crossover. **b)** Data points follow the homogeneous and heterogeneous predictions in the same low and high temperature ranges corresponding to the free energy, while separated by a discrete transition that the numeric result is converging to in the thermodynamic limit. **c)** Similarly, the vibrational entropy results also converge to a discrete jump at the crossover of free energy. **d)** At the phase transition, the specific heat is also characterized by has a jump, seen in the largest system size.

in the Appendix E or see Ref. (176) for homogeneous networks and Ref. (175) for heterogeneous networks.

Spatial and temporal correlations

We have shown the existence of two distinct thermodynamic liquid phases of networks with the basic thermodynamic quantities. Among these quantities, the specific heat is a good experimental indicator to detect the two liquid phases and the transition: one can look for a lambda divergence or a peak in specific heat above glass transition T_g, as found in certain strong-type glass-forming liquids and water (172–174; 139). Here we present also the spatial and temporal correlation profiles of the two phases that could be directly measured in experiment to probe the transition. The spatial and temporal correlations are investigated by the structure factor and the time autocorrelation function as shown in Fig. 3.10. They are defined by the occupation $\{\sigma\}$ as,

$$S_f(k) = \frac{1}{3N(3N-1)} \sum_{ij \neq kl} (\sigma_{ij} - \bar{\sigma})(\sigma_{kl} - \bar{\sigma}) e^{ikr_{ij,kl}}, \tag{3.24}$$

$$G(t) = \frac{1}{T_{tot} - t} \sum_{\tau} \frac{1}{3N} \sum_{ij} [\sigma_{ij}(\tau) - \bar{\sigma}][\sigma_{ij}(\tau + t) - \bar{\sigma}], \tag{3.25}$$

where $\bar{\sigma} = n/3$ and $r_{ij,kl}$ denotes the distance from the center point between node i and node j and the center point between node k and node l.

For temperatures higher than the transition temperature $T_{LLT} \approx 0.2$, we observe a plateau to finite correlation in the time range scanned in simulation and a strong signal in structure factor averaged over that time scale, which reflects the heterogeneous phase as in the snapshot in the left panel of Fig. 3.8. On the contrary, for temperatures lower than T_{LLT}, we observe normal homogeneous liquid, where the correlation quickly relaxes to zero with no special structure in wave vector space after averaged over time, as in the snapshot in the right panel of Fig. 3.8. In the left panel of Fig. 3.10, we also notice that the systems in the heterogeneous phase yield two relaxation times: the system first relaxes to a plateau rapidly, yet in this plateau, the system is also relaxing but with a much larger characteristic time. It implies that the rigid and floppy clusters are not held fixed in a given position and the structural features in $S_f(k)$ will also vanish when averaged at the time longer than the second relaxation as in liquids. These features of spatial and temporal correlations emerging at an intermediate time scale should be looked for in distinguishing the two liquid phases and detecting the transition.

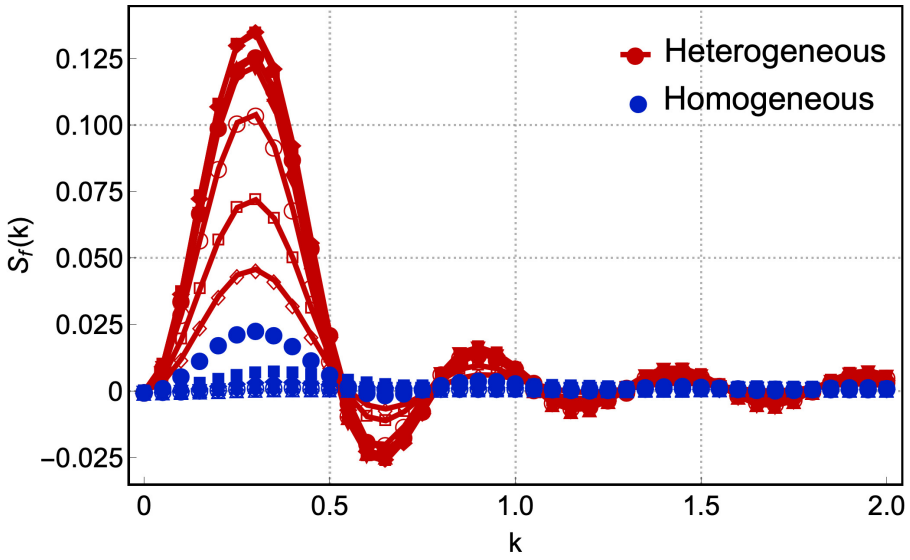

(a)

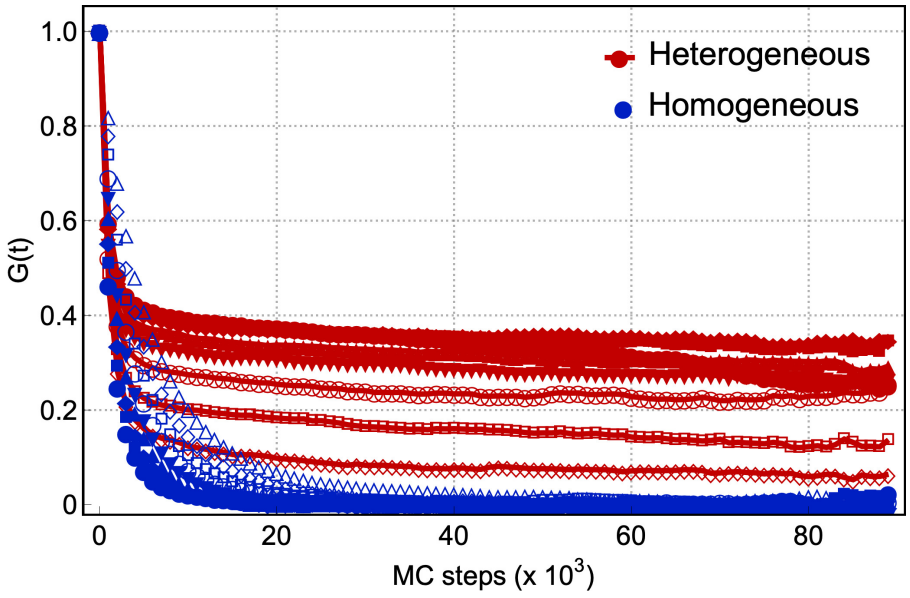

(b)

Figure 3.10: **a**) Spatial correlation function and **b**) time correlation function for $N = 576$. Red curves correspond to temperatures $T(m) = 10/2^m$ with $m = \{0,...,5\}$ and blue curves correspond to temperatures $T(m)$ with $m = \{6,...,16\}$. The blue open symbols correspond to temperatures $T \lesssim \alpha$, i.e. of the order of the weak interactions. The wavenumber k has been averaged over three different directions. The time correlation function was computed using samples taken every 10^3 Monte Carlo steps.

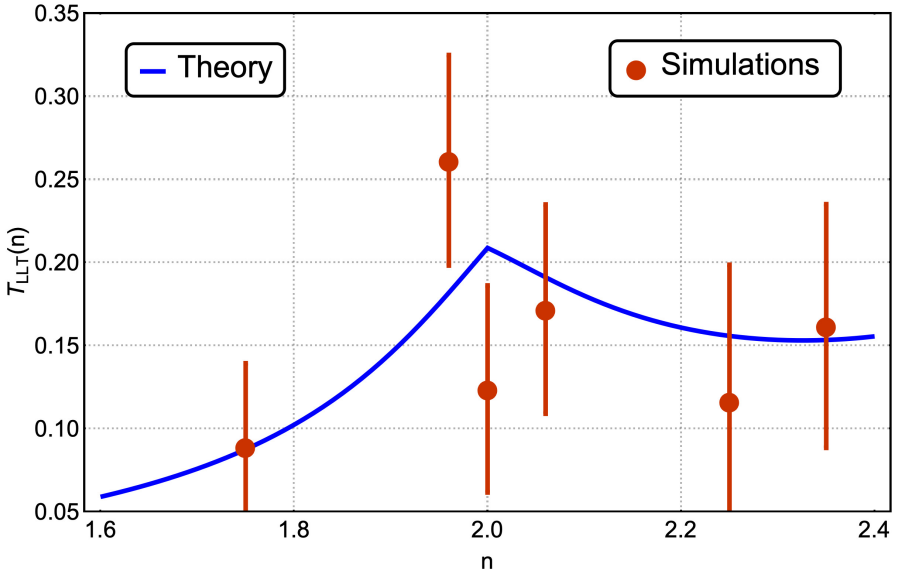

(a)

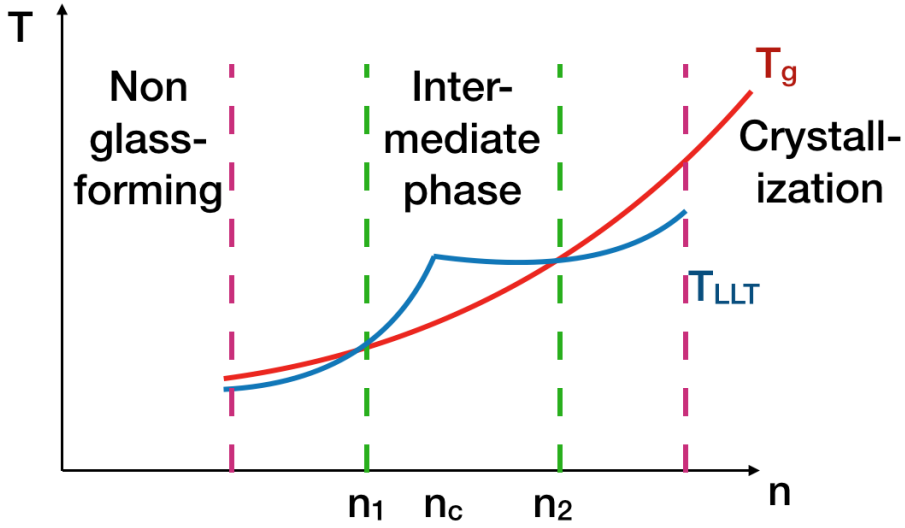

(b)

Figure 3.11: **a**) Liquid-liquid transition temperature vs number of constraints, predicted by theory (blue line) and measured numerically for the network model for $N = 256$ (data points). Details of the theory and numerical extraction of T_{LLT} are documented in Appendix E. The error bars correspond to the peak size of the heat capacity when the phase transition occurs. **b**) Illustration of different dependence of T_{LLT} and the glass transition T_g on the number of constraints n. When n is close to n_c where T_{LLT} becomes greater than T_g, the liquid is frozen in a homogeneous intermediate phase at T_g.

Dependence on network topology

Finally, we derive the liquid-liquid transition temperature T_{LLT} for varying constraint number n but close to n_c where a heterogeneous phase exists at high temperature, shown in Fig. 3.11(a) [1]. Unlike the glass transition temperature T_g, which increases monotonically with n, T_{LLT} varies non-monotonically and is maximal at $n = n_c$, which is also consistently shown by numerical results of the model as data points in Fig. 3.11(a). This result implies that for certain range of parameters, the networks undergo LLT to a thermodynamic homogeneous phase before they are dynamically trapped in glass, when $T_{LLT}(n) > T_g(n)$ or $n_f < n < n_r$, which is likely to occur in the vicinity of the rigidity threshold n_c due to the different dependences of T_{LLT} and T_g on n. The liquids frozen in homogeneous networks become glass in the IP, while the network glass out of the IP is then frozen in the heterogeneous network structures as the glass transition happens first under cooling, as illustrated in Fig. 3.11(b). The transitions to the IP are thus transitions between different frozen thermodynamic liquid phases in this picture.

PCA and unsupervised learning

As a proof a concept we applied Principal Component Analysis to the model to gain structure information. This approach is also known as *unsupervised learning* (181; 182), however, we believe this is rather misleading. We should also point out that PCA is a vast field and what we present here is solely a small part of the overwhelming literature concerning PCA. The nice thing of this approach is that it is fairly simple to apply and, in principle, no previous insight regarding the model is necessary. In Ref. (181) this method was applied to the 2D Ising model to obtain the order parameter that differentiates the ferromagnetic and paramagnetic phases.

The outline of the method is simple and straightforward, we construct the covariance matrix of the spring sites in our model. Then we compute the eigenvalues of the covariance matrix. This is shown in Fig. 3.12. Notice that the first two eigenvalues have more weight that the rest of the eigenvalues. This means that the eigenvectors associated with the first two eigenvalues contain most of the infor-

[1] Notice that the temperature predicted here is in the unit of covalent bond bending and stretching energy. For instance, in the case of silica with an average constraint number $n_{SiO_2} = 3.67$, the liquid-liquid phase transition temperature has been experimentally reported at $T_{LLT} \approx 1820K$ (178; 179) and glass transition at $T_g \approx 1425K$. The bond energy is estimated at $621.7kJ/mol$ (180), and the bond bending/stretching energy can be estimated by Lindemann's criterion with $k\epsilon^2 = 2 \times 0.3^2 \times 621.7 \approx 112kJ/mol$. We then have $T_{LLT} \approx 0.14$ and $T_g \approx 0.11$ in the unit of $k\epsilon^2$ for silica.

mation of the covariance matrix, which means that contain most of the information of the model as the temperature decreases.

In Fig. 3.13 we have plotted the first two eigenvector while coloring each tuple, form by one element from each eigenvector, according to the temperature. In this sense, bright red corresponds to $T = 10$ while blue corresponds to $T \approx 0$. Notice there is a small cluster in the upper right corner of the plot, which corresponds to the heterogeneous phase. The spatial separation between this cluster and the rest of the plot points suggests a phase transition (but, of course, is not a proof of a phase transition). This results also suggests that a linear combination of the two eigenvectors could serve as an order parameter. However, this method does not provide physical information. Hence, we are not able to determine the relationship between these eigenvectors and the physical observables.

For instance, if this same approach is applied to the Ising model, the eigenvector associated to the largest eigenvalue is the magnetization itself (see Ref. (181) and Appendix F). In this case we know that it is the magnetization because we know from different methods that this is a good order parameter as well as its dependence with temperature.

In any case, this approach gives a hint on the question *Is there an order parameter for this phase transition?*.

3.2.4 Discussion

Relying on how and where T_g and T_{LLT} intersect with each other, this new picture of the intermediate phase is potent to explain some of the material features in the experiments. First, depending on the relative strength of the Van der Waals forces, the constraint numbers where T_g and T_{LLT} intersect vary, which leads to different widths and locations of the intermediate phase when changing the chemical compositions (156; 175). Second, as the dynamics have shown to be much less fragile in a liquid with homogeneous structures, the liquid-liquid transition from the high-temperature heterogeneous to low-temperature homogeneous phase implies the dynamics of a liquid in the intermediate phase potentially undergoes a fragile to strong transition under cooling as observed in water (174) and *in-silico* silica (179; 183). Finally, as a byproduct of our theory, the disappearance of heterogeneous phases at very high and very low n may explain the transitions beyond the intermediate phase far from the rigidity threshold (159), as depicted in Fig. 3.11(b).

To test this picture of the intermediate phase experimentally, one could look for direct signals of the liquid-liquid transition, including a lambda peak in the specific heat and loss of structural features

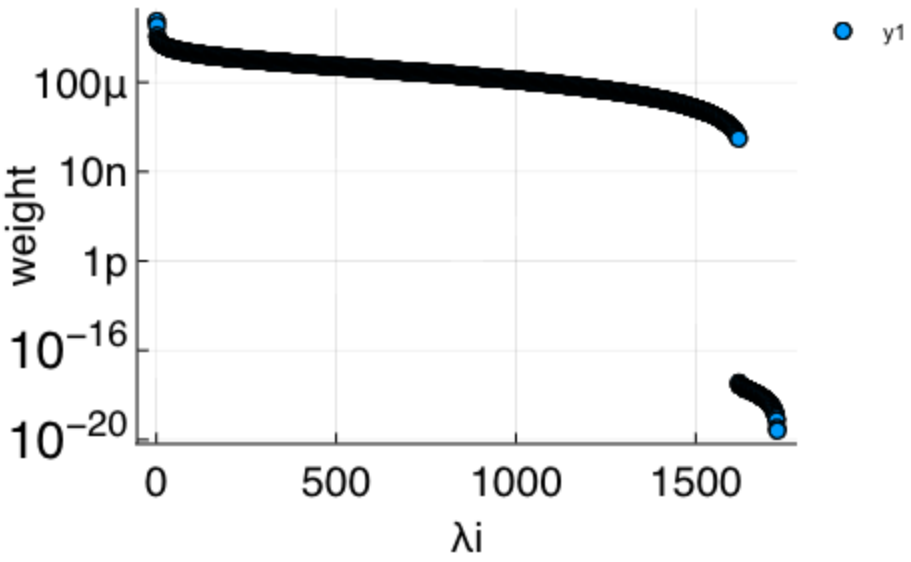

(a)

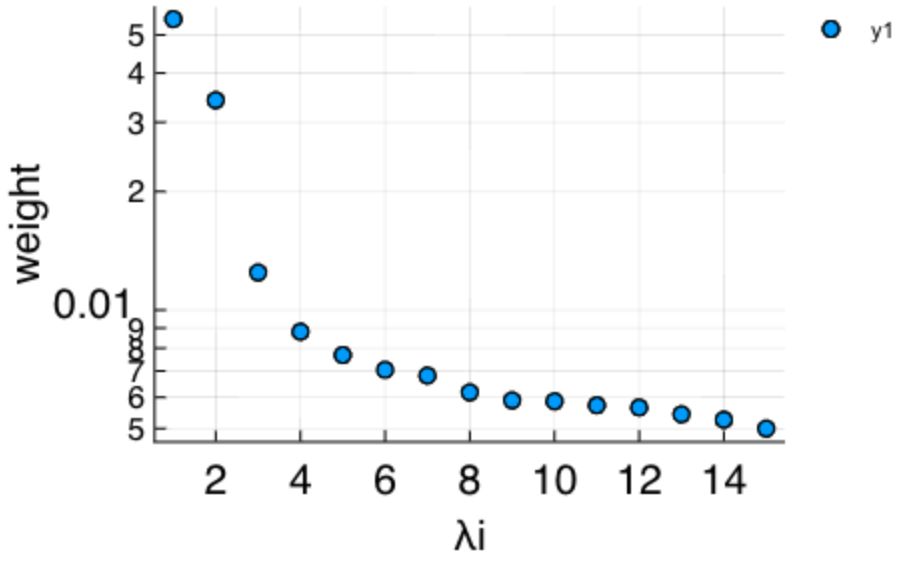

(b)

Figure 3.12: Ranking of the eigenvalues of the covariance matrix of the spring occupation sites in a Linear-Log plot. **a)** All eigenvalues. **b)** First 15 eigenvalues. Notice that there is a jump between the second a third eigenvalue, which means the first to eigenvalues have more weight than the rest.

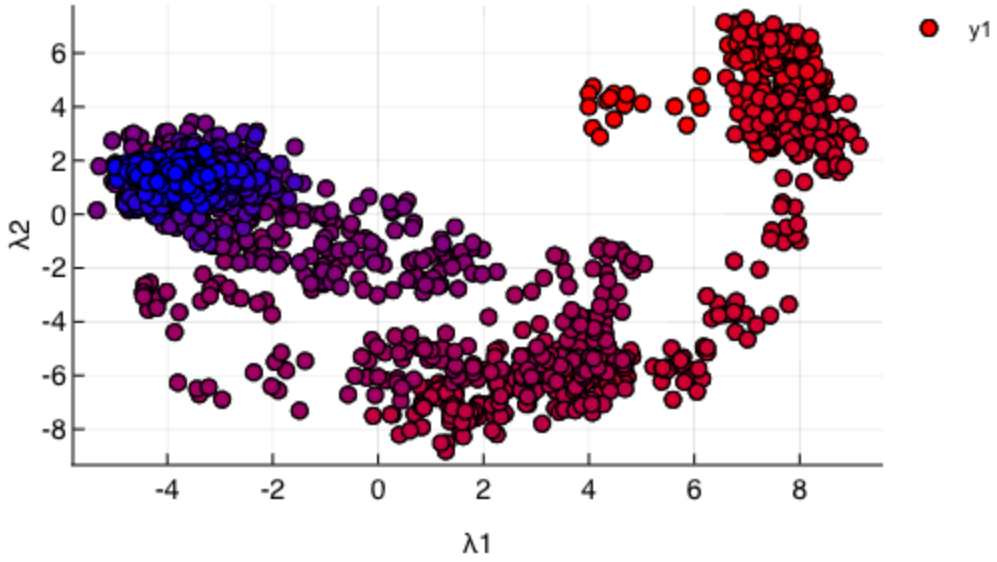

Figure 3.13: First two eigenvectors plotted. The coloring maps the temperature where the highest temperature is colored red and the lowest one is represented by blue. Notice that the upper right corner contains a small cluster which corresponds to the heterogeneous phase transition. The existance a the cluster, i.e., the spatial separation suggests a phase transition.

from the scattering experiments under cooling. The direct evidence should be most likely to be found in compounds close to the boundaries of the intermediate phase, where the liquid-liquid transition temperature is comparable to the glass transition temperature. As the glass transition reflects the dynamic aspect while the liquid-liquid transition reflects the thermodynamic aspect of the material, one could also tune one of the transitions by increasing the cooling rate, or adding a small amount of impurities, or exerting a certain amount of pressure to check if the range of the intermediate phase can be perturbed in a predictable way.

3.3 Conclusions

In conclusion, here we observed that for simple dense fluids near a glass or a crystal phase transition there is a dynamical gap and above a certain critical wavevector, k_c, there are transversal propagating modes although with strong damping. Modes with k below to k_c have zero frequency. This critical k_c goes to zero as a power law with exponent close to 0.8 as the fluid goes into a solid in the vicinity where this phase transition occurs.

In fact, this sole observation opens new avenues for future research. For example, quite recently

it was shown that the hexatic-to-solid phase transition in the case of monodisperse hard-disks, as well as with a small concentration of bidispersity, is a KT transition (115). This was proven on the basis of a prediction made within the KTHNY-theory framework, in which the elastic constant, K, should be zero in the hexatic phase and have a jump to 16π in the solid (184). This elastic constant K may be expressed in terms of the transverse and longitudinal speed of sound denoted as V_t^2 and V_l^2, respectively, which yields

$$K = 4\rho V_t^2 \left(1 - \frac{V_t^2}{V_l^2}\right). \tag{3.26}$$

When k_c goes to zero, shear waves propagate in the system as a whole and the transverse speed of sound changes from zero to some finite value. Hence, in the case of monodisperse hard-disks, we speculate that k_c may serve as an order parameter for the hexatic-to-solid transition.

An even more interesting aspect is that, although the hexatic phase disappears for even a small concentration of small hard-disks , the KT transition should still happen theoretically (184; 115). In this sense, the dynamical-gap may serve as a tool to locate it.

Also, by assuming isotropy of the liquid, one can count zero frequency modes to assign a number of floppy modes to the fluid. Thus, a dynamical average coordination number and a certain number of broken constraints can be defined from this count. Our study suggest that viscoelasticity can serve as a powerful tool to characterize rigidity in the fluid phase.

These floppy modes may appear through vibrational entropy maximization as shown with the elastic network model. This feature is related the fact that the microscopic structure of a network glass undergoes a liquid-liquid transition from an entropy-dominated heterogeneous phase to an energy-dominated homogeneous phase under cooling. At this first-order transition, the specific heat diverges, structural features disappear, and relaxation plateau vanishes. The transition temperature scales as the average frustration energy stored in covalent bonds and varies non-monotonically on the network connectivity. As the glass transition temperature scales positively with the connectivity, the two transition temperatures could cross at two constraint numbers. Inside the two constraint numbers, we would observe the liquid-liquid transition first under cooling and obtain homogeneous network glass at glass transition as in the intermediate phase.

Chapter 4

Conclusions

In this Thesis we have provided an answer on how relaxation and rigidity are related by putting the accent on the floppy modes, namely:

- We showed how vibrational modes are related with relaxation times by means of a simple solvable degenerate two-level system which has a first order transition to a crystal while, under a quench, it presents a dynamical transition to a glass.
- We also showed by means of a non-linear and zero temperature model the relation between vibrational modes and energy barriers. This non-linearities give rise to a wide range of relaxation times, i.e., dynamical heterogeneity.
- We then used viscoelasticity theory to characterized rigidity. Through this theory we used the dynamical gap to characterize rigidity and showed that this may serve as an order parameter for rigidity by testing it in hard disks simulations. Furthermore, it may serve as an order parameter for the KT-transition.
- From the dynamical gap we propose a way to count floppy modes which differs from the local mean field approach in rigidity theory.
- We also showed that when vibrational entropy is maximized, floppy mode domains appear.
- When the coordination number is in a window around the rigidity threshold coordination number, there is a first order phase transition to a homogeneous phase at a fixed temperature.
- We showed that this homogeneous-heterogeneous phase transition is the same as the liquid-liquid transition

The previous points provide a picture to understand the rigidity and relaxation in the case of glass forming systems. The message is that, to understand relaxation in glass forming systems, it's important to study the vibrational modes which contribute to the vibrational entropy. On the other hand, there is in general a competition between internal energy and entropy to minimize the free energy. When this minimization comes from the maximization of vibrational entropy, floppy-mode domains appear. The competition between internal energy and entropy, however, depends on external parameters such as temperature and pressure. All things considered, the vibrational entropy will be maximized provided the coordination number is well-tuned to a value around the rigidity threshold coordination number. Rigidity theory says the coordination number is the important ingredient to characterize rigidity while proposes that it may be tuned by changing concentrations in glass formers. However, when vibrational entropy is maximized, floppy domains appear as well as overconstrained domains, which implies the coexistance of two coordination numbers. In this sense, the tools provided by rigidity theory may fail. Another approach is to use viscoelasticity theory, from which one may use the dynamical gap to characterize rigidity and, furthermore, count the number of floppy modes. The latter is yet to be proven. In this way, one should use this method in real systems, such as chalcogenide glass melts. One may also use the density current correlation function to compute the coordination number.

The glass transition has been the subject of many works for many years, yet a complete understanding is still lacking. Hence, some may say that the glass transition is a dead end. Traditionally, glassy dynamics has been reduced to supercooled liquids. However, for the past few years glassy dynamics has been extended to so many problems and fields, ranging from biology to (lately) machine learning (101; 185). On the other hand, in recent times the importation of tools, such as, dynamical mean field theory or holography has been proposed to understand glassy dynamics (127; 186). It is accurate to say that glass transition is, without doubt, a very busy field where so many ideas converge. A complete glass theory should then be able to shed light on all of these new phenomena in all these different fields. Moreover, as glassy dynamics emerge in different fields, the glass theory gains additional constraints which should ultimately drive research in the correct direction.

Bibliography

[1] G. G. Naumis and R. Kerner, "Stochastic matrix description of glass transition in ternary chalcogenide systems," *Journal of non-crystalline solids*, vol. 231, no. 1, pp. 111–119, 1998.

[2] J. Phillips, "Stretched exponential relaxation in molecular and electronic glasses," *Reports on Progress in Physics*, vol. 59, no. 9, p. 1133, 1996.

[3] R. Kerner and G. G. Naumis, "Stochastic matrix description of the glass transition," *Journal of Physics: Condensed Matter*, vol. 12, no. 8, p. 1641, 2000.

[4] M. Micoulaut and G. Naumis, "Glass transition temperature variation, cross-linking and structure in network glasses: a stochastic approach," *EPL (Europhysics Letters)*, vol. 47, no. 5, p. 568, 1999.

[5] P. E. Ramírez-González, L. López-Flores, H. Acuña-Campa, and M. Medina-Noyola, "Density-temperature-softness scaling of the dynamics of glass-forming soft-sphere liquids," *Physical review letters*, vol. 107, no. 15, p. 155701, 2011.

[6] P. G. Debenedetti, *Metastable liquids: concepts and principles*. Princeton University Press, 1996.

[7] P. G. Debenedetti and F. H. Stillinger, "Supercooled liquids and the glass transition," *Nature*, vol. 410, no. 6825, pp. 259–267, 2001.

[8] F. H. Stillinger, "Supercooled liquids, glass transitions, and the kauzmann paradox," *The Journal of chemical physics*, vol. 88, no. 12, pp. 7818–7825, 1988.

[9] F. H. Stillinger and P. G. Debenedetti, "Energy landscape diversity and supercooled liquid properties," *The Journal of chemical physics*, vol. 116, no. 8, pp. 3353–3361, 2002.

[10] M. M. Smedskjaer, J. C. Mauro, and Y. Yue, "Prediction of glass hardness using temperature-dependent constraint theory," *Physical review letters*, vol. 105, no. 11, p. 115503, 2010.

[11] K. Trachenko, "A stress relaxation approach to glass transition," *Journal of Physics: Condensed Matter*, vol. 18, no. 19, p. L251, 2006.

[12] K. Trachenko, C. Roland, and R. Casalini, "Relationship between the nonexponentiality of relaxation and relaxation time in the problem of glass transition," *The Journal of Physical Chemistry B*, vol. 112, no. 16, pp. 5111–5115, 2008.

[13] J. C. Dyre, "Colloquium: The glass transition and elastic models of glass-forming liquids," *Reviews of modern physics*, vol. 78, no. 3, p. 953, 2006.

[14] G. G. Naumis, "Variation of the glass transition temperature with rigidity and chemical composition," *Physical Review B*, vol. 73, no. 17, p. 172202, 2006.

[15] J. C. Mauro, D. C. Allan, and M. Potuzak, "Nonequilibrium viscosity of glass," *Physical Review B*, vol. 80, no. 9, p. 094204, 2009.

[16] L. Berthier and G. Biroli, "Theoretical perspective on the glass transition and amorphous materials," *Reviews of Modern Physics*, vol. 83, no. 2, p. 587, 2011.

[17] L. Struik, "Orientation effects and cooling stresses in amorphous polymers," *Polymer Engineering & Science*, vol. 18, no. 10, pp. 799–811, 1978.

[18] J. C. Phillips, "Topology of covalent non-crystalline solids i: Short-range order in chalcogenide alloys," *Journal of Non-Crystalline Solids*, vol. 34, no. 2, pp. 153–181, 1979.

[19] H. Aben, J. Anton, M. Õis, K. Viswanathan, S. Chandrasekar, and M. Chaudhri, "On the extraordinary strength of prince rupert's drops," *Applied Physics Letters*, vol. 109, no. 23, p. 231903, 2016.

[20] YAWPITA. Amazing glass blowing art || compilation || 2017. Youtube. [Online]. Available: https://www.youtube.com/watch?v=X7mL8mcPiQ4

[21] D. W. Sandlin. Mystery of prince rupert's drop at 130,000 fps - smarter every day 86. Youtube. [Online]. Available: https://www.youtube.com/watch?v=xe-f4gokRBs

[22] P. G. Wolynes and V. Lubchenko, *Structural Glasses and Supercooled Liquids: Theory, Experiment, and Applications*. John Wiley & Sons, 2012.

[23] H. M. Flores-Ruiz and G. G. Naumis, "Boson peak as a consequence of rigidity: A perturbation theory approach," *Physical Review B*, vol. 83, no. 18, p. 184204, 2011.

[24] H. Tanaka, "Origin of the excess wing and slow β relaxation of glass formers: A unified picture of local orientational fluctuations," *Physical Review E*, vol. 69, no. 2, p. 021502, 2004.

[25] C. A. Angell, "Formation of glasses from liquids and biopolymers," *Science*, vol. 267, no. 5206, pp. 1924–1935, 1995.

[26] P. S. Salmon and A. Zeidler, "Identifying and characterising the different structural length scales in liquids and glasses: an experimental approach," *Physical Chemistry Chemical Physics*, vol. 15, no. 37, pp. 15 286–15 308, 2013.

[27] A. Samarakoon, T. J. Sato, T. Chen, G.-W. Chern, J. Yang, I. Klich, R. Sinclair, H. Zhou, and S.-H. Lee, "Aging, memory, and nonhierarchical energy landscape of spin jam," *Proceedings of the National Academy of Sciences*, vol. 113, no. 42, pp. 11 806–11 810, 2016.

[28] G. Naumis and J. Romero-Arias, "The problem of glass formation and the low frequency vibrational modes anomalies," *Revista mexicana de física*, vol. 56, no. 2, pp. 97–105, 2010.

[29] J. C. Phillips, "Topology of covalent non-crystalline solids i: Short-range order in chalcogenide alloys," *Journal of Non-Crystalline Solids*, vol. 34, no. 2, pp. 153–181, 1979.

[30] M. Thorpe, "Rigidity percolation in glassy structures," *Journal of Non-Crystalline Solids*, vol. 76, no. 1, pp. 109 – 116, 1985.

[31] P. Boolchand, D. Georgiev, and B. Goodman, "Discovery of the intermediate phase in chalcogenide glasses," *Journal of Optoelectronics and Advanced Materials*, vol. 3, no. 3, pp. 703–720, 2001.

[32] P. Boolchand, M. Bauchy, M. Micoulaut, and C. Yildirim, "Topological phases of chalcogenide glasses encoded in the melt dynamics (phys. status solidi b 6/2018)," *physica status solidi (b)*, vol. 255, no. 6, p. 1870122, 2018.

[33] C. Yildirim, J.-Y. Raty, and M. Micoulaut, "Revealing the role of molecular rigidity on the fragility evolution of glass-forming liquids," *Nature communications*, vol. 7, p. 11086, 2016.

[34] M. Micoulaut and Y. Yue, "Material functionalities from molecular rigidity: Maxwell's modern legacy," *Mrs Bulletin*, vol. 42, no. 1, pp. 18–22, 2017.

[35] J. C. Mauro, "Topological constraint theory of glass," *American ceramic society bulletin*, vol. 90, no. 4, p. 31, 2011.

[36] R. Zwanzig, *Nonequilibrium statistical mechanics*. Oxford University Press, USA, 2001.

[37] K. Binder and W. Kob, *Glassy materials and disordered solids: An introduction to their statistical mechanics*. World Scientific, 2011.

[38] G. Naumis and J. Phillips, "Bifurcation of stretched exponential relaxation in microscopically homogeneous glasses," *Journal of Non-Crystalline Solids*, vol. 358, no. 5, pp. 893–897, 2012.

[39] M. Born, *Is Classical Mechanics in Fact Deterministic?* New York, NY: Springer New York, 1968, pp. 78–83. [Online]. Available: https://doi.org/10.1007/978-1-4615-7587-0_7

[40] M. F. Shlesinger, G. M. Zaslavsky, and J. Klafter, "Strange kinetics," *Nature*, vol. 363, no. 6424, pp. 31–37, 1993.

[41] A. Diaz-Ruelas, H. J. Jensen, D. Piovani, and A. Robledo, "Relating high dimensional stochastic complex systems to low-dimensional intermittency," *The European Physical Journal Special Topics*, vol. 226, no. 3, pp. 341–351, 2017.

[42] I. Fermi, P. Pasta, S. Ulam, and M. Tsingou, "Studies of the nonlinear problems," Los Alamos Scientific Lab., N. Mex., Tech. Rep., 1955.

[43] A. Ponno, "The fermi-pasta-ulam problem in the thermodynamic limit," in *Chaotic Dynamics and Transport in Classical and Quantum Systems*. Springer, 2005, pp. 431–440.

[44] J. Ford, "Equipartition of energy for nonlinear systems," *Journal of Mathematical Physics*, vol. 2, no. 3, pp. 387–393, 1961.

[45] U. R. Pedersen, L. Costigliola, N. P. Bailey, T. B. Schrøder, and J. C. Dyre, "Thermodynamics of freezing and melting," *Nature communications*, vol. 7, p. 12386, 2016.

[46] S. Albert, T. Bauer, M. Michl, G. Biroli, J.-P. Bouchaud, A. Loidl, P. Lunkenheimer, R. Tourbot, C. Wiertel-Gasquet, and F. Ladieu, "Fifth-order susceptibility unveils growth of thermodynamic amorphous order in glass-formers," *Science*, vol. 352, no. 6291, pp. 1308–1311, 2016.

[47] H. W. Hansen, B. Frick, T. Hecksher, J. C. Dyre, and K. Niss, "Connection between fragility, mean-squared displacement, and shear modulus in two van der waals bonded glass-forming liquids," *Physical Review B*, vol. 95, no. 10, p. 104202, 2017.

[48] T. Gleim and W. Kob, "The-relaxation dynamics of a simple liquid," *The European Physical Journal B-Condensed Matter and Complex Systems*, vol. 13, no. 1, pp. 83–86, 2000.

[49] M. Mezard and G. Parisi, "Glasses and replicas," *Structural Glasses and Supercooled Liquids: Theory, Experiment, and Applications*, pp. 151–191, 2012.

[50] K. Trachenko and V. Brazhkin, "Heat capacity at the glass transition," *Physical Review B*, vol. 83, no. 1, p. 014201, 2011.

[51] A. Ninarello, L. Berthier, and D. Coslovich, "Models and algorithms for the next generation of glass transition studies," *Physical Review X*, vol. 7, no. 2, p. 021039, 2017.

[52] M. Thorpe, "Continuous deformations in random networks," *Journal of Non-Crystalline Solids*, vol. 57, no. 3, pp. 355–370, 1983.

[53] A. Huerta and G. Naumis, "Relationship between glass transition and rigidity in a binary associative fluid," *Physics Letters A*, vol. 299, no. 5, pp. 660–665, 2002.

[54] A. Huerta and G. G. Naumis, "Evidence of a glass transition induced by rigidity self-organization in a network-forming fluid," *Physical Review B*, vol. 66, no. 18, p. 184204, 2002.

[55] H. M. Flores-Ruiz and G. G. Naumis, "Mean-square-displacement distribution in crystals and glasses: An analysis of the intrabasin dynamics," *Physical Review E*, vol. 85, no. 4, p. 041503, 2012.

[56] E. Lerner, G. Düring, and E. Bouchbinder, "Statistics and properties of low-frequency vibrational modes in structural glasses," *Physical review letters*, vol. 117, no. 3, p. 035501, 2016.

[57] E. Lerner and E. Bouchbinder, "Effect of instantaneous and continuous quenches on the density of vibrational modes in model glasses," *Physical Review E*, vol. 96, no. 2, p. 020104, 2017.

[58] G. G. Naumis, "Energy landscape and rigidity," *Physical Review E*, vol. 71, no. 2, p. 026114, 2005.

[59] ——, "Simple solvable energy-landscape model that shows a thermodynamic phase transition and a glass transition," *Physical Review E*, vol. 85, no. 6, p. 061505, 2012.

[60] H. M. Flores-Ruiz, G. G. Naumis, and J. Phillips, "Heating through the glass transition: A rigidity approach to the boson peak," *Physical Review B*, vol. 82, no. 21, p. 214201, 2010.

[61] J. Q. Toledo-Marín, I. P. Castillo, and G. G. Naumis, "Minimal cooling speed for glass transition in a simple solvable energy landscape model," *Physica A: Statistical Mechanics and its Applications*, vol. 451, pp. 227–236, 2016.

[62] J. Q. Toledo-Marín and G. G. Naumis, "Short time dynamics determine glass forming ability in a glass transition two-level model: A stochastic approach using kramers' escape formula," *The Journal of Chemical Physics*, vol. 146, no. 9, p. 094506, 2017.

[63] A. Ponno, "Chaotic dynamics and transport in classical and quantum systems, vol. 182," 2005.

[64] J. Romero-Arias, F. Salazar, G. Naumis, and G. Fernandez-Anaya, "Thermal conductivity, relaxation and low-frequency vibrational mode anomalies in glasses: a model using the fermi–pasta–ulam nonlinear hamiltonian," *Philosophical Transactions of the Royal Society of London A: Mathematical, Physical and Engineering Sciences*, vol. 367, no. 1901, pp. 3173–3181, 2009.

[65] J. Romero-Arias and G. G. Naumis, "Thermal relaxation and low-frequency vibrational anomalies in simple models of glasses: A study using nonlinear hamiltonians," *Physical Review E*, vol. 77, no. 6, p. 061504, 2008.

[66] M. Onorato, L. Vozella, D. Proment, and Y. V. Lvov, "Route to thermalization in the α-fermi–pasta–ulam system," *Proceedings of the National Academy of Sciences*, vol. 112, no. 14, pp. 4208–4213, 2015.

[67] I. Limas, G. Naumis, F. Salazar, and C. Wang, "Efficient anharmonic phonon generation using a quasiperiodic lattice," *Physics Letters A*, vol. 337, no. 1, pp. 141 – 146, 2005. [Online]. Available: http://www.sciencedirect.com/science/article/pii/S0375960105001477

[68] G. G. Naumis, "Use of the trace map for evaluating localization properties," *Phys. Rev. B*, vol. 59, pp. 11 315–11 321, May 1999. [Online]. Available: https://link.aps.org/doi/10.1103/PhysRevB.59.11315

[69] M. Henon and C. Heiles, "The applicability of the third integral of motion: some numerical experiments," *The Astronomical Journal*, vol. 69, p. 73, 1964.

[70] A. P. Fordy, "The hénon-heiles system revisited," *Physica D: Nonlinear Phenomena*, vol. 52, no. 2-3, pp. 204–210, 1991.

[71] J. Aguirre, J. C. Vallejo, and M. A. Sanjuán, "Wada basins and chaotic invariant sets in the hénon-heiles system," *Physical Review E*, vol. 64, no. 6, p. 066208, 2001.

[72] B. A. Waite and W. H. Miller, "Mode specificity in unimolecular reaction dynamics: The henon–heiles potential energy surface," *The Journal of Chemical Physics*, vol. 74, no. 7, pp. 3910–3915, 1981.

[73] M. Toda, *Theory of nonlinear lattices*. Springer Science & Business Media, 2012, vol. 20.

[74] H. Zhao and M. Du, "Threshold law for escaping from the henon-heiles system," *Physical Review E*, vol. 76, no. 2, p. 027201, 2007.

[75] D. Wales, *Energy landscapes: Applications to clusters, biomolecules and glasses*. Cambridge University Press, 2003.

[76] W. Bauer and G. Bertsch, "Decay of ordered and chaotic systems," *Physical review letters*, vol. 65, no. 18, p. 2213, 1990.

[77] P. Hänggi, P. Talkner, and M. Borkovec, "Reaction-rate theory: fifty years after kramers," *Reviews of modern physics*, vol. 62, no. 2, p. 251, 1990.

[78] W. Coffey, Y. P. Kalmykov, and J. Waldron, *With Applications to Stochastic Problems in Physics, Chemistry and Electrical Engineering 2nd Edition*. World Scientific, 2004.

[79] S. Sastry, "The relationship between fragility, configurational entropy and the potential energy landscape of glass-forming liquids," *Nature*, vol. 409, no. 6817, pp. 164–167, 2001.

[80] T. F. Middleton and D. J. Wales, "Energy landscapes of some model glass formers," *Physical Review B*, vol. 64, no. 2, p. 024205, 2001.

[81] B. Doliwa and A. Heuer, "Energy barriers and activated dynamics in a supercooled lennard-jones liquid," *Physical Review E*, vol. 67, no. 3, p. 031506, 2003.

[82] K. Broderix, K. K. Bhattacharya, A. Cavagna, A. Zippelius, and I. Giardina, "Energy landscape of a lennard-jones liquid: statistics of stationary points," *Physical review letters*, vol. 85, no. 25, p. 5360, 2000.

[83] D. J. Wales, "A microscopic basis for the global appearance of energy landscapes," *Science*, vol. 293, no. 5537, pp. 2067–2070, 2001.

[84] H. W. Hansen, B. Frick, S. Capaccioli, T. Hecksher, J. C. Dyre, and K. Niss, "Connection between fragility, mean-squared displacement and shear modulus in two van der waals bonded glass-forming liquids," *arXiv preprint arXiv:1611.01748*, 2016.

[85] D. J. Wales, J. P. Doye, M. A. Miller, P. N. Mortenson, and T. R. Walsh, "Energy landscapes: from clusters to biomolecules," *Advances in Chemical Physics*, vol. 115, pp. 1–112, 2000.

[86] F. H. Stillinger, "Exponential multiplicity of inherent structures," *Physical Review E*, vol. 59, no. 1, p. 48, 1999.

[87] S. A. Langer, A. T. Dorsey, and J. P. Sethna, "Entropy distribution of a two-level system: An asymptotic analysis," *Physical Review B*, vol. 40, no. 1, p. 345, 1989.

[88] S. Redner, *A guide to first-passage processes*. Cambridge University Press, 2001.

[89] V. Mel'nikov and S. Meshkov, "Theory of activated rate processes: exact solution of the kramers problem," *The Journal of chemical physics*, vol. 85, no. 2, pp. 1018–1027, 1986.

[90] P. K. Gupta and J. C. Mauro, "Composition dependence of glass transition temperature and fragility. i. a topological model incorporating temperature-dependent constraints," *The Journal of Chemical Physics*, vol. 130, no. 9, p. 094503, 2009. [Online]. Available: https://doi.org/10.1063/1.3077168

[91] R. Landauer and J. Swanson, "Frequency factors in the thermally activated process," *Physical Review*, vol. 121, no. 6, p. 1668, 1961.

[92] R. Metzler and J. Klafter, "The random walk's guide to anomalous diffusion: a fractional dynamics approach," *Physics reports*, vol. 339, no. 1, pp. 1–77, 2000.

[93] K. Ngai, *Relaxation and diffusion in complex systems*. Springer Science & Business Media, 2011.

[94] Y. Liu, T. Fujita, D. Aji, M. Matsuura, and M. Chen, "Structural origins of johari-goldstein relaxation in a metallic glass," *Nature communications*, vol. 5, p. 3238, 2014.

[95] H. B. Yu, W. H. Wang, H. Y. Bai, and K. Samwer, "The β-relaxation in metallic glasses," *National Science Review*, vol. 1, no. 3, pp. 429–461, 2014.

[96] G. Diezemann, "A free-energy landscape model for primary relaxation in glass-forming liquids: Rotations and dynamic heterogeneities," *The Journal of chemical physics*, vol. 107, no. 23, pp. 10 112–10 120, 1997.

[97] G. Johari, "Localized molecular motions of β-relaxation and its energy landscape," *Journal of non-crystalline solids*, vol. 307, pp. 317–325, 2002.

[98] M. Vogel and E. Rössler, "On the nature of slow β-process in simple glass formers: a 2h nmr study," *The Journal of Physical Chemistry B*, vol. 104, no. 18, pp. 4285–4287, 2000.

[99] G. G. Naumis and G. Cocho, "The tails of rank-size distributions due to multiplicative processes: from power laws to stretched exponentials and beta-like functions," *New Journal of Physics*, vol. 9, no. 8, p. 286, 2007. [Online]. Available: http://stacks.iop.org/1367-2630/9/i=8/a=286

[100] A. Prados, J. Brey, and B. Sánchez-Rey, "A dynamical monte carlo algorithm for master equations with time-dependent transition rates," *Journal of statistical physics*, vol. 89, no. 3-4, pp. 709–734, 1997.

[101] D. Bi, X. Yang, M. C. Marchetti, and M. L. Manning, "Motility-driven glass and jamming transitions in biological tissues," *Physical Review X*, vol. 6, no. 2, p. 021011, 2016.

[102] A. Huerta and G. G. Naumis, "Role of rigidity in the fluid-solid transition," *Phys. Rev. Lett.*, vol. 90, p. 145701, Apr 2003. [Online]. Available: https://link.aps.org/doi/10.1103/PhysRevLett.90.145701

[103] A. Huerta, G. G. Naumis, D. T. Wasan, D. Henderson, and A. Trokhymchuk, "Attraction-driven disorder in a hard-core colloidal monolayer," *The Journal of Chemical Physics*, vol. 120, no. 3, pp. 1506–1510, 2004. [Online]. Available: https://doi.org/10.1063/1.1632893

[104] L. Yan, "Entropy favors heterogeneous structures of networks near the rigidity threshold," *Nature communications*, vol. 9, no. 1, p. 1359, 2018.

[105] H. M. Flores-Ruiz and G. G. Naumis, "Excess of low frequency vibrational modes and glass transition: A molecular dynamics study for soft spheres at constant pressure," *The Journal of Chemical Physics*, vol. 131, no. 15, p. 154501, 2009. [Online]. Available: https://doi.org/10.1063/1.3246805

[106] H. M. Flores-Ruiz, G. G. Naumis, and J. C. Phillips, "Heating through the glass transition: A rigidity approach to the boson peak," *Phys. Rev. B*, vol. 82, p. 214201, Dec 2010. [Online]. Available: https://link.aps.org/doi/10.1103/PhysRevB.82.214201

[107] H. M. Flores-Ruiz and G. G. Naumis, "Boson peak as a consequence of rigidity: A perturbation theory approach," *Phys. Rev. B*, vol. 83, p. 184204, May 2011. [Online]. Available: https://link.aps.org/doi/10.1103/PhysRevB.83.184204

[108] M. Bauchy and M. Micoulaut, "Atomic scale foundation of temperature-dependent bonding constraints in network glasses and liquids," *Journal of Non-Crystalline Solids*, vol. 357, no. 14, pp. 2530–2537, 2011.

[109] D. Selvanathan, W. Bresser, and P. Boolchand, "Stiffness transitions in si x se 1- x glasses from raman scattering and temperature-modulated differential scanning calorimetry," *Physical Review B*, vol. 61, no. 22, p. 15061, 2000.

[110] K. Gunasekera, S. Bhosle, P. Boolchand, and M. Micoulaut, "Superstrong nature of covalently bonded glass-forming liquids at select compositions," *The Journal of chemical physics*, vol. 139, no. 16, p. 164511, 2013.

[111] P. M. Chaikin and T. C. Lubensky, *Principles of Condensed Matter Physics*. Cambridge: Cambridge University Press, 1995.

[112] D. Bi, J. Lopez, J. M. Schwarz, and M. L. Manning, "A density-independent rigidity transition in biological tissues," *Nature Physics*, vol. 11, no. 12, p. 1074, 2015.

[113] L. Atia, D. Bi, Y. Sharma, J. A. Mitchel, B. Gweon, S. A. Koehler, S. J. DeCamp, B. Lan, J. H. Kim, R. Hirsch *et al.*, "Geometric constraints during epithelial jamming," *Nature physics*, vol. 14, no. 6, p. 613, 2018.

[114] J. P. Boon and S. Yip, *Molecular hydrodynamics*. Courier Corporation, 1991.

[115] J. Russo and N. B. Wilding, "Disappearance of the hexatic phase in a binary mixture of hard disks," *Physical review letters*, vol. 119, no. 11, p. 115702, 2017.

[116] M. Engel, J. A. Anderson, S. C. Glotzer, M. Isobe, E. P. Bernard, and W. Krauth, "Hard-disk equation of state: First-order liquid-hexatic transition in two dimensions with three simulation methods," *Physical Review E*, vol. 87, no. 4, p. 042134, 2013.

[117] M. Isobe, "Hard sphere simulation in statistical physics methodologies and applications," *Molecular Simulation*, vol. 42, no. 16, pp. 1317–1329, 2016.

[118] J. Russo, F. Romano, and H. Tanaka, "Glass forming ability in systems with competing orderings," *Physical Review X*, vol. 8, no. 2, p. 021040, 2018.

[119] E. Flenner and G. Szamel, "Fundamental differences between glassy dynamics in two and three dimensions," *Nature communications*, vol. 6, p. 7392, 2015.

[120] H. Shiba, Y. Yamada, T. Kawasaki, and K. Kim, "Unveiling dimensionality dependence of glassy dynamics: 2d infinite fluctuation eclipses inherent structural relaxation," *Physical review letters*, vol. 117, no. 24, p. 245701, 2016.

[121] B. Illing, S. Fritschi, H. Kaiser, C. L. Klix, G. Maret, and P. Keim, "Mermin–wagner fluctuations in 2d amorphous solids," *Proceedings of the National Academy of Sciences*, vol. 114, no. 8, pp. 1856–1861, 2017.

[122] H. Weber, D. Marx, and K. Binder, "Melting transition in two dimensions: A finite-size scaling analysis of bond-orientational order in hard disks," *Physical Review B*, vol. 51, no. 20, p. 14636, 1995.

[123] M. N. Bannerman, R. Sargant, and L. Lue, "Dynamo: a free \calo (n) general event-driven molecular dynamics simulator," *Journal of computational chemistry*, vol. 32, no. 15, pp. 3329–3338, 2011.

[124] M. Skoge, A. Donev, F. H. Stillinger, and S. Torquato, "Packing hyperspheres in high-dimensional euclidean spaces," *Physical Review E*, vol. 74, no. 4, p. 041127, 2006.

[125] M. P. Allen and D. J. Tildesley, *Computer simulation of liquids*. Oxford university press, 2017.

[126] K. Trachenko and V. Brazhkin, "Collective modes and thermodynamics of the liquid state," *Reports on Progress in Physics*, vol. 79, no. 1, p. 016502, 2015.

[127] M. Baggioli, V. Brazhkin, K. Trachenko, and M. Vasin, "Gapped momentum states," *arXiv preprint arXiv:1904.01419*, 2019.

[128] M. Baggioli and K. Trachenko, "Maxwell interpolation and close similarities between liquids and holographic models," *arXiv preprint arXiv:1808.05391*, 2018.

[129] ——, "Solidity of liquids: How holography knows it," *arXiv preprint arXiv:1807.10530*, 2018.

[130] J. Q. Toledo-Marín and G. G. Naumis, "To be published," 2019.

[131] C. Yang, M. Dove, V. Brazhkin, and K. Trachenko, "Emergence and evolution of the k gap in spectra of liquid and supercritical states," *Physical review letters*, vol. 118, no. 21, p. 215502, 2017.

[132] D. Frenkel, "Order through entropy," *Nature materials*, vol. 14, no. 1, p. 9, 2014.

[133] S. Glasstone, H. Eyring, and K. J. Laidler, *The theory of rate processes*. McGraw-Hill, 1941.

[134] J. Q. Toledo-Marín and G. G. Naumis, "Escape time, relaxation, and sticky states of a softened henon-heiles model: Low-frequency vibrational mode effects and glass relaxation," *Physical Review E*, vol. 97, no. 4, p. 042106, 2018.

[135] M. Wyart, "On the rigidity of amorphous solids. price fluctuations, conventions and microstructure of financial markets," Ph.D. dissertation, Ecole Polytechnique X, 2005.

[136] Y. Katayama, T. Mizutani, W. Utsumi, O. Shimomura, M. Yamakata, and K.-i. Funakoshi, "A first-order liquid–liquid phase transition in phosphorus," *Nature*, vol. 403, no. 6766, p. 170, 2000.

[137] H. Tanaka, R. Kurita, and H. Mataki, "Liquid-liquid transition in the molecular liquid triphenyl phosphite," *Physical review letters*, vol. 92, no. 2, p. 025701, 2004.

[138] V. V. Vasisht, S. Saw, and S. Sastry, "Liquid–liquid critical point in supercooled silicon," *Nature Physics*, vol. 7, no. 7, p. 549, 2011.

[139] S. Wei, F. Yang, J. Bednarcik, I. Kaban, O. Shuleshova, A. Meyer, and R. Busch, "Liquid–liquid transition in a strong bulk metallic glass-forming liquid," *Nature communications*, vol. 4, p. 2083, 2013.

[140] A. Cadien, Q. Hu, Y. Meng, Y. Cheng, M. Chen, J. Shu, H. Mao, and H. Sheng, "First-order liquid-liquid phase transition in cerium," *Physical review letters*, vol. 110, no. 12, p. 125503, 2013.

[141] X. Zhao, C. Wang, H. Zheng, Z. Tian, and L. Hu, "The role of liquid–liquid transition in glass formation of cuzr alloys," *Physical Chemistry Chemical Physics*, vol. 19, no. 24, pp. 15 962–15 972, 2017.

[142] P. H. Poole, F. Sciortino, U. Essmann, and H. E. Stanley, "Phase behaviour of metastable water," *Nature*, vol. 360, no. 6402, p. 324, 1992.

[143] O. Mishima and H. E. Stanley, "The relationship between liquid, supercooled and glassy water," *Nature*, vol. 396, no. 6709, p. 329, 1998.

[144] V. Holten and M. Anisimov, "Entropy-driven liquid–liquid separation in supercooled water," *Scientific reports*, vol. 2, p. 713, 2012.

[145] J. C. Palmer, F. Martelli, Y. Liu, R. Car, A. Z. Panagiotopoulos, and P. G. Debenedetti, "Metastable liquid–liquid transition in a molecular model of water," *Nature*, vol. 510, no. 7505, p. 385, 2014.

[146] M. Kobayashi and H. Tanaka, "The reversibility and first-order nature of liquid–liquid transition in a molecular liquid," *Nature communications*, vol. 7, p. 13438, 2016.

[147] S. Woutersen, B. Ensing, M. Hilbers, Z. Zhao, and C. A. Angell, "A liquid-liquid transition in supercooled aqueous solution related to the hda-lda transition," *Science*, vol. 359, no. 6380, pp. 1127–1131, 2018.

[148] J. C. Palmer, P. H. Poole, F. Sciortino, and P. G. Debenedetti, "Advances in computational studies of the liquid–liquid transition in water and water-like models," *Chemical reviews*, vol. 118, no. 18, pp. 9129–9151, 2018.

[149] J. A. Sellberg, C. Huang, T. A. McQueen, N. Loh, H. Laksmono, D. Schlesinger, R. Sierra, D. Nordlund, C. Hampton, D. Starodub *et al.*, "Ultrafast x-ray probing of water structure below the homogeneous ice nucleation temperature," *Nature*, vol. 510, no. 7505, p. 381, 2014.

[150] G. G. Naumis, "Energy landscape and rigidity," *Physical Review E*, vol. 71, no. 2, p. 026114, 2005.

[151] J. Maxwell, "On the calculation of the equilibrium and stiffness of frames," *Philos. Mag.*, vol. 27, no. 5755, pp. 294–299, 1864.

[152] R. W. Hall and P. G. Wolynes, "Microscopic theory of network glasses," *Phys. Rev. Lett.*, vol. 90, p. 085505, Feb 2003. [Online]. Available: http://link.aps.org/doi/10.1103/PhysRevLett.90.085505

[153] H. Shintani and H. Tanaka, "Universal link between the boson peak and transverse phonons in glass," *Nat Mater*, vol. 7, pp. 870–877, Nov 2008. [Online]. Available: http://www.nature.com/nmat/journal/v7/n11/suppinfo/nmat2293_S1.html

[154] J. C. Mauro, D. C. Allan, and M. Potuzak, "Nonequilibrium viscosity of glass," *Physical Review B*, vol. 80, no. 9, p. 094204, 2009.

[155] L. Yan, G. Düring, and M. Wyart, "Why glass elasticity affects the thermodynamics and fragility of supercooled liquids," *Proceedings of the National Academy of Sciences*, vol. 110, no. 16, pp. 6307–6312, 2013.

[156] P. Boolchand, D. Georgiev, and B. Goodman, "Discovery of the intermediate phase in chalcogenide glasses," *Journal of Optoelectronics and Advanced Materials*, vol. 3, no. 3, pp. 703–720, 2001.

[157] F. Wang, S. Mamedov, P. Boolchand, B. Goodman, and M. Chandrasekhar, "Pressure raman effects and internal stress in network glasses," *Phys. Rev. B*, vol. 71, p. 174201, May 2005. [Online]. Available: http://link.aps.org/doi/10.1103/PhysRevB.71.174201

[158] K. Rompicharla, D. I. Novita, P. Chen, P. Boolchand, M. Micoulaut, and W. Huff, "Abrupt boundaries of intermediate phases and space filling in oxide glasses," *Journal of Physics: Condensed Matter*, vol. 20, no. 20, p. 202101, 2008. [Online]. Available: http://stacks.iop.org/0953-8984/20/i=20/a=202101

[159] S. Bhosle, K. Gunasekera, P. Boolchand, and M. Micoulaut, "Melt homogenization and self-organization in chalcogenides-part ii," *International Journal of Applied Glass Science*, vol. 3, no. 3, pp. 205–220, 2012. [Online]. Available: http://dx.doi.org/10.1111/j.2041-1294.2012.00092.x

[160] D. J. Jacobs and M. F. Thorpe, "Generic rigidity percolation: The pebble game," *Phys. Rev. Lett.*, vol. 75, pp. 4051–4054, Nov 1995. [Online]. Available: http://link.aps.org/doi/10.1103/PhysRevLett.75.4051

[161] ——, "Generic rigidity percolation in two dimensions," *Phys. Rev. E*, vol. 53, pp. 3682–3693, Apr 1996. [Online]. Available: http://link.aps.org/doi/10.1103/PhysRevE.53.3682

[162] J. Barré, A. R. Bishop, T. Lookman, and A. Saxena, "Adaptability and "intermediate phase" in randomly connected networks," *Phys. Rev. Lett.*, vol. 94, p. 208701, May 2005. [Online]. Available: http://link.aps.org/doi/10.1103/PhysRevLett.94.208701

[163] M. Thorpe, D. Jacobs, M. Chubynsky, and J. Phillips, "Self-organization in network glasses," *Journal of Non-Crystalline Solids*, vol. 266-269, Part 2, no. 0, pp. 859 – 866, 2000. [Online]. Available: http://www.sciencedirect.com/science/article/pii/S002230939900856X

[164] M. V. Chubynsky, M.-A. Brière, and N. Mousseau, "Self-organization with equilibration: A model for the intermediate phase in rigidity percolation," *Phys. Rev. E*, vol. 74, p. 016116, Jul 2006. [Online]. Available: http://link.aps.org/doi/10.1103/PhysRevE.74.016116

[165] L. Yan and M. Wyart, "Evolution of covalent networks under cooling: Contrasting the rigidity window and jamming scenarios," *Phys. Rev. Lett.*, vol. 113, p. 215504, Nov 2014. [Online]. Available: http://link.aps.org/doi/10.1103/PhysRevLett.113.215504

[166] K. A. Kirchner and J. C. Mauro, "Statistical mechanical model of the self-organized intermediate phase in glass-forming systems with adaptable network topologies," *Frontiers in Materials*, vol. 6, p. 11, 2019.

[167] M.-A. Brière, M. V. Chubynsky, and N. Mousseau, "Self-organized criticality in the intermediate phase of rigidity percolation," *Phys. Rev. E*, vol. 75, p. 056108, May 2007. [Online]. Available: http://link.aps.org/doi/10.1103/PhysRevE.75.056108

[168] M. Micoulaut and M. Bauchy, "Anomalies of the first sharp diffraction peak in network glasses: Evidence for correlations with dynamic and rigidity properties," *physica status solidi (b)*, vol. 250, no. 5, pp. 976–982, 2013. [Online]. Available: http://dx.doi.org/10.1002/pssb.201248512

[169] M. Bauchy, A. Kachmar, and M. Micoulaut, "Structural, dynamic, electronic, and vibrational properties of flexible, intermediate, and stressed rigid as-se glasses and liquids from first principles molecular dynamics," *The Journal of chemical physics*, vol. 141, no. 19, p. 194506, 2014.

[170] M. Bauchy and M. Micoulaut, "Densified network glasses and liquids with thermodynamically reversible and structurally adaptive behaviour," *Nature communications*, vol. 6, 2015.

[171] C. Yildirim, J.-Y. Raty, and M. Micoulaut, "Decoding entangled transitions: Polyamorphism and stressed rigidity," *The Journal of chemical physics*, vol. 148, no. 24, p. 244505, 2018.

[172] C. A. Angell, "Insights into phases of liquid water from study of its unusual glass-forming properties," *Science*, vol. 319, no. 5863, pp. 582–587, 2008.

[173] S. Wei, I. Gallino, R. Busch, and C. A. Angell, "Glass transition with decreasing correlation length during cooling of fe 50 co 50 superlattice and strong liquids," *Nature Physics*, vol. 7, no. 2, p. 178, 2011.

[174] C. A. Angell, "Heat capacity and entropy functions in strong and fragile glass-formers, relative to those of disordering crystalline materials," in *Glassy, amorphous and nano-crystalline materials*. Springer, 2011, pp. 21–40.

[175] L. Yan, "Entropy favors heterogeneous structures of networks near the rigidity threshold," *Nature communications*, vol. 9, no. 1, p. 1359, 2018.

[176] L. Yan and M. Wyart, "Adaptive elastic networks as models of supercooled liquids," *Physical Review E*, vol. 92, no. 2, p. 022310, 2015.

[177] M. Newman and G. Barkema, *Monte carlo methods in statistical physics chapter 1-4*. Oxford University Press: New York, USA, 1999.

[178] R. Brueckner, "Properties and structure of vitreous silica. i," *Journal of non-crystalline solids*, vol. 5, no. 2, pp. 123–175, 1970.

[179] J. Horbach and W. Kob, "Static and dynamic properties of a viscous silica melt," *Physical Review B*, vol. 60, no. 5, p. 3169, 1999.

[180] P. Jutzi and U. Schubert, *Silicon chemistry: from the atom to extended systems*. John Wiley & Sons, 2007.

[181] L. Wang, "Discovering phase transitions with unsupervised learning," *Physical Review B*, vol. 94, no. 19, p. 195105, 2016.

[182] I. Goodfellow, Y. Bengio, and A. Courville, *Deep learning*. MIT press, 2016.

[183] S. Sastry and C. A. Angell, "Liquid–liquid phase transition in supercooled silicon," *Nature materials*, vol. 2, no. 11, p. 739, 2003.

[184] K. J. Strandburg, "Two-dimensional melting," *Reviews of modern physics*, vol. 60, no. 1, p. 161, 1988.

[185] S. Spigler, M. Geiger, S. d'Ascoli, L. Sagun, G. Biroli, and M. Wyart, "A jamming transition from under-to over-parametrization affects generalization in deep learning," *Journal of Physics A: Mathematical and Theoretical*, vol. 52, no. 47, p. 474001, 2019.

[186] D. Facoetti, G. Biroli, J. Kurchan, and D. R. Reichman, "Classical glasses, black holes, and strange quantum liquids," *arXiv preprint arXiv:1906.09228*, 2019.

[187] U. Balucani and M. Zoppi, *Dynamics of the liquid state*. Clarendon Press, 1995, vol. 10.

[188] C. Calladine, "Buckminster fuller's "tensegrity" structures and clerk maxwell's rules for the construction of stiff frames," *International Journal of Solids and Structures*, vol. 14, no. 2, pp. 161–172, 1978.

[189] M. Newman and G. Barkema, *Monte carlo methods in statistical physics chapter 1-4*. Oxford University Press: New York, USA, 1999.

[190] U. Wolff, "Collective monte carlo updating for spin systems," *Physical Review Letters*, vol. 62, no. 4, p. 361, 1989.

Appendix A

First passage time and transition rate (Kramer)

The Kramer problem is to find the rate at which a Brownian particle escapes from a potential well over a potential barrier. One way to tackle this is through mean of the first passage time theory. Let us recall this by assuming we have the following problem:

$$\begin{cases} \frac{\partial c(\mathbf{r},t)}{\partial t} = \mathscr{D} c(\mathbf{r},t) \\ c(\mathbf{a},0) = \delta(\mathbf{a}-\mathbf{a_0}) \ , \ \forall \mathbf{a} \in V \\ c(\mathbf{a},t) = 0 \ , \ \forall \mathbf{a} \in \partial V \ , \end{cases} \tag{A.1}$$

where $\mathscr{D}$ is an operator (which we already assume it corresponds to the Smoluchowsky Diffusion Eq.). The formal operator solution as an initial value problem is

$$c(\mathbf{a},t) = e^{t\mathscr{D}} \delta(\mathbf{a}-\mathbf{a_0}) \ . \tag{A.2}$$

Now, the survival probability is defined as

$$S(t,\mathbf{a_0}) = \int_V d\mathbf{a} c(\mathbf{a},t) \ , \tag{A.3}$$

which for long times is zero. Now, we may define the first passage probability $f(t,\mathbf{a_0})$ as through means of the survival probability, i.e.,

$$S(t,\mathbf{a}) = 1 - \int_0^t dt' f(t',\mathbf{a_0}) \ . \tag{A.4}$$

Hence, differentiating the last Eq. with respect to t, we obtain

$$f(t,\mathbf{a_0}) = -\frac{dS(\mathbf{a_0},t)}{dt} \ . \tag{A.5}$$

The mean first passage time is the first moment of t,

$$\begin{aligned}
\tau(\mathbf{a_0}) &= \int_0^\infty dt\, t f(t,\mathbf{a_0}) \\
&= -\int_0^\infty dt\, t \frac{dS(\mathbf{a_0},t)}{dt} \\
&= \int_0^\infty dt S(\mathbf{a_0},t) \\
&= \int_0^\infty dt \int_V d\mathbf{a} e^{t\mathscr{D}} \delta(\mathbf{a}-\mathbf{a_0}) \\
&= \int_0^\infty dt \int_V d\mathbf{a} \delta(\mathbf{a}-\mathbf{a_0}) \left(e^{t\mathscr{D}^+} 1\right) \\
&= \int_0^\infty dt \left(e^{t\mathscr{D}^+} 1\right).
\end{aligned} \tag{A.6}$$

Now, let us apply the adjoint operator,

$$\begin{aligned}
\mathscr{D}^+\tau &= \int_0^\infty dt \mathscr{D}^+ e^{t\mathscr{D}^+} 1 \\
&= \int_0^\infty dt \frac{d}{dt} e^{t\mathscr{D}^+} 1 \\
&= -1
\end{aligned} \tag{A.7}$$

In the case of the Smoluchowsky Eq., the above yields

$$\tau(x) = \frac{1}{D}\int_x^b dy e^{U(y)/kT} \int_a^y dz e^{-U(z)/kT}, \tag{A.8}$$

here the absorbing barrier is at b and a could be, in principle, $\pm\infty$.

In the case of the duffing oscillator we are interested in the first passage time to the maximum given the particle is initially in the left well. Therefore, Eq. (A.8) takes the following form

$$\tau(x) = \frac{1}{D}\int_x^0 dy e^{U(y)/kT} \int_{-\infty}^y dz e^{-U(z)/kT} \tag{A.9}$$

Now, when $kT \ll 1$, then we may extend the upper limit of integration to ∞.

The integral over y is practically independent of x as long as x is near the potential minimum, so the lower limit can be replaced by $-\infty$. Thus

$$\tau(x) = \frac{1}{D}\int_{-\infty}^0 dy e^{U(y)/kT} \int_{-\infty}^\infty dz e^{-U(z)/kT}, \tag{A.10}$$

Appendix B

Soft Henon-Heiles: Eigenvectors and Fits

B.1 Eigenvectors

In this section we obtain the eigenvectors and eigenvalues of the dynamical matrix. For this purpose, we introduce the ansatz $Q_j(t) = q_j e^{-\imath\omega t}$ in the corresponding Hamiltonian Eqs. , neglecting the non-linear terms, which yield

$$\left(\mathbf{D} - \omega^2 \mathbf{I}\right) \vec{q} = \vec{0}\,, \tag{B.1}$$

where $\mathbf{D}$ is the dynamic matrix given by

$$\mathbf{D} = k \begin{bmatrix} 1+\beta & -1 & -\beta \\ -1 & 1+\alpha & -\alpha \\ -\beta & -\alpha & \alpha+\beta \end{bmatrix}.$$

The eigenvalues of the dynamical matrix $\mathbf{D}$ are,

$$\begin{cases} \omega_0/k = 0, \\ \omega_x/k = 1+\alpha+\beta+\sqrt{1-\alpha+\alpha^2-\beta-\alpha\beta+\beta^2}\}\,, \\ \omega_y/k = 1+\alpha+\beta-\sqrt{1-\alpha+\alpha^2-\beta-\alpha\beta+\beta^2}\} \end{cases} . \tag{B.2}$$

Let us determine the eigenvectors. To do so, notice that since there are no fixed endpoints, the first eigenvalue corresponds to the center mass movement. Hence, one of the normal modes is,

$$|0\rangle = \frac{1}{\sqrt{3}} \begin{bmatrix} 1 \\ 1 \\ 1 \end{bmatrix}. \tag{B.3}$$

The remaining two eigenvectors must be orthonormal. Therefore, one way to tackle this is by considering two generic eigenvectors in the XY plane, i.e.,

$$|1,0\rangle = \begin{bmatrix} \sin\chi \\ -\cos\chi \\ 0 \end{bmatrix} . \tag{B.4}$$

$$|2,0\rangle = \begin{bmatrix} \cos\chi \\ \sin\chi \\ 0 \end{bmatrix} . \tag{B.5}$$

We rotate these vectors using the same rotation matrices which transforms vector $(0,0,1)$ into $(1,1,1)/\sqrt{3}$, i.e., first we rotate an angle θ_x such that $\cos\theta_x = 1/\sqrt{3}$ around the X axis clockwise, and then we rotate an angle $\theta_z = \pi/4$ around the Z axis clockwise. Thus

$$\mathbf{R}_x(\theta_x) = \begin{bmatrix} 1 & 0 & 0 \\ 0 & \cos\theta_x & -\sin\theta_x \\ 0 & \sin\theta_x & \cos\theta_x \end{bmatrix} ,$$

$$\mathbf{R}_x(\theta_x) = \begin{bmatrix} \cos\theta_z & -\sin\theta_z & 0 \\ \sin\theta_z & \cos\theta_z & 0 \\ 0 & 0 & 1 \end{bmatrix} ,$$

$$|1\rangle \equiv \mathbf{R}_z(\theta_z)\mathbf{R}_x(\theta_x)|1,0\rangle = \begin{bmatrix} -\frac{\cos\chi}{\sqrt{6}} + \frac{\sin\chi}{\sqrt{2}} \\ -\frac{\cos\chi}{\sqrt{6}} - \frac{\sin\chi}{\sqrt{2}} \\ \sqrt{\frac{2}{3}}\cos\chi \end{bmatrix} . \tag{B.6}$$

$$|2\rangle \equiv \mathbf{R}_z(\theta_z)\mathbf{R}_x(\theta_x)|2,0\rangle = \begin{bmatrix} \frac{\cos\chi}{\sqrt{2}} + \frac{\sin\chi}{\sqrt{6}} \\ -\frac{\cos\chi}{\sqrt{2}} + \frac{\sin\chi}{\sqrt{6}} \\ -\sqrt{\frac{2}{3}}\sin\chi \end{bmatrix} , \tag{B.7}$$

Now, notice that both eigenvectors must fulfill the characteristic equation for $\mathbf{D}$, from which we obtain, using $|2\rangle$ that

$$\tan\chi = \sqrt{3}\frac{2+\alpha-\omega_-^2}{3\alpha-\omega_-^2} . \tag{B.8}$$

Before moving on, notice that when $\alpha = \beta = 1$ the eigenvalues become $\{0,3\}$ being the last one degenerate. Also notice that making $\chi \to \chi - \pi/2$ in $|2\rangle$ gives $|1\rangle$.

Now that we have the eigenvectors, we diagonalize **D**. We define $|ic\rangle$ as the canonical base with $i = \{1,2,3\}$ and the matrix **A**, which diagonalizes the interaction, i.e., $\mathbf{D}_0 = \mathbf{ADA}^T$. Then A is

$$\mathbf{A} = |1c\rangle\langle 1| + |2c\rangle\langle 2| + |3c\rangle\langle 0| \tag{B.9}$$

$$= \begin{bmatrix} -\frac{\cos\chi}{\sqrt{6}} + \frac{\sin\chi}{\sqrt{2}} & -\frac{\cos\chi}{\sqrt{6}} - \frac{\sin\chi}{\sqrt{2}} & \sqrt{\frac{2}{3}}\cos\chi \\ \frac{\cos\chi}{\sqrt{2}} + \frac{\sin\chi}{\sqrt{6}} & -\frac{\cos\chi}{\sqrt{2}} + \frac{\sin\chi}{\sqrt{6}} & -\sqrt{\frac{2}{3}}\sin\chi \\ 1/\sqrt{3} & 1/\sqrt{3} & 1/\sqrt{3} \end{bmatrix} . \tag{B.10}$$

Therefore, the normal (canonical) coordinates are

$$\vec{x} = \mathbf{A}\vec{Q} , \tag{B.11}$$

$$\vec{p} = \mathbf{A}\vec{P} . \tag{B.12}$$

Hence, in our Hamiltonian we make the following substitutions:

$$Q_i = \sum \mathbf{A}^t_{ij} x_j , \tag{B.13}$$

$$P_i = \sum \mathbf{A}^t_{ij} y_j . \tag{B.14}$$

Substituting these last Eqs. in the Hamiltonian, we obtain the diagonalized Hamiltonian, i.e.,

$$H = \frac{1}{2}\left(p_x^2 + p_y^2 + p_z^2\right) + \frac{1}{2}\left(\omega_x^2 x^2 + \omega_y^2 y^2\right) . \tag{B.15}$$

Notice that p_z is a constant since z is a cyclic coordinate.

Consider the cubic interaction term, i.e.,

$$\frac{\gamma}{3}\left((Q_1 - Q_2)^3 + (Q_2 - Q_3)^3 + (Q_3 - Q_1)^3\right) , \tag{B.16}$$

and let us apply the transformation $Q_i \to x_i$. This last operation yields

$$\frac{3\gamma}{\sqrt{2}}\left(-\xi_2\left(\frac{\xi_2^2}{3} - \xi_3^2\right)\cos 3\chi + \xi_3\left(\frac{\xi_3^2}{3} - \xi_2^2\right)\sin 3\chi\right) . \tag{B.17}$$

In the case where $\alpha = \beta$, let us examine what happens to the angle θ. Notice that the matrix **D** becomes

$$\mathbf{D} = \begin{bmatrix} 1+\beta & -1 & -\beta \\ -1 & 1+\beta & -\beta \\ -\beta & -\beta & 2\beta \end{bmatrix} ,$$

with eigenvalues $\omega_y^2 = 2+\beta$ and $\omega_x^2 = 3\beta$. When fixing the angle θ for which the secular Eq. is fulfilled, we may use

$$-\beta\left(\sqrt{\frac{2}{3}}\sin\chi\right) - \left(2\beta - \omega_{x,y}^2\right)\sqrt{\frac{2}{3}}\sin\chi = 0\,, \tag{B.18}$$

which is the last Eq. of $\left(\mathbf{D} - \omega_{2,3}^2\mathbf{I}\right)|2\rangle = 0$. Now, if we plug in the eigenvalue 3β in Eq. (B.18) we obtain the trivial solution. On the contrary, when we plug in the eigenvalue $2+\beta$ in Eq. (B.18), this tells us that $\chi = n\pi$, with $n = 0, 1, 2, ...$ We diagonalize the matrix $\mathbf{D}$ by obtaining the following diagonal matrix $\mathbf{D}_0$:

$$\mathbf{D}_0 = \mathbf{A}\mathbf{D}\mathbf{A}^T = \begin{bmatrix} d_{11}(\chi) & 0 & 0 \\ 0 & d_{22}(\chi) & 0 \\ 0 & 0 & d_{33}(\chi) \end{bmatrix}. \tag{B.19}$$

For $\chi = n\pi$, according to Eq. (B.18) we should expect that $d_{11}(\chi) = \omega_x^2$, $d_{22}(\chi) = \omega_y^2$ and $d_{33}(\chi) = 0$. The last case occurs because, as previously mentioned, the eigenvector $|2\rangle$ becomes $|1\rangle$, and conversely $|1\rangle \rightarrow |2\rangle$

Hence, when $\alpha = \beta$, $\chi = n\pi$ and the corresponding eigenvectors becomes

$$|2+\beta\rangle = \frac{1}{\sqrt{2}}\begin{bmatrix} (-1)^n \\ (-1)^{n+1} \\ 0 \end{bmatrix}. \tag{B.20}$$

$$|3\beta\rangle = \frac{1}{\sqrt{6}}\begin{bmatrix} (-1)^{n+1} \\ (-1)^{n+1} \\ 2(-1)^n \end{bmatrix}. \tag{B.21}$$

Finally, the Hamiltonian in terms of the normal coordinates and momenta is

$$H = \frac{1}{2}\left(p_x^2 + p_y^2 + p_z^2\right) + \frac{1}{2}\left(\omega_x^2 x^2 + \omega_y^2 y^2\right) + \frac{3\gamma}{2^{1/2}}\nu\left(\frac{1}{3}y^3 - x^2 y\right), \tag{B.22}$$

where $\nu = \{-1, 1\}$.

B.2 Fits

In figures B.1, B.2, B.3 and B.4 we show the curves of $\log N(t)/N(0)$ vs t for times corresponding to the exponential decay regime and their linear fit for each of the combinations of β and ΔE shown in figure 3. The time intervals t_{fit} used in the fitting process for each of the curves were selected following two

criteria. The remaining population after t_{fit} should be below 50%, which ensures that the regime in that time interval corresponds to the exponential decay. The fitting curve should go over the real data for the most part, such that the absolute value of the slope of the fitting curve, i.e., α will be smaller than or equal to the absolute value of the slope of the real data. In this sense, these α values correspond to lower bounds. Notice from figure 9 that the α obtained from the fitting method almost always goes over the α obtained by the flux method. Thus, if one were to improve the fit by choosing a smaller time interval, the divergence between both methods would grow.

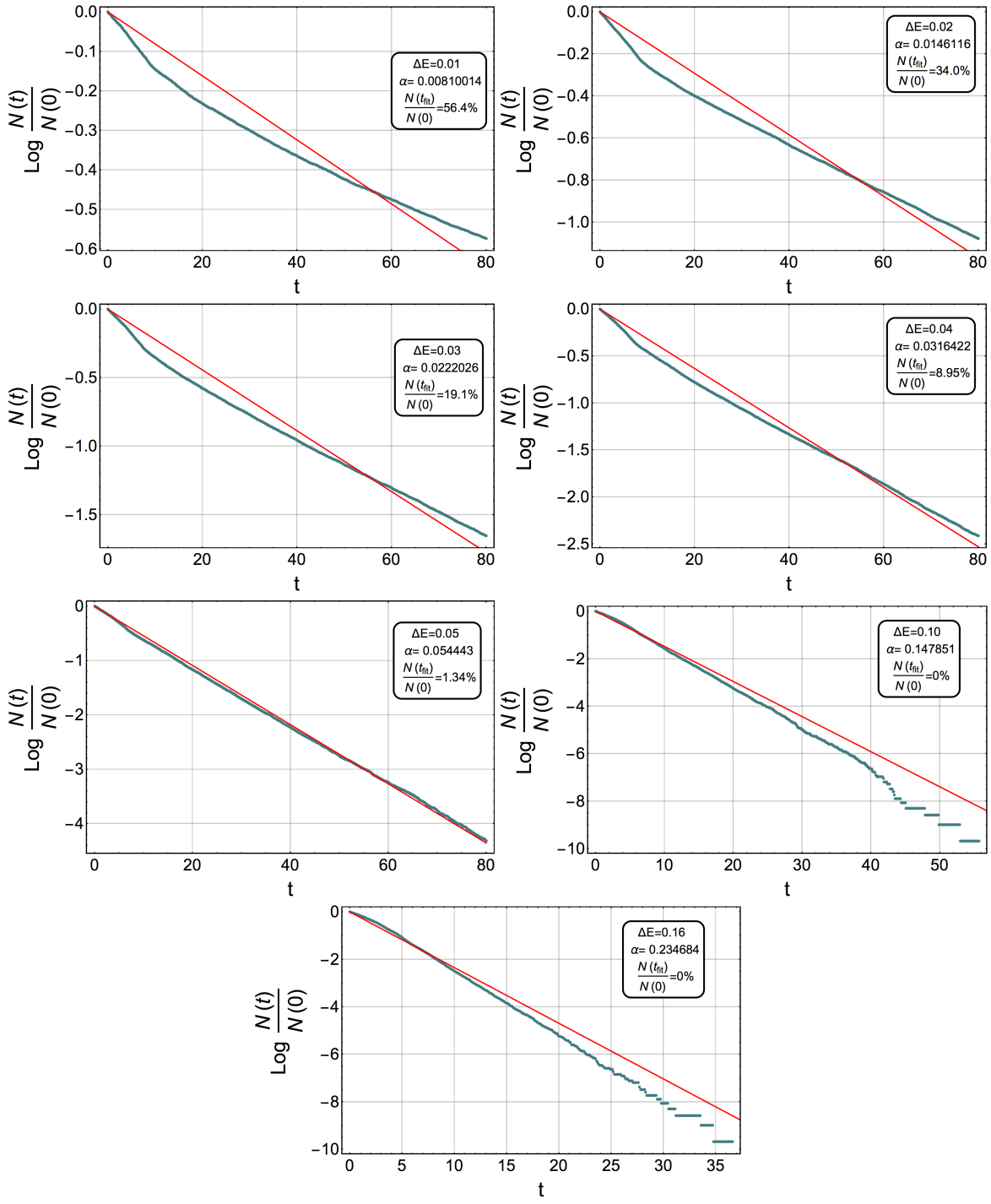

Figure B.1: $\beta = 0.8$. $\log N(t)/N(0)$ vs t (blue curve) and their linear fit (red curve) for different ΔE (see insets). The α parameter shown in the inset is the slope absolute value of the fit. The fit was done in a time interval t_{fit} such that after that time the remaining population is the one shown in the inset.

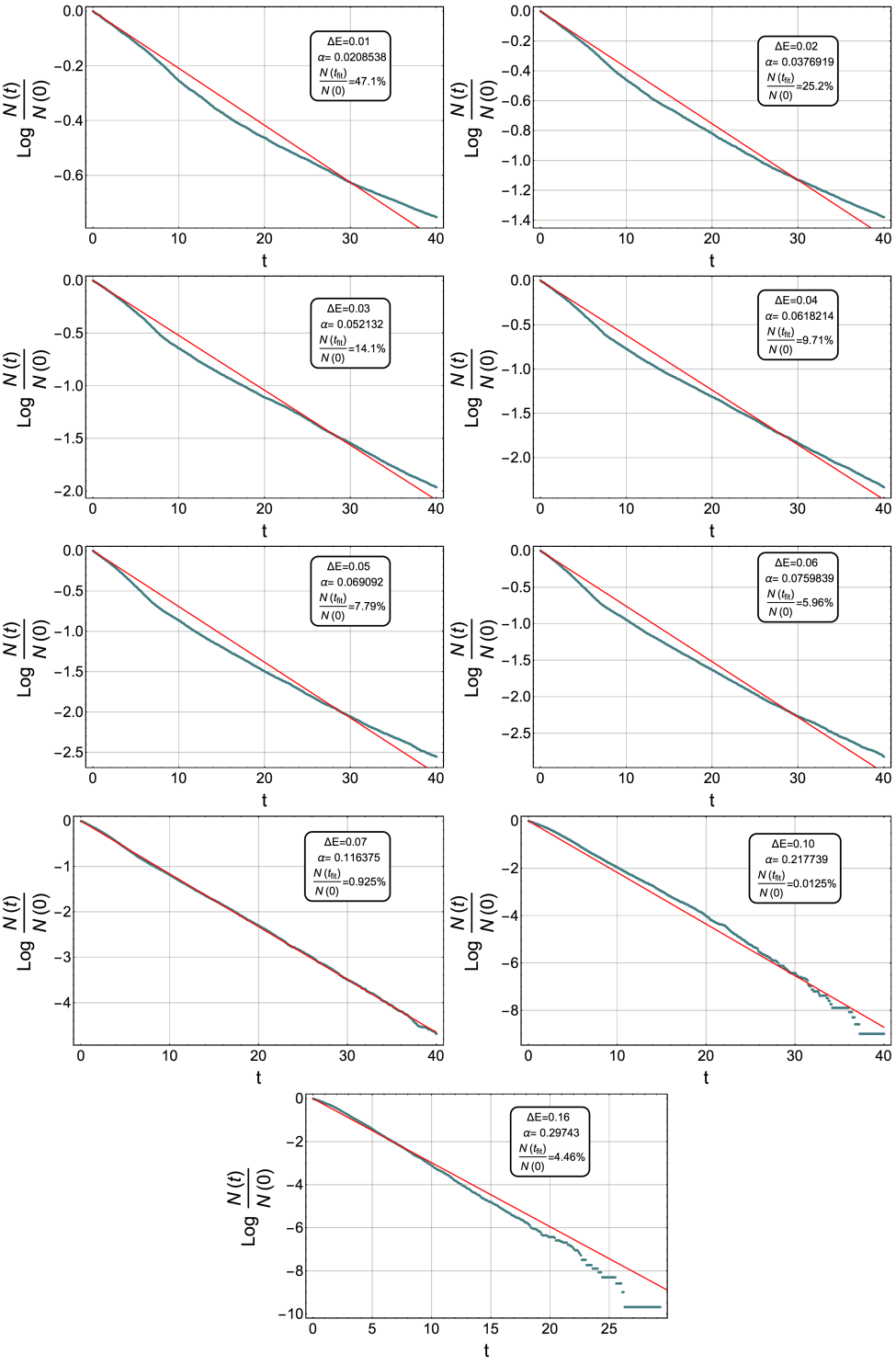

Figure B.2: $\beta = 0.6$. $\log N(t)/N(0)$ vs t (blue curve) and their linear fit (red curve) for different ΔE (see insets). The α parameter shown in the inset is the slope absolute value of the fit. The fit was done in a time interval t_{fit} such that after that time the remaining population is the one shown in the inset.

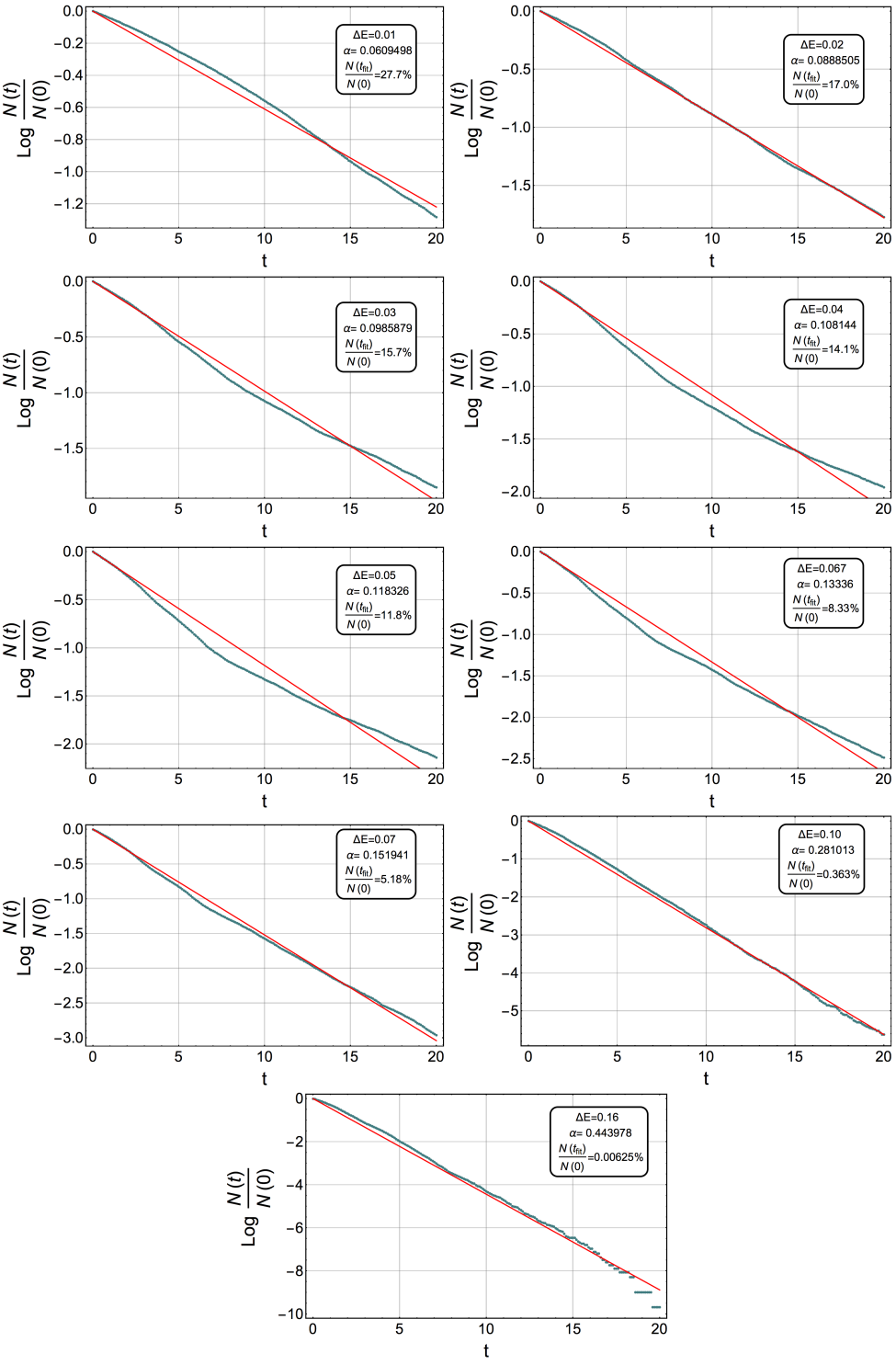

Figure B.3: $\beta = 0.4$. $\log N(t)/N(0)$ vs t (blue curve) and their linear fit (red curve) for different ΔE (see insets). The α parameter shown in the inset is the slope absolute value of the fit. The fit was done in a time interval t_{fit} such that after that time the remaining population is the one shown in the inset.

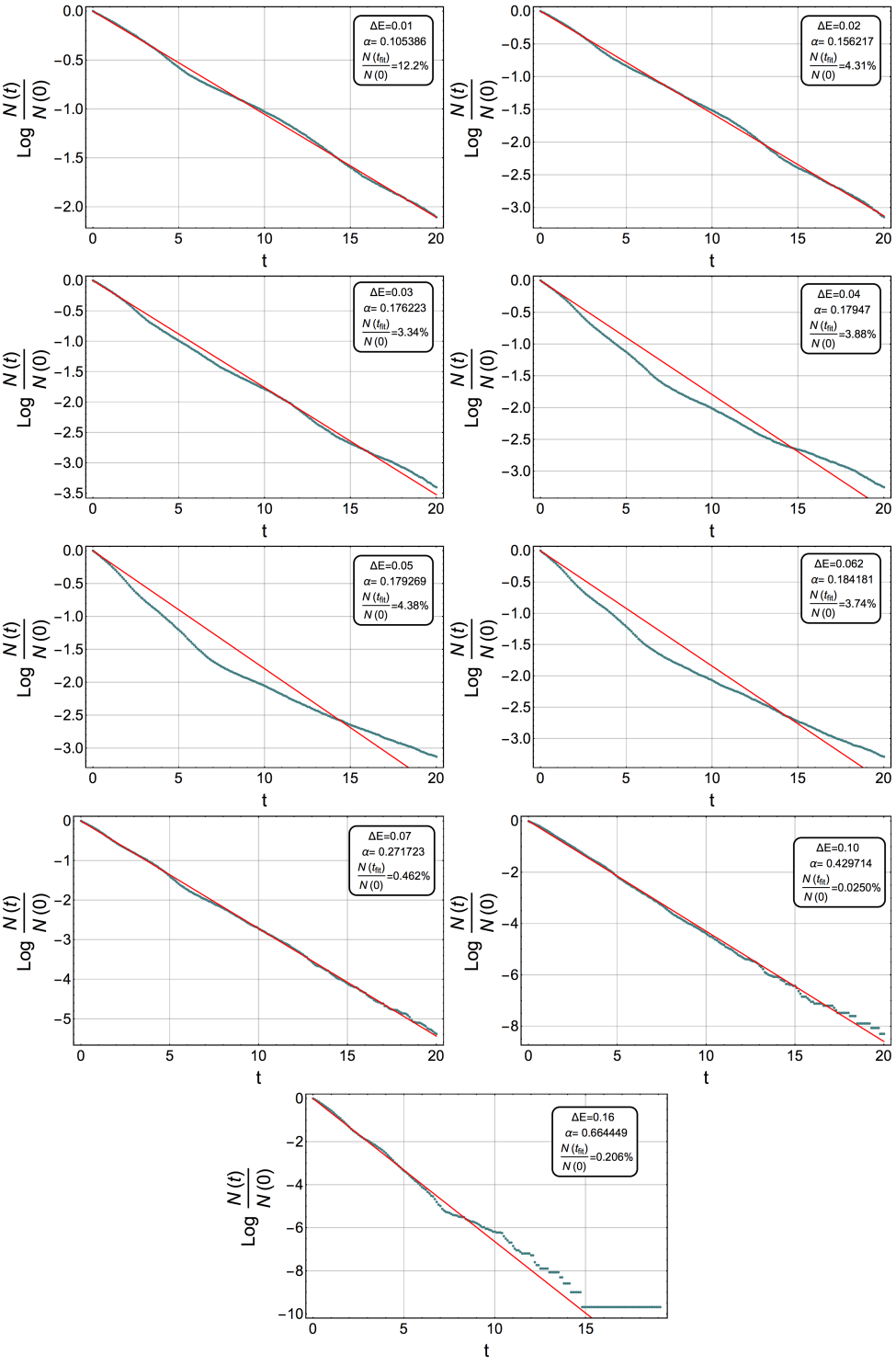

Figure B.4: $\beta = 0.2$. $\log N(t)/N(0)$ vs t (blue curve) and their linear fit (red curve) for different ΔE (see insets). The α parameter shown in the inset is the slope absolute value of the fit. The fit was done in a time interval t_{fit} such that after that time the remaining population is the one shown in the inset.

Appendix C

Transversal current correlation function (TCCF)

A vector field, $\boldsymbol{J}(\boldsymbol{r},t)$, may be expressed expressed as a longitudinal and a transversal part, i.e.,

$$\boldsymbol{J}(\boldsymbol{r},t)=\boldsymbol{J}_L(\boldsymbol{r},t)+\boldsymbol{J}_T(\boldsymbol{r},t)\,, \tag{C.1}$$

which usually $\boldsymbol{J}_L(\boldsymbol{r},t)$ is related to a gradient while $\boldsymbol{J}_T(\boldsymbol{r},t)$ is related to a rotational. Thus,

$$\begin{cases}\boldsymbol{J}_L(\boldsymbol{r},t)=-\nabla\phi\,,\\ \boldsymbol{J}_T(\boldsymbol{r},t)=\nabla\times\boldsymbol{A}(\boldsymbol{r},t)\,.\end{cases} \tag{C.2}$$

Now, using Helmholtz decomposition theorem we find the relation between $\boldsymbol{J}(\boldsymbol{r},t)$ and $\boldsymbol{A}(\boldsymbol{r},t)$.

In three dimensions and considering an unbounded volume, we have

$$\boldsymbol{A}(\boldsymbol{r},t)=\frac{1}{4\pi}\int_{\text{all space}}d^3\boldsymbol{r}'\frac{\nabla'\times\boldsymbol{J}(\boldsymbol{r}',t)}{|\boldsymbol{r}-\boldsymbol{r}'|}\,. \tag{C.3}$$

Now, we are interested in the Fourier transform of $\boldsymbol{J}(\boldsymbol{r},t)$. We know that

$$\boldsymbol{J}_T(\boldsymbol{k},t)=\imath\boldsymbol{k}\times\boldsymbol{A}(\boldsymbol{k},t)\,. \tag{C.4}$$

Furthermore, notice that Eq. (C.3) is a convolution in space between $\boldsymbol{J}(\boldsymbol{r},t)$ and $1/|\boldsymbol{r}|$, hence denoting the Fourier transform operator as $\mathscr{F}$, we may equate

$$\boldsymbol{A}(\boldsymbol{k},t)=\frac{1}{4\pi}\imath\boldsymbol{k}\times\boldsymbol{J}(\boldsymbol{k},t)\,\mathscr{F}\{1/|\boldsymbol{r}|\}(\boldsymbol{k})\,. \tag{C.5}$$

Now, to determine the Fourier transform of $1/|\boldsymbol{r}|$ we do the following:

$$\begin{aligned}
\int d^3\boldsymbol{r}\frac{e^{-\lambda|\boldsymbol{r}|}}{|\boldsymbol{r}|}e^{-\imath\boldsymbol{k}\cdot\boldsymbol{r}} &= 2\pi\int_0^\pi d\theta\int_0^\infty dr\, r^2\sin\theta\frac{e^{-\lambda r-\imath kr\cos\theta}}{r}\\
&= \frac{2\pi}{\imath k}\int_0^\infty dr e^{-\lambda r}\left(e^{\imath kr}-e^{-\imath kr}\right)\\
&= \frac{2\pi}{\imath k}\left(\frac{e^{\imath kr-\lambda r}}{\imath k-\lambda}+\frac{e^{-\imath kr-\lambda r}}{\imath k+\lambda}\right)\Bigg|_0^\infty\\
&= \frac{2\pi}{\imath k}\left(-\frac{1}{\imath k-\lambda}-\frac{1}{\imath k+\lambda}\right)\\
&= -\frac{2\pi}{\imath k}\left(\frac{1}{\imath k+\lambda}-\frac{1}{\lambda-\imath k}\right)\\
&= -\frac{2\pi}{\imath k}\left(\frac{\lambda-\imath k-\imath k-\lambda}{k^2+\lambda^2}\right)\\
&= -\frac{2\pi}{\imath k}\frac{-2\imath k}{k^2+\lambda^2}\\
&= \frac{4\pi}{k^2+\lambda^2}\longrightarrow\frac{4\pi}{k^2}\,. \qquad \text{(C.6)}
\end{aligned}$$

Therefore, we have

$$\begin{aligned}
\boldsymbol{J}_T(\boldsymbol{k},t) &= \imath\boldsymbol{k}\times\left(\frac{1}{4\pi}\imath\boldsymbol{k}\times\boldsymbol{J}(\boldsymbol{k},t)\frac{4\pi}{k^2}\right)\\
&= -\frac{1}{k^2}\boldsymbol{k}\times(\boldsymbol{k}\times\boldsymbol{J}(\boldsymbol{k},t))\,. \qquad \text{(C.7)}
\end{aligned}$$

There is a vectorial identity that yields

$$\boldsymbol{A}\times(\boldsymbol{B}\times\boldsymbol{C})=(\boldsymbol{A}\cdot\boldsymbol{C})\,\boldsymbol{B}-(\boldsymbol{A}\cdot\boldsymbol{B})\,\boldsymbol{C}\,. \qquad \text{(C.8)}$$

Hence, we may write

$$\boldsymbol{J}_T(\boldsymbol{k},t)=\frac{1}{k^2}\left(k^2\boldsymbol{J}(\boldsymbol{k},t)-(\boldsymbol{k}\cdot\boldsymbol{J}(\boldsymbol{k},t))\,\boldsymbol{k}\right)\,. \qquad \text{(C.9)}$$

The TCCF is defined by

$$C_T(k,t)=\langle\boldsymbol{J}_T(\boldsymbol{k},t)\boldsymbol{J}_T^*(\boldsymbol{k},0)\rangle\,. \qquad \text{(C.10)}$$

Here t is time, $\boldsymbol{k}$ is the wave vector, $\langle\ldots\rangle$ is an average over the ensemble (including the different directions of $\boldsymbol{k}$). Hence,

$$C_T(k,t)=\langle\boldsymbol{J}(\boldsymbol{k},t)\cdot\boldsymbol{J}^*(\boldsymbol{k},0)-\left(\hat{k}\cdot\boldsymbol{J}(\boldsymbol{k},t)\right)\left(\hat{k}\cdot\boldsymbol{J}^*(\boldsymbol{k},0)\right)\rangle\,. \qquad \text{(C.11)}$$

Now, let us denote the initial value as $J(k,0)=v_0^2$.

The function $C_T(k,t)$ satisfies the linearized Navier-Stokes Eq., i.e.,

$$\frac{\partial C_T(k,t)}{\partial t}=-\nu k^2C_T(k,t)\,. \qquad \text{(C.12)}$$

Using Laplace Transform, the previous Eq. yields

$$C_T(k,s) = \frac{v_0^2}{s+\nu k^2} \tag{C.13}$$

Now, given the parity of $C_T(k,t)$, the Fourier Transform of will only have real part. Furthermore, notice that

$$C_T(k,\omega) = 2\mathbf{Re}\left[\int_0^\infty dt e^{-\imath\omega t} C_T(k,t)\right] = 2\mathbf{Re}\left[\int_0^\infty dt e^{-st} C_T(k,t)|_{s=\imath\omega}\right] = 2\mathbf{Re}\left[C_T(k,s)|_{s=\imath\omega}\right] . \tag{C.14}$$

Hence, the TCCF in Fourier space is

$$C_T(k,\omega) = \frac{2v_0^2\nu k^2}{\omega^2 + (\nu k^2)^2} . \tag{C.15}$$

This simple result tells us that the correlation function decays as a simple exponential, i.e., $C_T(k,t) \sim \exp(-\nu k^2|t|)$. Here, $\nu = \eta/nM$ is the kinematic viscosity. We immediately notice the characteristic time $\tau(k) = 1/\nu k^2$.

The previous sketch has been taken from ref. (114). The result arrived in Eq. (C.15) is telling us that, although there are some transversal density fluctuations happening at $\omega \neq 0$, the prominent ones happen at $\omega = 0$. This agrees with the fact that in liquids shear stress is unsustainable, at least at small k and long times. There is (or at least, should be) a k_c where above this threshold the liquid is able to sustain shear wave propagation. Yip and Boon argue that for $k \geq 2\pi/l$ the TCCF behaves as a Gaussian, i.e.,

$$C_T^{k\geq}(k,t) = 2v_0^2 \frac{\sqrt{2\pi}}{kv_0} e^{-\frac{1}{2}\left(\frac{\omega}{kv_0}\right)^2} . \tag{C.16}$$

Notice that the second moment is

$$\omega^2 = \frac{\left(kv_0^2\right)^2}{nM} G_\infty(k) . \tag{C.17}$$

Thus, what would be really swell is to appropriately determine the TCCF that works for any k value as well as ω and actually captures this crossover between viscous and elastic behavior. This viscoelastic behavior is usually modeled by an interpolation between solid and liquid behavior. The problem with this approach is that it oversimplifies matters. Perhaps a rather *ad hoc* approach would be to consider a memory kernel in Eq. (C.12), i.e.,

$$\frac{\partial C_T(k,t)}{\partial t} = -k^2 \int_0^t dt' Q(k,t-t') C_T(k,t') . \tag{C.18}$$

There are some conditions this memory kernel must fulfill, namely, from Eq. (C.17) it is easy to see that

$$Q(k,t=0) = \frac{1}{nM} G_\infty(k) . \tag{C.19}$$

We might as well think of a characteristic time, say, τ such that for $t \gg \tau$ the main contribution occurs at $t' = t$, then $J(k,t') \to J(k,t)$ and (This can be proved mathematically by changing variable $u = t - t'$ and then doing a Taylor expansion to order zeroth around $u = 0$ of $J(k, t-u)$.)

$$\lim_{k\to 0}\int_0^\infty dt' Q(k,t') = \nu\,. \tag{C.20}$$

Then, the TCCF will have the same form as in Eq. (C.15), i.e.,

$$C_T(k,\omega) = 2\mathbf{Re}\left[\frac{v_0^2}{\imath\omega + k^2 Q(k,\imath\omega)}\right]. \tag{C.21}$$

Here $Q(k,\imath\omega)$ is the Laplace Transform of the kernel memory function $Q(k,t)$ with $s \to \imath\omega$. Now, in general $Q(k,\imath\omega) = Q'(k,\omega) + \imath Q''(k,\omega)$, where $Q'(k,\omega)$ and $Q''(k,\omega)$ are both real functions. Thus, the previous Eq. may be expressed as

$$C_T(k,\omega) = 2\frac{v_0^2 k^2 Q'(k,\omega)}{\left(\omega + k^2 Q''(k,\omega)\right)^2 + \left(k^2 Q'(k,\imath\omega)\right)^2}\,. \tag{C.22}$$

Yip and Boon go on trying different memory kernel function, for instance, they tried a simple exponential which they analyze in detail, as well as a Gaussian and the sum of two simple exponential functions. In the case of the simple exponential they find the Maxwell relation, i.e., $\tau(k) = \eta/G_\infty(0)$. They also find an inequality which if fulfilled the liquid is able to sustain shear wave propagation. This condition is

$$k^2 Q(k,0) > \frac{1}{2\tau^2(k)} \tag{C.23}$$

Although Yip and Boon's results give a picture of the liquid behavior for different length and time scales, the model is perhaps oversimplified. It has been long before argued that there are several characteristic times in liquids (as well as in other complex systems) which give place to dynamical heterogeneity. Therefore, the kernel memory should depend on various characteristic times. In order to take this into account one might be tempted to consider a stretched exponential, and I believe it is something worth looking at later. But for now, let us consider a kernel memory given by

$$Q(k,t) = Q(k,0)\prod_{i=1}^{N}\int_0^t dt_i Q_i(t_i)\delta\left(t - \sum_i t_i\right). \tag{C.24}$$

Then, in Laplace time,

$$Q(k,s) = Q(k,0)\prod_{i=1}^{N} Q_i(s)\,. \tag{C.25}$$

Let us consider $N = 2$ and $Q_i(t) = \exp(t/\tau_i)$. Then,

$$Q(k,\omega) = Q(k,0)\left(\frac{\tau_1\tau_2(1-\omega^2\tau_1\tau_2)}{(1+\omega^2\tau_1^2)(1+\omega^2\tau_2^2)} - \imath\frac{\tau_1\tau_2(\tau_1+\tau_2)\omega}{(1+\omega^2\tau_1^2)(1+\omega^2\tau_2^2)}\right) \tag{C.26}$$

Making the substitution in Eq. (C.22) and some algebra we obtain

$$C_T(k,\omega) = 2v_0^2 k^2 Q(k,0) \frac{\tau_1\tau_2(1-\omega^2\tau_1\tau_2)(1+\omega^2(\tau_1^2+\tau_2^2)+\omega^4\tau_1^2\tau_2^2)}{k^4Q^2(k,0)\tau_1^2\tau_2^2(1-\omega^2\tau_1\tau_2)^2+\omega^2\left(1+\omega^2(\tau_1^2+\tau_2^2)+\omega^4\tau_1^2\tau_2^2-k^2Q^2(k,0)\tau_1\tau_2(\tau_1+\tau_2)\right)^2} \tag{C.27}$$

Notice that even for $N = 2$, the TCCF explicit form is a bit overwhelming and little insight would be gained from further exploration. Yet, this provides a picture on how the characteristic time scale affect the TCCF.

Appendix D

Radial distribution function and structure factor

Here we relate the (static) coordination number with the current density correlation function. Let us denote as $g(\boldsymbol{r}) \equiv g(r)$ the radial distribution function. The probability for a particle to have a particle located between $\boldsymbol{r}$ and $\boldsymbol{r}+d\boldsymbol{r}$ is proportional to $\propto g(r)d^3\boldsymbol{r}$. In general (187), we may consider a system of N particles such that the Hamiltonian yields

$$\begin{aligned} H &= \frac{1}{2m}\sum_i \langle \boldsymbol{p}_i^2 \rangle + \langle V_N(\{\boldsymbol{r}\}) \rangle \\ &= \frac{3}{2}NkT + \frac{1}{2}\langle \sum_{ij} \phi(\boldsymbol{r}_{ij}) \rangle \\ &= \frac{3}{2}NkT + \frac{1}{2}N\rho \int d^3\boldsymbol{r}\phi(\boldsymbol{r})g(\boldsymbol{r}) \end{aligned} \tag{D.1}$$

Where we have used

$$\rho g(\boldsymbol{r}) = \frac{1}{N}\langle \sum_{ij} \delta\left(\boldsymbol{r} - \boldsymbol{r}_{ij}\right) \rangle \tag{D.2}$$

Notice that integrating the previous Eq. over all accessible volume yields

$$N - 1 = \rho \int d^3\boldsymbol{r}\, g(r)\,. \tag{D.3}$$

Now, under certain conditions (isotropic, homogeneous??...), this function relates to the structure factor $S(\boldsymbol{k})$ by

$$S(\boldsymbol{k}) = 1 + \rho \int d^3\boldsymbol{r}\left(g(\boldsymbol{r}) - 1\right) e^{-\imath \boldsymbol{k}\cdot\boldsymbol{r}}\,. \tag{D.4}$$

Thus,

$$\rho g(\boldsymbol{r}) = \rho + \frac{1}{(2\pi)^3}\int d^3\boldsymbol{k} e^{\imath \boldsymbol{k}\cdot\boldsymbol{r}}\left(S(\boldsymbol{k}) - 1\right) \tag{D.5}$$

The relation between the structure factor and the longitudinal current correlation function is given by

$$C_L(\boldsymbol{k},t) = \frac{\omega^2}{k^2} S(\boldsymbol{k},\omega)\,. \tag{D.6}$$

Lastly, the LCCF and the TCCF are related by

$$\boldsymbol{J}(\boldsymbol{k},t)\cdot\boldsymbol{J}(\boldsymbol{k},0) = C_L(\boldsymbol{k},t) + C_T(\boldsymbol{k},t)\,. \tag{D.7}$$

Then, we may write

$$\begin{aligned} N-1 &= \int d^3\boldsymbol{r}\left(\rho + \frac{1}{(2\pi)^3}\int d^3\boldsymbol{k} e^{\imath\boldsymbol{k}\cdot\boldsymbol{r}}\left(S(\boldsymbol{k})-1\right)\right) \\ &= N-1+S(\boldsymbol{k}=0) \end{aligned} \tag{D.8}$$

Now, let us relate the coordination number with the structure factor and so on. Thus, we integrate over a volume δV,

$$\begin{aligned} z &= \int_{\delta V} d^3\boldsymbol{r}\left(\rho + \frac{1}{(2\pi)^3}\int d^3\boldsymbol{k} e^{\imath\boldsymbol{k}\cdot\boldsymbol{r}}\left(S(\boldsymbol{k})-1\right)\right) \\ &= \frac{N\delta V}{V} - 1 + \frac{1}{(2\pi)^3}\int_{\delta V} d^3\boldsymbol{r}\int d^3\boldsymbol{k} S(\boldsymbol{k}) e^{\imath\boldsymbol{k}\cdot\boldsymbol{r}}\,. \end{aligned} \tag{D.9}$$

Hence,

$$\begin{aligned} z+1-\frac{N\delta V}{V} &= \frac{1}{(2\pi)^3}\int_{\delta V} d^3\boldsymbol{r}\int d^3\boldsymbol{k} S(\boldsymbol{k}) e^{\imath\boldsymbol{k}\cdot\boldsymbol{r}} \\ &= \frac{1}{(2\pi)^3}\int_{\delta V} d^3\boldsymbol{r}\int d^3\boldsymbol{k}\int d\omega S(\boldsymbol{k},\omega) e^{\imath\boldsymbol{k}\cdot\boldsymbol{r}} \\ &= \frac{1}{(2\pi)^3}\int_{\delta V} d^3\boldsymbol{r}\int d^3\boldsymbol{k}\int d\omega \frac{k^2}{\omega^2} C_L(\boldsymbol{k},\omega) e^{\imath\boldsymbol{k}\cdot\boldsymbol{r}}\,. \end{aligned} \tag{D.10}$$

Notice that

$$C_L(k,\omega) = \boldsymbol{J}_L(\boldsymbol{k},\omega)\cdot\boldsymbol{J}_L^*(\boldsymbol{k},0)\,. \tag{D.11}$$

Then,

$$C_L(\boldsymbol{r},\omega) = \int d^3\boldsymbol{r}'\boldsymbol{J}_L(\boldsymbol{r}+\boldsymbol{r}',\omega)\cdot\boldsymbol{J}_L(\boldsymbol{r}',0)\,. \tag{D.12}$$

Hence, notice the following:

$$\begin{aligned} \int d^3\boldsymbol{r}\nabla^2 C_L(\boldsymbol{r},\omega) e^{-\imath\boldsymbol{k}\cdot\boldsymbol{r}} &= \int d^3\boldsymbol{r}\{\nabla^2\left(C_L(\boldsymbol{r},\omega)e^{-\imath\boldsymbol{k}\cdot\boldsymbol{r}}\right) - \nabla^2\left(e^{-\imath\boldsymbol{k}\cdot\boldsymbol{r}}\right)C_L(\boldsymbol{r},\omega)\} \\ &= \int d^3\boldsymbol{r}\nabla^2\left(C_L(\boldsymbol{r},\omega)e^{-\imath\boldsymbol{k}\cdot\boldsymbol{r}}\right) + k^2\boldsymbol{J}_L(\boldsymbol{k},\omega)\cdot\boldsymbol{J}_L^*(\boldsymbol{k},0) \\ &= \int dS\nabla\left(C_L(\boldsymbol{r},\omega)e^{-\imath\boldsymbol{k}\cdot\boldsymbol{r}}\right)\cdot\hat{n} + k^2\boldsymbol{J}_L(\boldsymbol{k},\omega)\cdot\boldsymbol{J}_L^*(\boldsymbol{k},0) \\ &= k^2\boldsymbol{J}_L(\boldsymbol{k},\omega)\cdot\boldsymbol{J}_L^*(\boldsymbol{k},0)\,. \end{aligned} \tag{D.13}$$

Therefore,

$$z+1-\frac{N\delta V}{V}=\frac{1}{(2\pi)^3}\int_{\delta V}d^3\boldsymbol{r}\int d^3\boldsymbol{k}\int d\omega\frac{1}{\omega^2}\int d^3\boldsymbol{\xi}\nabla^2 C_L(\boldsymbol{\xi},\omega)e^{-\imath\boldsymbol{k}\cdot\boldsymbol{\xi}}e^{\imath\boldsymbol{k}\cdot\boldsymbol{r}}\,. \tag{D.14}$$

The previous result relates the coordination number with the longitudinal current correlation function. Further manipulations to relate the coordination number with the transversal current correlation function requires being able to relate the TCCF with its counter part using a different Eq. than the actual definition (Eq. (D)). This will depend on the isotropy of the given system.

Appendix E

Liquid-Liquid transition network glass model

E.1 Linear Approximation

In this note we derive Eq. (4) of the main work. For this, let us consider a two-dimensional triangular lattice of N particles connected by N_s springs. Now, we denote an infinitesimal displacement field of the particles by $|\delta \boldsymbol{R}\rangle$, while the change of length in the springs we denote them as $|\delta r\rangle$. In the case of small displacements, the following equality $|\delta r\rangle = \mathscr{S}|\delta \mathrm{R}\rangle$ holds. Here $\mathscr{S}$ is a $N_s \times dN$ matrix, that relates particle displacements with spring deformation. To simplify notation, we write $\mathscr{S}$ as a $N_s \times dN$ matrix of components of dimension d which gives $S_{\gamma,i} = \partial r_\gamma / \partial \boldsymbol{R_i} = \delta_{\gamma,i}\, \boldsymbol{n}_\gamma$, where $\delta_{\gamma,i}$ is 1 when spring γ is connected with particle i and is zero otherwise. $\boldsymbol{n}_\gamma$ is a unit vector in the direction of the spring γ and pointing to the particle i. Using the bra-ket notation, we may rewrite $\mathscr{S} = \sum_{\langle ij\rangle \equiv \gamma} |\gamma\rangle \boldsymbol{n}_\gamma \left(\langle i| - \langle j|\right)$, where the sum is over all springs in the network. Note, that the transpose of $\mathscr{S}$, $\mathscr{S}^t$, relates the set of contact forces $|f\rangle$ to the set of unbalanced forces $|\boldsymbol{F}\rangle$ on the particles, namely, $|\boldsymbol{F}\rangle = \mathscr{S}^t|f\rangle$, which simply follows from the gact that $F_i = \sum_\gamma \delta_{\gamma,i} f_\gamma \boldsymbol{n}_\gamma = \sum_\gamma f_\gamma \mathscr{S}_{\gamma,i}$. (188)

On the other hand, the dynamic matrix $\tilde{\mathscr{M}}$ is a linear operator connecting external forces with the displacements, i.e., $\tilde{\mathscr{M}}|\delta \boldsymbol{R}\rangle = |\boldsymbol{F}\rangle$. Let us denote as $\mathscr{K}$ the $N_s \times N_s$ diagonal matrix whose components are the springs' stiffnessess, that means, $\mathscr{K}_{\gamma\gamma} = k_\gamma \equiv k$. Thus, for harmonic springs, we have $|f\rangle = \mathscr{K}|\delta r\rangle$. Applying $\mathscr{S}^t$ to the previous equality yields $|\boldsymbol{F}\rangle = \mathscr{S}^t \mathscr{K} \mathscr{S}|\delta \boldsymbol{R}\rangle$. Therefore, the dynamic matrix may be expressed as

$$\tilde{\mathscr{M}} = \mathscr{S}^t \mathscr{K} \mathscr{S}\,. \tag{E.1}$$

Since in our model we are considering strong and weak interactions, we make this explicit by expressing the previous Eq. as $\tilde{\mathscr{M}} = k\left(\mathscr{S}^t\mathscr{S} + \frac{k_w}{k}\mathscr{S}_w^t\mathscr{S}_w\right)$, where $\mathscr{S}_w^t$ is a projection of $\mathscr{S}^t$ to the weak-

springs-interaction subspace. Now, let us consider the mean-field limit of weak interactions together with the limit of weak interactions, such that the coordination number for weak interactions $z_w \to \infty$ while the stiffness of weak interactions $k_w \to 0$ in a way that $\alpha \equiv z_w k_w / zk = const > 0$. Under these considerations, the weak springs lead to an effective interaction between each particle and the center of mass of the system, so that,

$$\tilde{\mathscr{M}} \approx k\left(\mathscr{S}^t\mathscr{S} + \alpha\mathscr{I}\right). \tag{E.2}$$

where $\mathscr{I}$ is the $dN \times dN$ identity matrix.

Let us assume that starting from a configuration where all springs are at rest, the rest lengths of the springs are changed by some amount $|y\rangle$. This will generate an unbalanced force field $|\boldsymbol{F}\rangle = \mathscr{S}^t\mathscr{K}|y\rangle$ on the particles, which will lead to a displacement $|\delta\boldsymbol{R}\rangle = \mathscr{M}^{-1}\mathscr{S}^t\mathscr{K}|y\rangle$. The elastic energy $H = \frac{1}{2}\langle y = \delta r|\mathscr{K}|y - \delta r\rangle$ is minimal for this displacement and the corresponding energy H is:

$$H\left(|y\rangle\right) = \frac{1}{2}\langle y|\mathscr{K} - \mathscr{K}\mathscr{S}\mathscr{M}^{-1}\mathscr{S}^t\mathscr{K}|y\rangle. \tag{E.3}$$

In our model, $y_\gamma = 0$ for weak springs and $y_\gamma = \epsilon\sigma_\gamma$ for strong springs, where ϵ_γ is a Gaussian variable and, hence we obtain Eq. (3) of the main text. Introducing the dimensionless dynamic matrix $\mathscr{M} = \tilde{\mathscr{M}}/k$ and the restriction $\mathscr{S}_s^t$ of the operator $\mathscr{S}^t$ on the subspace of strong springs of dimension N_s, i.e., $\mathscr{S}_s^t|\sigma\rangle \equiv \mathscr{S}^t|y\rangle$. Thus, Eq. E.3 becomes

$$H\left(\{\sigma_i\}\right) = \frac{1}{2}\langle\sigma|\mathscr{G}|\sigma\rangle. \tag{E.4}$$

Where the matrix $\mathscr{G}$ has the following form:

$$\mathscr{G} = \mathscr{I} - \mathscr{S}_s\mathscr{M}^{-1}\mathscr{S}_s^t. \tag{E.5}$$

Now, let us express $\mathscr{S}_s^t\mathscr{S}_s$ in an eigenvalue decomposition, i.e.,

$$\mathscr{S}_s^t\mathscr{S}_s = \sum_\omega \omega^2 |\delta\boldsymbol{R}_\omega\rangle\langle\delta\boldsymbol{R}_\omega|, \tag{E.6}$$

where $|\delta\boldsymbol{R}_\omega\rangle$ are the vibrational modes in the elastic network without weak interactions. Thus, let us derive the explicit form of $\mathscr{G}$. First, notice that

$$\begin{aligned}
\mathscr{M}^{-1} &\simeq \left(S_s^t S_s + \alpha\mathscr{I}\right)^{-1} = \left(\mathscr{S}_s^t\mathscr{S}_s\right)^{-1}\left(\mathscr{I} + \alpha\left(\mathscr{S}_s^t\mathscr{S}_s\right)^{-1}\right)^{-1} \\
&= \left(\mathscr{S}_s^t\mathscr{S}_s\right)^{-1}\left(\mathscr{I} - \alpha\left(\mathscr{S}_s^t\mathscr{S}_s\right)^{-1} + \alpha^2\left(\mathscr{S}_s^t\mathscr{S}_s\right)^{-2} - \alpha^3\left(\mathscr{S}_s^t\mathscr{S}_s\right)^{-3} + ...\right) \\
&= \sum_\omega \frac{1}{\omega^2}|\delta\boldsymbol{R}_\omega\rangle\langle\delta\boldsymbol{R}_\omega| - \sum_\omega \frac{\alpha}{\left(\omega^2\right)^2}|\delta\boldsymbol{R}_\omega\rangle\langle\delta\boldsymbol{R}| + \sum_\omega \frac{\alpha^2}{\left(\omega^2\right)^3}|\delta\boldsymbol{R}\rangle\langle\delta\boldsymbol{R}_\omega| \qquad \text{(E.7)} \\
&\quad - \sum_\omega \frac{\alpha^3}{\left(\omega^2\right)^4}|\delta\boldsymbol{R}_\omega\rangle\langle\delta\boldsymbol{R}_\omega| + ... \qquad \text{(E.8)}
\end{aligned}$$

Now, let us denote as $|\delta \boldsymbol{r}_\omega\rangle$ the orthonormal eigenvectors in contact space, hence $|\delta \boldsymbol{r}_\omega\rangle = S_t|\delta \boldsymbol{R}_\omega\rangle/\omega$. Hence,

$$\mathscr{S}_s\mathscr{M}^{-1}\mathscr{S}_s^t = \sum_\omega |\delta \boldsymbol{r}_\omega\rangle\langle\delta \boldsymbol{r}_\omega| - \sum_\omega \frac{\alpha}{\omega^2}|\delta \boldsymbol{r}_\omega\rangle\langle\delta \boldsymbol{r}_\omega| + \sum_\omega \frac{\alpha^2}{\left(\omega^2\right)^2}|\delta \boldsymbol{r}_\omega\rangle\langle\delta \boldsymbol{r}_\omega| \tag{E.9}$$

$$- \sum_\omega \frac{\alpha^3}{\left(\omega^2\right)^3}|\delta \boldsymbol{r}_\omega\rangle\langle\delta \boldsymbol{r}_\omega| + ... \tag{E.10}$$

Thus,

$$\mathscr{G} = \mathscr{I} - \sum_\omega |\delta \boldsymbol{r}_\omega\rangle\langle\delta \boldsymbol{r}_\omega| + \sum_\omega \frac{\alpha}{\omega^2}|\delta \boldsymbol{r}_\omega\rangle\langle\delta \boldsymbol{r}_\omega| - \sum_\omega \frac{\alpha^2}{\left(\omega^2\right)^2}|\delta \boldsymbol{r}_\omega\rangle\langle\delta \boldsymbol{r}_\omega| + \sum_\omega \frac{\alpha^3}{\left(\omega^2\right)^3}|\delta \boldsymbol{r}_\omega\rangle\langle\delta \boldsymbol{r}_\omega| + ... \tag{E.11}$$

Now, let us define $\delta z = z - z_c$, where z is the coordination number and z_c is the critical coordination number equal to 4. When $\delta z < 0$, the relation $|\delta \boldsymbol{r}\rangle = S_t|\delta R_\omega\rangle/\omega$ defines all contact space. On the contrary, when $\delta z > 0$ there will be a number of eigenvectors in contact space undefined, i.e.,

$$\begin{cases} \sum_\omega |\delta \boldsymbol{r}_\omega\rangle\langle\delta \boldsymbol{r}_\omega| = \mathscr{I}\,, & \text{for } \delta z < 0 \\ \sum_\omega |\delta \boldsymbol{r}_\omega\rangle\langle\delta \boldsymbol{r}_\omega| + \sum_p^{\delta z N/2} |\delta \boldsymbol{r}_p\rangle\langle\delta \boldsymbol{r}_p| = \mathscr{I} & \text{for } \delta z > 0\,. \end{cases} \tag{E.12}$$

Taking into account these considerations, we finally obtain

$$\begin{aligned} \mathscr{G} &= \sum_p^{\delta z N/2} |\delta r_p\rangle\langle\delta r_p| + \sum_\omega \frac{\alpha}{\omega^2}|\delta \boldsymbol{r}_\omega\rangle\langle\delta \boldsymbol{r}_\omega| - \sum_\omega \frac{\alpha^2}{\left(\omega^2\right)^2}|\delta \boldsymbol{r}_\omega\rangle\langle\delta \boldsymbol{r}_\omega| + \sum_\omega \frac{\alpha^3}{\left(\omega^2\right)^3}|\delta \boldsymbol{r}_\omega\rangle\langle\delta \boldsymbol{r}_\omega| + ... \\ &= \sum_p^{\delta z N/2} |\delta \boldsymbol{r}_p\rangle\langle\delta \boldsymbol{r}_p| + \sum_\omega \frac{\alpha}{\alpha+\omega^2}|\delta \boldsymbol{r}_\omega\rangle\langle\delta \boldsymbol{r}_\omega|\,. \end{aligned} \tag{E.13}$$

Thus, the Hamiltonian becomes

$$H(\{\sigma_i\}) = \frac{1}{2}\sum_{p=1}^{\delta z N/2} |\langle\sigma|\delta \boldsymbol{r}_p\rangle|^2 + \frac{1}{2}\sum_\omega \frac{\alpha}{\alpha+\omega^2}|\langle\sigma|\delta \boldsymbol{r}_\omega\rangle|^2\,. \tag{E.14}$$

From here we may now compute the *annealed* free energy.

E.2 Vibrational Entropy

In this note we obtain the Eq. (3) of the main work. Let us take into consideration the previous derivations. We further denote as $X_p = \langle\sigma|\boldsymbol{r}_p\rangle$ and $X_\omega = \langle\sigma|\boldsymbol{r}_\omega\rangle$ and treat them as Gaussian variables such as to consider annealed disorder. Thus, the partition function will have the following form:

$$\begin{aligned} Z &= \underbrace{\left(\frac{Nz}{2}\right)!}_{\text{config. entropy contribution}} \underbrace{\iint e^{-H(\{X_p,X_\omega\})/T}\prod_{p=1}^{\delta z N/2}\frac{e^{-X_p^2/2}}{\sqrt{2\pi}}dX_p\prod_\omega\frac{e^{-X_\omega^2/2}}{\sqrt{2\pi}}dX_\omega}_{\text{averaged stored energy contribution}} \\ &\cdot \underbrace{\int d^{dN}p\int d\{\delta R\}e^{-p^2/2mT}e^{-\langle\delta R|\mathscr{M}|\delta R\rangle/2T}}_{\text{vibrational energy contribution}}\,. \end{aligned} \tag{E.15}$$

The prefactor in the partition function corresponds to the configurational entropy which we assume that way momentarily. The integrals over phase space are being weight with Gaussian distribution with mean value and standard deviation equal to 0 and 1, respectively. The last term contains the vibrations in the network and, therefore, is the term that contributes to the vibrational entropy. It is feasible to reduce the partition function in Eq. (E.15) to,

$$\begin{aligned} Z &= \left(\frac{Nz}{2}\right)!\left[\left(1+\frac{1}{T}\right)^{-1/2}\right]^{\delta zN/2}\prod_{\omega}\left(1+\frac{\alpha}{T(\alpha+\omega^2)}\right)^{-1/2} \\ &\cdot \quad (2\pi T)^{Nd/2}\det(\mathscr{M})^{-1/2}\ . \end{aligned} \tag{E.16}$$

The free energy is obtained from the partition function as usual. Then, the vibrational entropy, $S_{vib}(\Gamma)$, reads

$$S_{vib}(\Gamma) = Nn_c\ln(2\pi T) - \frac{1}{2}\ln\det(\mathscr{M})\ . \tag{E.17}$$

E.3 Thermodynamics in the Homogeneous phase

In this note, we obtain the thermodynamic quantities in the homogeneous phase, used to fit the simulation results. Let us take into account the previous derivations. Now, we define the number of redundant directions as R, which satisfy the relation $R = \mathscr{F} + N_s - Nd$ where $\mathscr{F}$ is the number of floppy modes. Let us denote the number of constraints as $n_r = R/N$.

Since for a fixed value of z, n_r can take different values, the partition function will rather be expressed as

$$\bar{Z} = \exp\left[\frac{1}{T}\left(NdT\ln(2\pi T) - \frac{T}{2}\sum_{\omega>0}\ln\left(1+\frac{\alpha}{T(\alpha+\omega^2)}\right) - \frac{T}{2}\sum_{\omega}\ln\left(\omega^2+\alpha\right)\right)\right] \tag{E.18}$$

$$\sum_{n_r}\exp\left(-\frac{N}{2}\left(n_r\ln(1+1/T) + \left(n_r - \frac{\delta z}{z}\right)\ln(\alpha) - 2s_c(n_r)\right)\right)\ . \tag{E.19}$$

Here we have replaced $\ln\left(\frac{Nz}{2}!\right) \to N_s s(n_r)$. Treating redundant constraints as defects, one may show that the configurational entropy (per spring) is similar to that of an ideal gas (176), i.e.,

$$s_c(n_{ex}) \approx s(0) - n_{ex}\ln\frac{n_{ex}}{en_0(z)}\ . \tag{E.20}$$

Here n_{ex} is the excess number of redundant constraints which is defined as

$$n_{ex} = \frac{1}{N_s}\left(R - \frac{N\delta z}{2}\Theta(\delta z)\right), \tag{E.21}$$

where $n_0(z) = n_{ex}(z, T \to \infty)$ and $s(0)$ is the entropy density for a minimal number of redundant constraints. Now, introducing Eq. (E.20) as the configurational entropy in the partition function (Eq. (E.19)) and using the saddle point method, we find that

$$\begin{cases} n_{ex}^0 = n_0(z)\left(\alpha(1+1/T)\right)^{-1/2} , \\ n_r^0 = n_{ex}^0 + \frac{\delta z}{z}\Theta(\delta z) . \end{cases} \tag{E.22}$$

From the partition function we obtain the free energy per spring, f, which yields

$$\begin{aligned} f_{hom}(T) &= T\left(\frac{n_r^0}{2n}\ln(1+1/T) + \frac{1}{2N_s}\sum_{\omega>0}\ln\left(1+\frac{\alpha}{T(\alpha+\omega^2)}\right)\right. \\ &\left. + \frac{1}{2N_s}\sum_{\omega}\ln\left(\omega^2+\alpha\right) + \frac{1}{n}\left(n_r - \frac{\delta z}{z}\right)\ln(\sqrt{\alpha}) - \frac{s_c\left(n_{ex}^0\right)}{n} - \frac{z_c}{z}\ln(2\pi T)\right) . \end{aligned} \tag{E.23}$$

From the free energy we may compute the rest of the thermodynamical quantities of interest. Before doing so, let us discuss Eq. (E.23). The first two terms come from the inherent structures energy and, hence, will contribute to the internal energy and the specific heat. In particular, the second term will gain relevance at low temperatures when $T \sim \alpha$ where the weak interactions are physically relevant in our model. The third and fourth terms are key for the homogeneous-to-heterogeneous phase transition since they contribute to the vibrational entropy. The fifth term corresponds to the configurational entropy while the last term contributes a constant in heat capacity, which is the constant in a solid, thus here on we will neglect. Also, in the following we will refer to thermodynamical quantities per spring as thermodynamical quantities and all thermodynamical quantities are divided by N_s.

The entropy ($S(T)$), internal energy ($E(T)$) and the heat capacity ($C(T)$) are obtained from Eq. (E.23) and yield

$$S_{hom}(T) = -\frac{f(T)}{T} + \frac{1}{2}\frac{n_r^0(T)/n}{T+1} + \frac{1}{2N_s}\sum_{\omega>0}\frac{1}{1+\left(1+\omega^2/\alpha\right)T} . \tag{E.24}$$

$$\begin{aligned} E_{hom}(T) &= \frac{T}{2(1+T)}\left(\frac{n_0(z)/n}{\sqrt{\alpha(1+1/T)}} + \frac{\delta z}{z}\Theta(\delta z)\right) \\ &+ \frac{1}{2N_s}\sum_{\omega>0}\frac{T}{1+\left(1+\omega^2/\alpha\right)T} . \end{aligned} \tag{E.25}$$

$$\begin{aligned} C_{hom}(T) &= \frac{1}{2(1+T)^2}\left(\frac{\frac{3}{2}n_0(z)/n}{\sqrt{\alpha(1+1/T)}} + \frac{\delta z}{z}\Theta(\delta z)\right) \\ &+ \frac{1}{2N_s}\sum_{\omega>0}\frac{1}{\left(1+\left(1+\omega^2/\alpha\right)T\right)^2} . \end{aligned} \tag{E.26}$$

The vibrational entropy, S^{v}_{hom}, as was mentioned previously, is

$$S^{v}_{hom} = -\frac{f}{2n}\ln(\alpha) - \frac{1}{2N_s}\sum_{\omega>0}\ln(\omega^2+\alpha) \approx -\frac{n_0(z)/n}{2\sqrt{\alpha(1+1/T)}}\ln(\alpha) + \Sigma^{v}_{hom}\,. \tag{E.27}$$

The approximation is done assuming $\alpha/\omega^2 \ll 1$.

E.4 Thermodynamics of the heterogeneous phase

In this note, we show and highlight the steps to obtain the thermodynamic quantities in the heterogeneous phase, used to fit the simulation results. We start by considering a floppy and a rigid domain in the network. With this in minds, let us denote as N_f the number of particles in the floppy domain and N_r the number of particles in the rigid domain. Let us also denote as $V_f = N_f/N$ and $V_r = N_r/N$. Furthermore, n is the mean constraint number, while N_s is the number of springs, $\mathscr{F}$ is the number of springs in the floppy phase while R is the number of springs in the rigid phase. Finally, n_f is the number of constraints per particle in the floppy domain while n_r is the number of constraints per particle in the rigid domain. These quantities satisfy the following Equations:

$$V_f + V_r = 1\,, \tag{E.28}$$

$$n_f V_f + n_r V_r = n\,, \tag{E.29}$$

$$F + N_s - N n_c = R\,. \tag{E.30}$$

Here $n_c = 2$ is the critical constraint number. From these Eqs. we obtain

$$n_f = \frac{N_f n_c - F}{N_f}\,, \tag{E.31}$$

$$n_c = \frac{N_r n_c + R}{N_r}\,. \tag{E.32}$$

From here, it is straightforward to obtain the configurational entropy, i.e., it is simply the logarithm of the number of ways one may allocate $N_f n_f$ springs in the floppy domain(which has $N_f n_m$ allocation places) times the number of ways to allocate $N_r n_r$ springs in the rigid domain (that has $N_r n_m$ allocation spots). Using Stirling's approximation, we obtain

$$\begin{aligned} S^{c}_{het}(T) &= \Sigma^{c}_{0} + \frac{V_r}{n}\left(n_r \log\frac{n_m}{n_r} + (n_m - n_r)\log\frac{n_m}{n_m - n_r}\right) \\ &\quad + \frac{V_f}{n}\left(n_f \log\frac{n_m}{n_f} + (n_m - n_f)\log\frac{n_m}{n_m - n_f}\right). \end{aligned} \tag{E.33}$$

Here Σ^c_{het} is the configurational entropy associated to the boundary which goes roughly as $\sim N^{2/3}$, thus in the thermodynamical limit is negligible. Moreover, $n_m = 3$ is the maximum number of constraints per particle. As was shown in (175), the gain in vibrational entropy when a floppy mode is introduced to the system, under certain conditions, may well be approximated by a constant λ. Hence, the vibrational entropy is simply

$$S^v_{het} = \Sigma^v_{het} + \frac{V_f}{n}\left(n_c - n_f\right)\lambda\,. \tag{E.34}$$

By maximizing the entropy, subject to the constraints given by Eqs. (E.28) and (E.29) through Lagrange multipliers, we obtain the following Equations:

$$\begin{cases} \frac{n_m - n_r}{n_r} = e^{\beta}\,, \\ \frac{n_m - n_f}{n_f} e^{-\beta} = e^{\lambda}\,, \\ \frac{n_f}{n_m} = 1 - \exp\left(\frac{\lambda n_c - \mu}{n_m}\right), \\ 1 - \frac{n_r}{n_m} = e^{-\mu/n_m}\,, \end{cases} \tag{E.35}$$

where μ and β are Lagrange multipliers.

From the previous Eqs. we obtain the following:

$$\frac{n_r}{n_m} = \frac{e^{-\lambda n_c/n_m} - 1}{e^{-\lambda} - 1}\,, \tag{E.36}$$

$$\frac{n_f}{n_m} = \frac{e^{\lambda n_c/n_m} - 1}{e^{\lambda} - 1}\,. \tag{E.37}$$

From the constraints (Eqs. (E.28) and (E.29)) we also obtain

$$V_r = \frac{n - n_f}{n_r - n_f}\,. \tag{E.38}$$

By taking into account the duality between self-stressed states and floppy modes (175), we replace $\lambda \to \lambda - 1/2\ln(1 + 1/T)$. Thus, Eqs. (E.36), (E.37) and (E.38) become

$$\frac{n_r(T)}{n_m} = \frac{e^{-\lambda n_c/n_m}(1 + 1/T)^{n_c/2n_m} - 1}{e^{-\lambda}(1 + 1/T)^{1/2} - 1}\,, \tag{E.39}$$

$$\frac{n_f(T)}{n_m} = \frac{e^{\lambda n_c/n_m}(1 + 1/T)^{-n_c/2n_m} - 1}{e^{\lambda}(1 + 1/T)^{-1/2} - 1}\,. \tag{E.40}$$

$$V_f(T) = \frac{n_r(T) - n}{n_r(T) - n_f(T)}\,. \tag{E.41}$$

The vibrational entropy, Eq. (E.34), becomes

$$S^{v}_{het} = \Sigma^{v}_{het} + \frac{1}{n} V_f(T) \left(n_c - n_f(T)\right) \lambda \,. \tag{E.42}$$

One shall be able to fit the vibrational entropy with two parameters s^{v}_{0} and λ. One shall also be able to compute the heat capacity from the free energy,

$$f_{het}(T) = \frac{T}{2n}(1 - V_f(T))(n_r(T) - n_c) \log\left(1 + \frac{1}{T}\right) - T S^{v}_{het}(T) - T S^{c}_{het}(T) \tag{E.43}$$

and the specific heat, $C_{het}(T)$, which is computed from the relation

$$C_{het}(T) = -T \frac{\partial^2 f_{het}(T)}{\partial T^2} \,. \tag{E.44}$$

The first term in Eq. (E.43) corresponds to the inherent structures' energy.

E.5 Fits

In this note we describe the way in which we fit the simulation results consistently with the Eqs. derived in the previous notes. Notice that the entropy gain when a floppy mode appears relates with the weak interaction approximately as $\lambda \sim \ln\sqrt{\alpha}$ (175). Throughout our simulations $\alpha = 3 \times 10^{-4}$, thus we expect $\lambda \approx 4$. The first thing we fit is the vibrational entropy and we do this by noticing that at low temperatures ($T \ll 1$) working Eq. E.27 it is feasible to obtain

$$\ln\left(S^{v}_{hom} - \Sigma^{v}_{hom}\right) \approx \ln\left(n_0(z) e^{\lambda} \lambda\right) + \frac{1}{2} \ln T \,. \tag{E.45}$$

Therefore, we tune the value of Σ^{v}_{hom} such that the fit of $\ln\left(S^{v}_{hom} - \Sigma^{v}_{hom}\right)$ *vs* $\ln T$ gives a straight line $y = mx + b$ with slope $m = 1/2$. Then,

$$n_0(z) = n \frac{e^{b-\lambda}}{\lambda} \,. \tag{E.46}$$

However, care must be taken since the λ parameter is no necessarily the same in the homogeneous and the heterogeneous. Thus we denote them as λ_{hom} and λ_{het}.

In the case of the heterogeneous phase, we have two fitting parameters left, namely, Σ^{v}_{het} and Σ^{c}_{het} which appear in the entropy (see Eqs. (E.33) and (E.42)) and the free energy (Eq. (E.43)). Thus, technically is, actually, one fitting parameter.

In the homogeneous phase, however, we must be cautious when $T \simeq \alpha$. Here, we follow the same path as in Ref. (155), which consists in replacing $\sum_{\omega>0} \to N_s \int d\omega D(\omega)$ for $\delta z \leq 0$ and $\sum_{\omega>0} \to$

$Nd\int d\omega D(\omega)$ for $\delta z > 0$. This approximation works better as we approach the thermodynamic limit, i.e., $N \to \infty$. Here, $D(\omega)$ is the vibrational density of states of random elastic networks. It is known that there are two frequency scales, namely, $\omega^* \sim \delta z$, above which a plateau of soft modes exists and a cutoff frequency, $\omega_c \gtrapprox 1$. Thus, we approximate $D(\omega)$ as

$$D(\omega) = \begin{cases} \frac{1}{\omega_c - \omega^*}, & \omega^* \le \omega \le \omega_c,\ \delta z \le 0 \\ \frac{1}{\omega_c}, & 0 \le \omega \le \omega_c,\ \delta z > 0 \end{cases} . \tag{E.47}$$

In order to simplify expressions, let us define the variable $x = \omega/\sqrt{\alpha}$. Similarly, $x_c = \omega_c/\sqrt{\alpha}$ and $x^* = \frac{|\delta z|}{z_c} x_c$. Thus, the Eqs. (E.23), (E.25) and (E.26) transform to,

$$\begin{aligned} f_{hom}(T) &= T\left(\frac{1}{2}\left(\frac{n_0(z)e^{\lambda}}{n\sqrt{1+1/T}} + \frac{\delta z}{z}\Theta(\delta z)\right)\ln(1+1/T)\right. \\ &\quad + \frac{1}{nx_c}\left(x\ln\left(1+\frac{1}{T(1+x^2)}\right) + 2\left(\frac{\sqrt{T+1}\arctan\left[\frac{\sqrt{T}x}{\sqrt{T+1}}\right]}{\sqrt{T}} - \arctan\left[\sqrt{x}\right]\right)\right)\Big|_{\chi(\delta z)}^{x_c} \\ &\quad \left. - \frac{n_0(z)e^{\lambda}\lambda}{n\sqrt{1+1/T}}\ln\left(\frac{e^{\lambda}\lambda}{\sqrt{1+1/T}}\right) - \Sigma_{hom}^{v} - \Sigma_{hom}^{c}\right) . \end{aligned} \tag{E.48}$$

$$\begin{aligned} E_{hom}(T) &= \frac{T}{2(1+T)}\left(\frac{n_0(z)e^{\lambda}}{n\sqrt{1+1/T}} + \frac{\delta z}{z}\Theta(\delta z)\right) \\ &\quad + \frac{1}{nx_c}\frac{\sqrt{T}\arctan\left[\frac{\sqrt{T}x}{\sqrt{T+1}}\right]}{\sqrt{T+1}}\Big|_{\chi(\delta z)}^{x_c} . \end{aligned} \tag{E.49}$$

$$\begin{aligned} C_{hom}(T) &= \frac{1}{2(1+T)^2}\left(\frac{\frac{3}{2}n_0(z)e^{\lambda}}{n\sqrt{1+1/T}} + \frac{\delta z}{z}\Theta(\delta z)\right) \\ &\quad + \frac{1}{2nx_c}\left(\frac{x}{(T+1)\left(1+T+Tx^2\right)} + \frac{\arctan\left[\frac{\sqrt{T}x}{\sqrt{T+1}}\right]}{\sqrt{T}\,(T+1)^{3/2}}\right)\Big|_{\chi(\delta z)}^{x_c} . \end{aligned} \tag{E.50}$$

where $\chi(\delta z)$ is defined as

$$\chi(\delta z) = \begin{cases} 0\,, & \delta z > 0 \\ x^*\,, & \delta z \le 0 \end{cases} . \tag{E.51}$$

As mentioned in the main work, the specific heat C is obtained from the mean energy fluctuation over the course of the Monte Carlo simulation, normalized by the temperature squared. Then, the

free energy is obtained in the Monte Carlo simulations from the direct measurement of the internal energy E and inferred total entropy $S = S_v + S_c$ by integrating over the specific heat,

$$S(T) = S(\infty) - \int_T^\infty \frac{C(T)}{T} \,. \tag{E.52}$$

In Fig. 3 of the main work we show the main results. In Table E.5 we show the values of the fitting parameters in the case of $n = 2.06$.

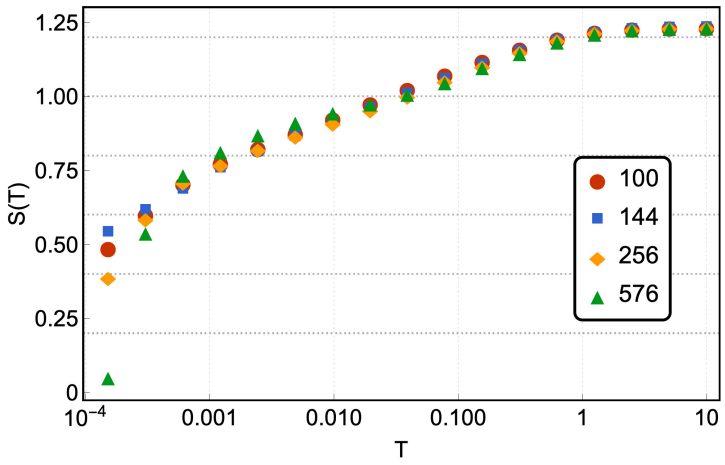

Figure E.1: Entropy $S(T)$ *vs* T for different system sizes (see legend). This was obtained from the Monte Carlo simulation, by integrating the specific heat (see text and main work for details). We fixed $S(T = 10) = 1.235$.

m	$n_0(z)$	λ_{hom}	Σ^v_{hom}	Σ^c_{hom}	x_c	λ_{het}	$\Sigma^v_{het} + \Sigma^c_{het}$
0.49 ± 0.01	8.5×10^{-3}	3.5	3.4×10^{-2}	0.892	280	3.0	0.04

Table E.1: Fitting parameters in the case of $n = 2.06$.

E.6 Liquid-Liquid transition temperature prediction

In this note we show how the T_{LLT} dependence on n was obtained. Similar to the previous notes, we compute a free energy for the heterogeneous and the homogeneous phase. Let us denote the free energy, in the homogeneous phase and in the heterogeneous phase as F_{hm} and F_{ht}, respectively. Hence, we have for the homogeneous phase

$$\mathsf{F}_{hm}(T)/T = \frac{n-2}{2n} \ln\left(1 + \frac{1}{T}\right) - S_{\mathrm{v}}(n,\lambda) - \ln\left(\frac{n_m}{n}\right) - \frac{n_m - n}{n} \ln\left(\frac{n_m}{n_m - n}\right) , \tag{E.53}$$

and, with the help of Eqs. (E.39), (E.40) and (E.41), the heterogeneous phase free energy is expressed as

$$\begin{aligned} \mathsf{F}_{ht}(T)/T &= \frac{1}{2n}(1-V_f(T))(n_r(T)-n_c)\log\left(1+\frac{1}{T}\right) \\ &\quad -\frac{V_r(T)}{n}\left(n_r(T)\log\frac{n_m}{n_r(T)}+(n_m-n_r(T))\log\frac{n_m}{n_m-n_r(T)}\right) \\ &\quad -\frac{V_f(T)}{n}\left(n_f(T)\log\frac{n_m}{n_f(T)}+\big(n_m-n_f(T)\big)\log\frac{n_m}{n_m-n_f(T)}\right) \\ &\quad -\big(1-V_f(T)\big)\,S_{\mathsf{v}}(n_r(T),\lambda)-V_f(T)S_{\mathsf{v}}(n_f(T),\lambda)\,. \end{aligned} \tag{E.54}$$

The first term in the r.h.s. of Eq. (E.53) corresponds to the internal energy while the second term corresponds to the vibrational entropy. The two last terms accounts for the configurational entropy. The heterogeneous phase free energy in Eq. (E.54) is obtained in an analogous way, however, assuming a floppy and rigid regions. The first line in the r.h.s. corresponds to the internal energy, while the second and third to the configurational entropy in the rigid and floppy regions, respectively. The fourth line corresponds to the vibrational entropy. The crux of the derivation relies in the computation of the vibrational entropy.

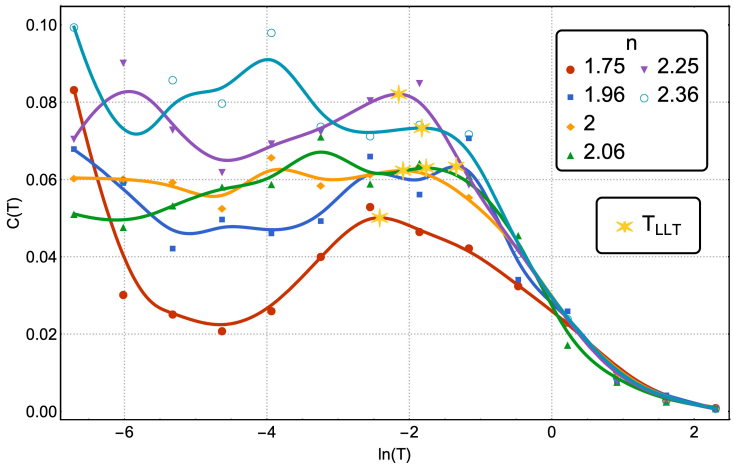

Figure E.2: Specific heat *vs* T for different constraint numbers n for 256 particles. The data points corresponds to the specific heat measured in the Monte Carlo simulation. The continuous curves are spline functions, obtained for each of the data sets (see legend). The yellow stars mark the spot where the $T_{LLT}(n)$ is located for a given n.

As was discussed in the previous notes, in the thermodynamical limit $\sum_{\omega>0} \to N_s \int d\omega D(\omega)$ for

$\delta z \leq 0$ and $\sum_{\omega>0} \to Nd\int d\omega D(\omega)$ for $\delta z > 0$. Thus, it is not difficult to show that,

$$S_{\mathrm{v}}(n,\lambda) = \begin{cases} -\frac{1}{2n}\left(-4+2ne^{-\lambda}\operatorname{arccot}\left(e^{-\lambda}\right)-2ne^{-\lambda}\arctan\left(\frac{(n-2)e^{\lambda}}{n}\right)+n\ln\left(1+e^{2\lambda}\right)\right. \\ \qquad \left.-(n-2)\ln\left(\frac{4+n(n+ne^{-2\lambda}-4)}{n^2e^{-2\lambda}}\right)\right), \qquad \delta n > 0, \\ -\lambda\frac{n-2}{n}-\frac{1}{2n}\left(-2n+2ne^{-\lambda}\arctan\left(\frac{2e^{\lambda}}{n}\right)+2ne^{-\lambda}\arctan\left(\frac{(n-2)e^{\lambda}}{n}\right)-2n\ln(n)\right. \\ \qquad \left.+2n\lambda+2\ln\left(4+n^2e^{-2\lambda}\right)-(n-2)\ln\left(4+n(n+ne^{-2\lambda}-4)\right)\right), \qquad \delta n \leq 0, \end{cases} . \tag{E.55}$$

The transition temperature $T_{LLT}(n)$ shown in Fig. 5a is obtained by equating the free energies from Eqs. (E.53) and (E.54). We tune the λ parameter to ≈ 2.67, which is where $T_{LLT} = 0.2$ when $n = 2.06$, in agreement with the results shown in Fig. 3 of the main work. From the Monte Carlo simulations, $T_{LLT}(n)$ was obtained from the first peak of the specific heat when lowering the temperature, while the error bars correspond to the size of the peaks. Since the measurements in the simulations were at the same set of temperatures, we obtained the peak by first applying the spline method to our data. In Fig. E.2 we show the specific heat data together with the spline functions and the $T_{LLT}(n)$ marked with yellow stars, for different values of n.

Appendix F

Principal Component Analysis applied to the 2D Ising Model

Let us imagine that we have N ($\gg 1$) degrees of freedom (say, a lattice of spins) which have some one-on-one interaction. One may wonder if there is a way to reduce those N degrees of freedom to some number, say, $M \geq 1$. This is perhaps the holy grail in Physics and tools ranging from the central limit theorem to renormalization group are used in this sense. Principal Component Analysis is another way to computationally study the possibility of a given set of variables may be reduced to a much smaller set.

To schematically see how PCA work, let us consider the following matrix

$$A = \begin{bmatrix} 1+\epsilon & 0 & 1-\epsilon \\ 0 & \epsilon & 0 \\ 1-\epsilon & 0 & 1+\epsilon \end{bmatrix} \tag{F.1}$$

and suppose that $\epsilon \ll 1$. The spectral decomposition of A is

$$A = 2|2\rangle\langle 2| + 2\epsilon|2\epsilon\rangle\langle 2\epsilon| + \epsilon|\epsilon\rangle\langle\epsilon| \tag{F.2}$$

where

$$|2\rangle = \frac{1}{\sqrt{2}}\begin{bmatrix}1\\0\\1\end{bmatrix} \tag{F.3}$$

$$|2\epsilon\rangle = \frac{1}{\sqrt{2}}\begin{bmatrix}1\\0\\-1\end{bmatrix} \tag{F.4}$$

$$|\epsilon\rangle = \begin{bmatrix}0\\\epsilon\\0\end{bmatrix} \tag{F.5}$$

Now, say, A acts on the ket $|x\rangle$ defined as

$$|x\rangle = \frac{1}{\sqrt{3}}\begin{bmatrix}1\\1\\1\end{bmatrix} = \sqrt{\frac{2}{3}}|2\rangle + \frac{1}{\sqrt{3}}|\epsilon\rangle\,. \tag{F.6}$$

Then,

$$A|x\rangle = 2\sqrt{\frac{2}{3}}|2\rangle + \frac{\epsilon}{\sqrt{3}}|\epsilon\rangle = \frac{1}{\sqrt{3}}\begin{bmatrix}2\sqrt{2}\\\epsilon\\2\sqrt{2}\end{bmatrix} \approx \begin{bmatrix}2\sqrt{2}\\0\\2\sqrt{2}\end{bmatrix} \tag{F.7}$$

But this result would be obtained by approximating or, to better say, by keeping the principal component in A, i.e.,

$$A \approx 2|2\rangle\langle 2|\,. \tag{F.8}$$

Now, let us apply these ideas to a bigger system, namely, a spin lattice. To this end, we follow Ref. (181). Consider $N = 40^2$ spins $\sigma_i = \{-1, 1\}$ interacting via the following Hamiltonian:

$$H = -J\sum_{\langle i,j\rangle=1}^{N}\sigma_i\sigma_j\,. \tag{F.9}$$

It is known that in two dimensions there is a second order phase transition at temperature $T \approx 2.26$ (temperature is in energy units). Thus, we generate an array $M \times N$, where $M = 1400$. We generate each row by fixing the temperature and sampling the spins 100 times, then we vary the temperature 0.1 and we sample the spins 100 times. We start at $T = 1.6$ and finish at $T = 2.9$ in steps of 0.1. The Monte Carlo algorithm we used is not a Metropolis type (189). Instead we used a cluster-based algorithm (190).

Let us skip the details and go straight to the data, which may be found at:

https://raw.githubusercontent.com/jquetzalcoatl/Test/master/IsingData.dat

We use the latin letters, say, i to tag the spin and we use greek subscripts, say, t_γ to denote the sample, such that $\gamma = \{1, ..., M\}$.

So, let us denote our data as X. Then:

$$X = \begin{bmatrix} \sigma_1(t_1) & \sigma_2(t_1) & \dots & \sigma_N(t_1) \\ \sigma_1(t_2) & \sigma_2(t_2) & \dots & \sigma_N(t_2) \\ \dots & \dots & \dots & \dots \\ \sigma_1(t_M) & \sigma_2(t_M) & \dots & \sigma_N(t_M) \end{bmatrix} . \tag{F.10}$$

Now, we are interested in applying PCA to the covariance matrix $\mathbb{M}$. Thus, we first subtract the mean value in each column of matrix X and denote this new matrix as ΔX, namely,

$$\Delta X = \begin{bmatrix} \sigma_1(t_1) - \frac{1}{M}\sum_{\gamma=1}^{M}\sigma_1(t_\gamma) & \sigma_2(t_1) - \frac{1}{M}\sum_{\gamma=1}^{M}\sigma_2(t_\gamma) & \dots & \sigma_N(t_1) - \frac{1}{M}\sum_{\gamma=1}^{M}\sigma_N(t_\gamma) \\ \sigma_1(t_2) - \frac{1}{M}\sum_{\gamma=1}^{M}\sigma_1(t_\gamma) & \sigma_2(t_2) - \frac{1}{M}\sum_{\gamma=1}^{M}\sigma_2(t_\gamma) & \dots & \sigma_N(t_2) - \frac{1}{M}\sum_{\gamma=1}^{M}\sigma_N(t_\gamma) \\ \dots & \dots & \dots & \dots \\ \sigma_1(t_M) - \frac{1}{M}\sum_{\gamma=1}^{M}\sigma_1(t_\gamma) & \sigma_2(t_M) - \frac{1}{m}\sum_{\gamma=1}^{M}\sigma_2(t_\gamma) & \dots & \sigma_N(t_M) - \frac{1}{M}\sum_{i=1}^{M}\sigma_N(t_\gamma) \end{bmatrix} \tag{F.11}$$

To shorten notation, we define the time average over M of $i\,th$ spin as $\tilde{\sigma}_i$, that is,

$$\tilde{\sigma}_i = \frac{1}{M}\sum_{\gamma=1}^{M}\sigma_i(t_\gamma) . \tag{F.12}$$

Then,

$$\Delta X = \sum_{i=1}^{N}\sum_{\gamma=1}^{M}\left(\sigma_i(t_\gamma) - \tilde{\sigma}_i\right)|\boldsymbol{e}_\gamma\rangle\langle\boldsymbol{e}_i| \tag{F.13}$$

Then,

$$\Delta X^T = \sum_{i=1}^{N}\sum_{\gamma=1}^{M}\left(\sigma_i(t_\gamma) - \tilde{\sigma}_i\right)|\boldsymbol{e}_i\rangle\langle\boldsymbol{e}_\gamma| \tag{F.14}$$

Then, the covariance matrix $\mathbb{M}$ is given by

$$\mathbb{M} = \frac{1}{M-1}\Delta X^T \Delta X = \frac{1}{M-1}\sum_{i,j=1}^{N}\sum_{\gamma,\eta=1}^{M}\left(\sigma_i(t_\gamma) - \tilde{\sigma}_i\right)\left(\sigma_j(t_\eta) - \tilde{\sigma}_j\right)|\boldsymbol{e}_i\rangle\langle\boldsymbol{e}_\gamma||\boldsymbol{e}_\eta\rangle\langle\boldsymbol{e}_j| \tag{F.15}$$

$$= \frac{1}{M-1}\sum_{i,j=1}^{N}\sum_{\gamma=1}^{M}\left(\sigma_i(t_\gamma) - \tilde{\sigma}_i\right)\left(\sigma_j(t_\gamma) - \tilde{\sigma}_j\right)|\boldsymbol{e}_i\rangle\langle\boldsymbol{e}_j| \tag{F.16}$$

$$= \sum_{i,j=1}^{N}|\boldsymbol{e}_i\rangle\mathbb{M}_{i,j}\langle\boldsymbol{e}_j| \tag{F.17}$$

where

$$\mathbb{M}_{i,j} = \frac{1}{M-1}\sum_{\gamma=1}^{M}\left(\sigma_i(t_\gamma)-\tilde{\sigma}_i\right)\left(\sigma_j(t_\gamma)-\tilde{\sigma}_j\right) . \tag{F.18}$$

The non-diagonal elements of matrix $\mathbb{M}$ corresponds to the covariance between two spins over "time" (well, we mean MC-steps) while the diagonal elements correspond to the variance over "time". Now, we are interested in knowing if this model is in any way strongly correlated. Hence, let us compute the eigenvalues and eigenvectors. In Fig. F.1 (left) we have plotted the 15 first eigenvalues.

Now take the two eigenvectors $|\lambda_1\rangle$ and $|\lambda_2\rangle$ corresponding to the two highest eigenvalues λ_1 and λ_2. Then, compute $|x_1\rangle = \Delta X|\lambda_1\rangle$ and $|x_2\rangle = \Delta X|\lambda_2\rangle$. Then, plot the kets $|x_1\rangle$ and $|x_2\rangle$. Notice that $|x_i\rangle$ has $M = 1400$ components, i.e., each component corresponds to a temperature. You can color the plot starting from blue to red in a continuous way, as we show in Fig. F.1 (right). These results show the direction where most of the variation occur in the space where the covariance matrix live. In plain and simple terms, the eigenvector associated to the largest eigenvalue corresponds to the order parameter of the system.

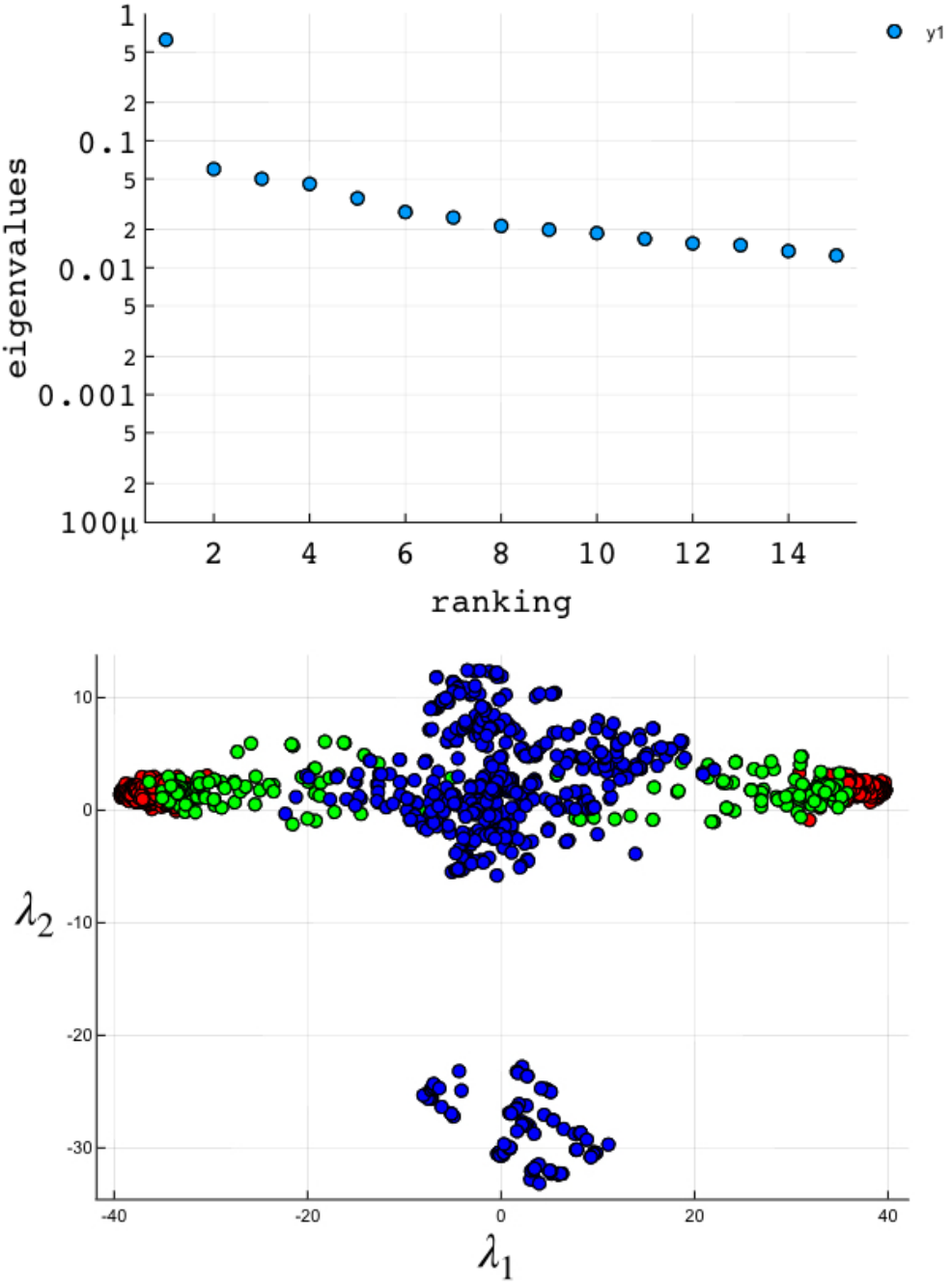

Figure F.1: (left) Eigenvalues.(right) First two eigenkets plotted. The color blue stand for low temperature and the color red for high temperature. Green represents the temperature where the phase transition occurs. Notice that this cluster-based Monte Carlo algorithm (190) is able to capture these fluctuations.